ตัวแปรสปินที่มีความไวต่อผลผลิตของอนุภาคสมมาตรยวดยิ่ง

นายนรพัทธ์ ศรีมโนภาษ

วิทยานิพนธ์นี้เป็นส่วนหนึ่งของการศึกษาตามหลักสูตรปริญญาวิทยาศาสตรดุษฎีบัณฑิต

สาขาวิชาฟิสิกส์

ภาควิชาฟิสิกส์ คณะวิทยาศาสตร์

จุฬาลงกรณ์มหาวิทยาลัยและมหาวิทยาลัยแอนต์เวิร์ป

(หลักสูตรร่วม)

ปีการศึกษา 2553

SPIN SENSITIVE VARIABLES FOR THE PRODUCTS OF

SUPERSYMMETRIC PARTICLES

Mr. Norraphat Srimanobhas

A Dissertation Submitted in Partial Fulfillment of the Requirements

for the Joint Degree of Doctor of Philosophy Program in Physics

(Joint Degree Program)

Department of Physics, Faculty of Science

Chulalongkorn University and University of Antwerp

Academic year 2010

Thesis Title	SPIN-SENSITIVE VARIABLES FOR THE PRODUCTS OF SUPERSYMMETRIC PARTICLES
By	Mr. Norraphat Srimanobhas
Field of Study	Physics
Thesis Advisor (CU)	Burin Asavapibhop, Ph.D.
Thesis Advisor (UA)	Professor Albert De Roeck, Ph.D.

Accepted by the Faculty of Science, Chulalongkorn University and University of Antwerp in Partial Fulfillment of the Requirements for the Joint Doctoral Degree

.... Dean of the Faculty of Science
(Professor Supot Hannongbua, Ph.D.) Chulalongkorn University

.... Dean of the Faculty of Science
(Professor Herwig Leirs, Dr. Wet.) University of Antwerp

THESIS COMMITTEE

.... Chairman
(Ahpisit Ungkitchanukit, Ph.D.)

.... Thesis Advisor
(Burin Asavapibhop, Ph.D.) Chulalongkorn University

.... Thesis Advisor
(Professor Albert De Roeck, Ph.D.) University of Antwerp

.... Examiner
(Assistant Professor Patcha Chatraphorn, Ph.D.)

.... Examiner
(Assistant Professor Nakorn Phaisangittisakul, Ph.D.)

.... External Examiner
(Assistant Professor Chinorat Kobdaj, Ph.D.)

นรพัทธ์ ศรีมโนภาษ : ตัวแปรที่ไวต่อสปินสำหรับผลผลิตของอนุภาคสมมาตรยวดยิ่ง. (SPIN-SENSITIVE VARIABLES FOR THE PRODUCTS OF SUPERSYMMETRIC PARTICLES) อ. ที่ปรึกษาวิทยานิพนธ์หลัก : อ.ดร.บุรินทร์ อัศวพิภพ, อ. ที่ปรึกษาวิทยานิพนธ์ร่วม : PROF. ALBERT DE ROECK, PH.D., 155 หน้า.

สมมาตรยวดยิ่งเป็นหนึ่งในทฤษฎีที่ต่อขยายจากทฤษฎีแบบจำลองมาตรฐาน ในทฤษฎีนี้ อนุภาคทุกตัวในแบบจำลองมาตรฐานจะมีคู่เป็นอนุภาคสมมาตรยวดยิ่ง กล่าวคืออนุภาคเฟอร์มิออนจะมีคู่เป็นอนุภาคสมมาตรยวดยิ่งโบซอน และในทางกลับกัน อนุภาคโบซอนก็จะมีคู่เป็นอนุภาคสมมาตรยวดยิ่งเฟอร์มิออน

การค้นหาอนุภาคสมมาตรยวดยิ่งนี้เป็นหนึ่งในหัวข้อศึกษาหลักของเครื่องตรวจวัดอนุภาคคอมแพคมิวออนโซลินอยด์ (ซีเอ็มเอส) ซึ่งเป็นเครื่องตรวจวัดอนุภาคทั่วไป ตั้งอยู่ที่เครื่องเร่งอนุภาคฮาดรอนขนาดใหญ่ (แอลเอชซี) ณ สถาบันวิจัยเซิร์น ในวิทยานิพนธ์นี้ได้ศึกษาการวัดสปินของอนุภาคสมมาตรยวดยิ่งผ่านการศึกษาความสัมพันธ์เชิงมุมของกลุ่มของอนุภาคซึ่งเกิดจากการสลายตัวของอนุภาคสมมาตรยวดยิ่งที่เป็นฟังก์ชั่นของปริมาณที่ไม่แปรเปลี่ยนลอเรนซ์ ซึ่งคือมวลนิ่งของกลุ่มอนุภาคที่เกิดจากการสลายตัวของอนุภาคสมมาตรยวดยิ่ง ซึ่งสามารถแสดงความไม่สมมาตรดังกล่าวข้างต้นได้ ในการศึกษานี้ได้ใช้การสลายตัวของอนุภาคสมมาตรยวดยิ่ง 2 รูปแบบคือ การสลายตัวของสควาร์กที่ให้อนุภาคนิวทรอลิโนและการสลายตัวของสท็อป (คู่ของอนุภาคท็อปในแบบจำลองมาตรฐาน) ที่ให้ชาร์จิโนเป็นกรณีศึกษา

จากการศึกษา สามารถสรุปได้ว่าเราสามารถที่จะสกัดข้อมูลเกี่ยวกับสปินของอนุภาคสมมาตรยวดยิ่งได้ โดยปริมาณของข้อมูลที่ต้องการนั้นขึ้นอยู่กับมวลของอนุภาคสมมาตรยวดยิ่ง นอกจากนี้เรายังได้ศึกษาการสลายตัวของอนุภาคสมมาตรยวดยิ่งที่ให้อนุภาคผลิตภัณฑ์ในหลายรูปแบบ เพื่อที่จะสามารถวัดคุณลักษณะเชิงสปินของอนุภาคสมมาตรยวดยิ่งได้อย่างหลากหลาย

ภาควิชา ....ฟิสิกส์........ ลายมือชื่อนิสิต..............................

สาขาวิชา ....ฟิสิกส์........ ลายมือชื่อ อ.ที่ปรึกษาวิทยานิพนธ์หลัก..............................

ปีการศึกษา ....2553........ ลายมือชื่อ อ.ที่ปรึกษาวิทยานิพนธ์ร่วม..............................

4672292423 : MAJOR PHYSICS

KEYWORDS : SUPERSYMMETRY / SPIN / CMS / LHC / CERN

NORRAPHAT SRIMANOBHAS : SPIN-SENSITIVE VARIABLES FOR THE PRODUCTS OF SUPERSYMMETRIC PARTICLES. THESIS ADVISOR : BURIN ASAVAPIBHOP, PH.D., THESIS CO-ADVISOR : PROF. ALBERT DE ROECK, PH.D., 155 pp.

Supersymmetry (SUSY) is a possible extension of the Standard Model, which predicts that each Standard Model fermion has a boson superpartner and each Standard Model boson has a fermion superpartner.

The search for supersymmetry is one of the main topics for study with the Compact Muon Solenoid (CMS), a general purpose detector at the Large Hadron Collider (LHC) at CERN. In this thesis, particle spin measurement are studied through effects in angular correlations in the decay products of supersymmetric particles. A Lorentz invariant quantity, the invariant mass of decay products, has been used to build asymmetries to investigate these correlation effects. Two different supersymmetric decay chains, namely the decay of a squark via a neutralino-2 and the decay of a stop quark (partner of top quark) via a chargino-1, have been used as examples for this study

We conclude that we can expect to extract spin information from the sparticles. The required amount of data depends on the supersymmetric particle mass spectrum. We have studied several final states, in order to have several measurements for the spin characterization of the supersymmetric paticles

Department : Physics	Student's Signature Norraphat Srimanobhas
Field of Study : Physics	Advisor's Signature
Academic Year : 2010	Co-Advisor's Signature

Acknowledgements

First and the foremost, I would like to sincerely express my special thanks to my Ph.D. supervisors, Dr. Burin Asavapibhop and Prof. Dr. Albert De Roeck for their valuable guidance, patient, support and giving me an opportunity to join the CMS collaboration. Their careful editing contributed enormously to this thesis.

I am very grateful to Prof. Dr. Supot Hannongbua, Asst. Prof. Dr. Kajornyod Yoodee, Prof. Dr. Eddi De Wolf and Prof. Dr. Nick Van Remortel for their support on the joint Ph.D. program between Chulalongkorn University and University of Antwerp. I am also grateful to Dr. Ahpisit Ungkitchanukit, Asst. Prof. Dr. Patcha Chatraphorn, Asst. Prof. Dr. Nakorn Phaisangittisakul, Asst. Prof. Dr. Chinorat Kobdaj for serving as the thesis committee. All of whom have made valuable comments and have been helpful in the production of the thesis.

I thank to my CERN colleagues from various departments, Dr. Peter Timothy Cox, Dr. Pedro Arce, Dr. Vitaliano Inglese, Domenico Della Ratta, Lukasz Piotr Pater, Hovhannes Khandanyan and Dr. Sara Diglio, for their invaluable support and friendship.

This research has been supported and funded by the Development and Promotion of Science and Technology Talent Project (DPST), Chulalongkorn University, and University of Antwerp.

Last but not the least, I would like to thank my family for supporting me spiritually throughout my life.

Contents

Chapter **Page**

Chapter **Page**

Chapter **Page**

List of Tables

Table **Page**

Table **Page**

Table **Page**

List of Figures

Figure **Page**

Figure **Page**

Figure **Page**

Figure **Page**

Figure **Page**

Figure **Page**

Figure **Page**

Figure **Page**

Figure **Page**

Figure **Page**

CHAPTER I

Introduction

Supersymmetry (SUSY) is a hypothetical symmetry extended to the Standard Model (SM) theory. It was introduced since early 1970s and became popular because it can provide descriptions to the missing parts of the Standard Model, such as the hierarchy problem that deals with the mass of the Higgs bosons, or candidates of the dark matter in the cosmological theory. The overview of the supersymmetry and some solutions proposed by the supersymmetry will be introduced in Chapter 2.

However, the existence of the supersymmetry also brings us to many questions about its properties, such as masses of supersymmetric particles (known as sparticles or superpartners) which have been proposed to be heavier than their Standard Model partners. An important question is how can we discover these supersymmetric particles. Since masses of supersymmetric particles have been predicted in the TeV energy scale, it is a chance for the Large Hadron Collider (LHC) to create the supersymmetric particles in the controlled environment. The LHC is constructed at the European Organization for Nuclear Research (CERN), the world largest particle physics laboratory. The LHC is designed to collide protons at 14 TeV in the center of mass frame. On 30 November 2009, the LHC became the worlds highest energy particle accelerator from the collision energy at the 2.36 TeV (1.18 TeV in each beam). At present (2011), the LHC is running at 7 TeV (3.5 TeV in each beam) for 1-2 years to collect data for physicists. A long shutdown will come afterward to prepare the machine to run at the designed energy (14 TeV). To discover the supersymmetric particles, two general purposed detectors, called ATLAS (A Toroidal LHC ApparatuS) and CMS (Compact Muon Solenoid), will be used. The details of the LHC and the CMS detector will be described in Chapter 3.

Since new physics always comes with some unknown parameters, it opens us to many possible channels. The characteristic of each channel is different. To study the new physics phenomena, the Monte Carlo studies come significantly to allow physicists to prepare necessary analysis tools. The detail of the CMS computing system will be introduced in Chapter 4.

Nowadays, physics beyond the Standard Model can be divided into two groups by the spin of the predicted particles. Both groups can propose the possible way to correct the missing parts of the Standard Model. The supersymmetry comes out with new particles which have the spins differ by $\hbar/2$ unit from their Standard Model partners. The important of this thesis is to study the possible ways to obtain the spin information of some supersymmetric particles if they exits at the LHC. In this thesis, the effect from the spin correlation factor of the supersymmetric particles to the kinematics of the decay products is studied with two decay chains of interest, including $\tilde{q} \to q\tilde{\chi}_2^0 \to ql^{\pm}_{near}\tilde{l}^{\mp} \to ql^{\pm}_{near}l^{\mp}_{far}\tilde{\chi}_1^0$ and $\tilde{t}^{\pm} \to b^{\mp}\tilde{\chi}_1^{\pm} \to b^{\mp}l^{\pm}\tilde{\nu}_l \to bl^{\pm}\nu_l\tilde{\chi}_1^0$. Three parameter sets (called LM1, LM2, and LM6) of the minimal supergravity (mSUGRA) have been used. The characteristics of each set will be discussed in Chapter 2. The analysis methods will be discuss in Chapter 5. The conclusion of works will be discussed in Chapter 6.

Note that, the extra work on the neutron background of the CMS detector will be discussed in Appendix B. This project had been done since the author was the summer student at CERN in 2004. In this project, the number of hits in the muon chambers from neutrons was studied. Not only the physics results come out, but also experiences of computer simulation for particle physics were gained significantly.

CHAPTER II

Theoretical background

What are the basic components of the matter around us? How do the basic components interact with each other? These two questions are classic questions since long time ago. Many answers of these two questions has been proposed. Democritus, the ancient greek philosopher, introduced the first suggestion of the components of the matter. He suggested that the matter was built from small indivisible particles, called atoms. After that, for more than 2000 years nobody continues the exploration for atom. In the 1800's, J. Dalton performed experiments to show that the matter consists of elementary lumpy particles, or atoms.

The era of the modern particle physics can be considered to start at the end of the 19th century when J. J. Thompson discovered the electron and proposed a model for the structure of the atom. In the beginning of the 20th century, the basic concepts of modern particle physics had been developed, including quantum mechanics and discoveries of the subatomic particles, such as neutron. In 1964, the idea of quarks was proposed by M. Gell-Mann and G. Zweig (independently). They proposed that three quarks and anti-quarks combined in many dierent ways according to the rules of symmetry could explain the existence of many particles. They called these three types of constituents as up-quark, down-quark and strange-quark. In 1967, S. Weinberg, S. Glashow (collaboration) and A. Salam (independent) proposed the so-called electroweak theory, to merge the electromagnetic and weak nuclear forces together. In 1969, J. Friedman, H. Kendall, and R. Taylor found the first evidence of quarks. A years after that, the Standard Model (SM) has been developed. Between 1970 and 2000, the members of the Standard

Model particles had been discovered, i.e. charmed quark (1974), tau lepton (1975), W and Z bosons (1983) and top quark (1995). The tau neutrino, the last member of the Standard Model, except Higgs bosons, was discovered in 2000.

In this chapter, the brief review of the Standard Model theory will be introduced firstly, then the supersymmetry will be discussed as a possible candidates of the beyond Standard Model (BSM) theories.

2.1 The Standard Model

2.1.1 Introduction

The Standard Model is a collection of theories which describe the knowledge of the elementary particles and three kinds of fundamental interactions. At present, we can describe matters and their interactions by two types of particles, called bosons and fermions. Fermions are particles which obey the Fermi-Dirac statistics. They have half-integer spins in the units of Planck's constant ($\hbar$). The elementary constituents of matters which include quarks and leptons are in the fermion group. For the bosons, they are particles which obey the Bose-Einstein statistics, and have integer spin in the same unit as fermions. The particles in this group are described as carriers of the fundamental forces, including the electromagnetic force, the weak nuclear force, and the strong nuclear force. The details of the matter and forces will be described in Sections 2.1.2 and 2.1.3, respectively.

In the Standard Model, there are four fundamental forces which can describe all phenomena in nature. These fundamental forces consist of the electromagnetic, the weak, the strong, and the gravitational forces. The electromagnetic and weak forces can be described by the **unified electroweak** theory. The strong force is described by the **quantum chromodynamics (QCD)** theory. The Standard Model is a combination of the gauge field theories which explain electroweak and strong forces, but it does not currently include gravity.

A problem of the Standard Model is the missing description about the mass of each particle. It is obvious from experiments that most of the Standard Model particles are massive, but when we put mass terms into the Standard Model Lagragian, it breaks the gauge invariance and the results is nonrenormalizable. A popular solution for this problem is the **Higgs mechanism** which requires spontaneous symmetry breaking. A brief review of Higgs boson searches is described in Section 2.1.4. A comprehensive description of the Standard Model can be found in [7].

2.1.2 Matter

As mentioned previously, All known matters around us are made of atoms. Atom is composed of electrons and atomic nucleus. A nucleus is formed by protons and neutrons, which are composed of quarks. Table 2.1 shows elementary fermionic particles. They are divided into two groups, lepton and quark. In the Standard Model, there are total twenty four fermions, which are six leptons and six quarks, and each of them has its corresponding antiparticles. An antiparticle is a particle which has the same mass as its associate but has opposite charge.

In the quark model, a quark is always combined with other (anti-) quark(s), we call the particles which are composed of quarks and/or anti-quarks as **hadrons**. We can separate the groups of quarks and anti-quarks into three groups which are the **baryon** which is composed of three quarks, the **antibaryon** which is composed of three anti-quarks, and the **mesons** which is composed of quark and anti-quark pair. Examples of hadrons are given in Table 2.2.

2.1.3 Forces

All of the forces we know at present are governed by the combination of four fundamental forces, including gravity, electromagnetism, strong nuclear force, and weak nuclear force. In the Standard Model, the interactions between particles are

Name	Symbol	Mass (MeV/c^2)	Charge (C)	Mean life time
Electron	e	0.511	-1	$> 4.6 \times 10^{26}$ yr
Electron neutrino	ν_e	$< 0.000\,002\,2$	0	Unknown
Muon	μ	105.65	-1	2.19×10^{-6} s
Muon neutrino	ν_μ	< 0.17	0	Unknown
Tau	e	1776.54	-1	290.6×10^{-15} s
Tau neutrino	ν_τ	< 15.5	0	Unknown
Up quark	u	1.5 - 3.3	$+\frac{2}{3}$	
Down quark	d	3.5 - 6.0	-$\frac{1}{3}$	
Charm quark	c	$1.27^{+0.07}_{-0.11} \times 10^3$	$+\frac{2}{3}$	
Strange quark	s	104^{+26}_{-34}	-$\frac{1}{3}$	
Top quark	t	$171.2 \pm 2.1 \times 10^3$	$+\frac{2}{3}$	
Bottom quark	b	$4.20^{+0.17}_{-0.17} \times 10^3$	-$\frac{1}{3}$	

Table 2.1: The basic properties of the quarks and leptons. Note that, the detail in neutrino masses can be found in [1, 2].

Particles	Components	Mass (MeV/c^2)	Charge (C)
π^+	$u\bar{d}$	139.57	1
K^-	$s\bar{u}$	493.67	-1
K^0	$\bar{d}s$	497.61	0
D^+	$c\bar{d}$	1869.62	1
Proton	uud	938.27	1
Neutron	udd	939.57	0
Λ	uds	1115.68	0
Σ^-	dds	1197.45	-1
Ξ^0	uss	1314.86	0
Ω^-	sss	1672.45	-1

Table 2.2: The examples of hadrons.

Type of forces	Range (m)	Related Theory	Mediators
Electromagnetism	∞	Quantum Electrodynamics	Photon
Weak	10^{-18}	Electroweak	$W^{\pm}$, Z^0
Strong	10^{-15}	Quantum Chromodynamics	gluons
Gravity	∞	General relativity	graviton

Table 2.3: The properties of the four basic forces.

described by the force mediator exchanges. For example, in the electron repulsion process, the virtual photon is transferred between two electrons, and makes them move conversely from each other. In the macroscopic pictures, we describe this process by the electrical repulsion force between the same charge objects.

Note that, in the Standard Model, the graviton which is the mediator of the gravitational force has been proposed but does not include in the theory. The properties of each force are shown in Table 2.3.

2.1.4 The Higgs mechanism

A remaining question of the Standard Model is masses of particles. The mechanism which can explain the masses of $W^{\pm}$ and Z bosons is the Higgs mechanism which lies in a process of spontaneous symmetry breaking.

The symmetry breaking happens when we consider the vacuum state, the state with no fields ($\varphi = 0$), of some Lagrangians. We found that there are a true ground state where $\varphi = 0$ is not a real minimum. For example, when we consider Lagrangian in forms of

$$\mathcal{L} = \frac{1}{2}(\partial_\mu \varphi)^2 - \frac{1}{2}\mu^2\varphi^2 - \frac{1}{4}\lambda\varphi^4, \tag{2.1}$$

where λ is the coupling constant of the interaction which depends on the energy scale and it has a positive value. The potential is

$$V(\varphi) = \frac{1}{2}\mu^2\varphi^2 + \frac{1}{4}\lambda\varphi^4. \tag{2.2}$$

The potential is drawn in Figure 2.1. To find the minimum, we calculate the derivative of the potential V with respect to φ and set it equal to zero.

$$0 = \varphi(\mu^2 + \lambda\varphi^2) \tag{2.3}$$

If μ^2 is chosen to be a negative, a non trivial minimum of the potential exists where

$$\mu^2 + \lambda\varphi^2 = 0 \tag{2.4}$$

The two possible minima can be given by

$$\varphi = \pm\sqrt{\frac{-\mu^2}{\lambda}} = \pm\nu \tag{2.5}$$

We can go to one of minima, but it breaks the symmetry. When the perturbation theory is applied around the minimum, the symmetry is broken and allows the mass tems to emerge. This is the concept of the Higgs machanism.

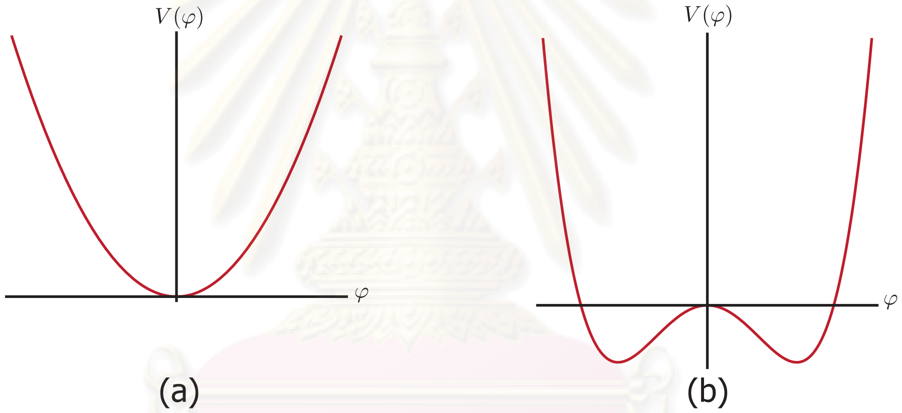

Figure 2.1: The potential for the Lagrangian given in Equation (2.1), for the case of (a) $\mu^2 > 0$, (b) $\mu^2 < 0$.

The Higgs mechanism for the electroweak symmetry breaking can predict precisely the masses and the couplings of the $W^{\pm}$ and Z bosons. The theoretical prediction agrees with the experimental results. In addition, the existance of a massive boson, which is called **Higgs boson**, is also predicted. At present, the Higgs boson has not been discovered yet. It is one of the highest expectations to be discovered at the LHC. The previous CERN accelerator LEP had placed the lower bound on the mass of the Higgs boson of 114.4 GeV/c^2 at a 95% confidence limit [8].

2.1.5 Higgs searches at the LHC

As introduced previously, the electroweak gauge bosons and fermions acquire masses through the interactions with the Higgs field. The unknown parameter of the Higgs boson is its mass, m_H. If we can find the Higgs boson productions at the LHC, the standard formulation of the electroweak theory can be built. Figure 2.2 shows the Feynman diagrams of the possible Higgs boson productions. The dominant Higgs boson production mechanism at the LHC will be the gluon-fusion process which is shown in Figure 2.2(a) [3]. The cross-sections of the various Higgs production processes are shown in Figure 2.3.

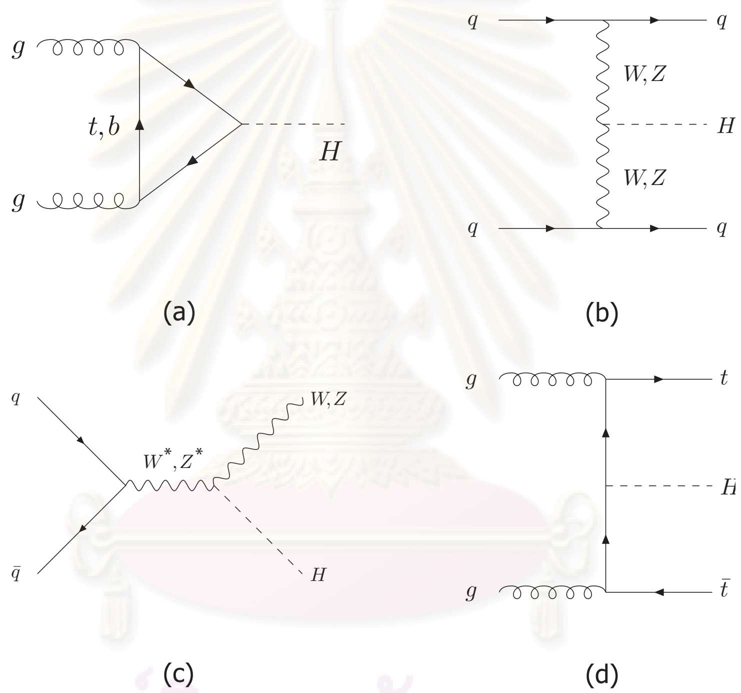

Figure 2.2: The Higgs boson production mechanisms: (a) gluon fusion, (b) vector boson fusion, (c) Higgs-strahlung, (d) Higgs bremsstrahlung off top quarks. The figure is taken from Section 10.1 of [3].

To discover Higgs boson, various Higgs decay channels have been studied by the CMS collaboration. The expected channels to discover Higgs boson include,

1. $H \rightarrow ZZ^* \rightarrow e^+e^-\mu^+\mu^-$: For the integrated luminosity of 30 fb^{-1}, the 5σ significance can be expected for the Higgs mass in range $130 \leq m_H \leq$

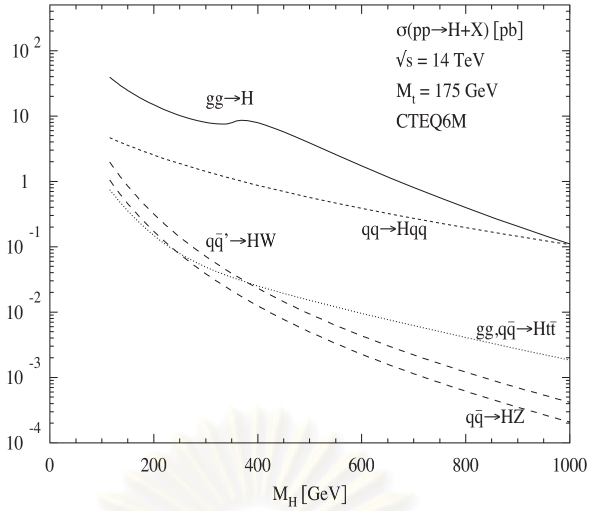

Figure 2.3: The Higgs boson production cross sections at the LHC. The figure comes from Section 10.1 of [3].

500 GeV/c^2. This channel is a very clean signature with relatively small background which yeilds the same signature of two electrons and two muons. The example of the background is $q\bar{q} \to ZZ^*/\gamma^* \to e^+e^-\mu^+\mu^-$.

2. $H \to WW^* \to 2l2\nu$: The 5σ significance can be expected to observe with the integrated luminosity of 7 fb^{-1} for the Higgs mass in range $150 \le m_H \le$ 180 GeV/c^2. The main background comes from diboson events, including WW, WZ, and ZZ.

3. $H \to \tau\tau \to l + \tau\,\text{jet} + E_T^{miss}$: The 5σ significance can be expected to observe with the integrated luminosity of 60 fb^{-1} for the Higgs mass in range $115 \le$ $m_H \le 135$ GeV/c^2. The considered background includes QCD (2τ+2 or 3 jets), boson + jets, and $t\bar{t}$ + jets.

4. $H \to W^+W^- \to l^\pm \nu jj$: The 5σ significance can be expected to observe with the integrated luminosity of 30 fb^{-1} for the Higgs mass in range $140 \le$ $m_H \le 200$ GeV/c^2. The major background includes $t\bar{t}$+jets, single boson + jets, diboson + jets, and QCD events.

5. $H \to \gamma\gamma$: The signal significance is about 3σ for the integrated luminosity of 60 fb^{-1} when the mass in range $115 \le m_H \le 130$ GeV/c^2. Then it

drops to 2.3σ when the mass in range $130 \leq m_H \leq 150$ GeV/c^2. The main background comes from the QCD process.

The comprehensive details for all study channels, including the Monte Carlo study, the discovery potential, background estimation, and the event selection by the CMS collaboration, can be found in [3]. Note that, searching for the Higgs boson is also continuing at the Tevatron experiments, D0 and CDF, at the Fermilab.

2.2 Supersymmetry

Even though the Standard Model is a successful theory, it is not complete by itself. There are more than ten arbitrary parameters, i.e. six quark masses, three charged lepton masses, boson masses. That leaves many important questions for us to discover, i.e. Higgs boson, or gravity incorporation. Higgs discovery is not the final step of the Standard Model, the question about the Higgs mass still remains. Due to the effects of every particles which couple to the Higgs field, the quantum corrections to the Higgs mass squares will be gotten. After applying the Feynman rules, the Higgs mass (m_H) and the quantum corrections (Δm_H) are given by

$$m_H^2 = (m_H^2)_0 + \Delta m_H^2, \tag{2.6}$$

$$\Delta m_H^2 = \frac{|\lambda_f|^2}{8\pi^2}\left[-\Lambda_{UV}^2 + \ldots\right]. \tag{2.7}$$

The λ_f is the Yukawa coupling of particles that couple to the Higgs field. The Λ_{UV} is called the ultraviolet cut-off and is the scale up to which the Standard Model is valid. If we consider at the Planck scale ($\Lambda_{UV} \sim M_P \sim 10^{19}$ GeV/c^2), the Higgs mass will diverge. This is known as the hierarchy problem. The new physics beyond the Standard Model (BSM) should introduce a suitable cut-off. With the beyond Standard Model theories, new groups of particles have been predicted. One theory of the BSM is the supersymmetry. With the supersymmetry, new predicted particles are proposed to be partners of the Standard Model particles and have the spin difference by $\frac{\hbar}{2}$, that is fermions have boson-like partners and vice versa. These partners of the Standard Model particles are called **superpartners** or **sparticles**. With their existences, the divergent problem of the Higgs mass is reduced by introducing additional terms which have the Λ_{UV} in the same order but different sign in quantum corrections. With the supersymmetry, the three forces, including strong, electromagnetic and weak, have exactly equal strengths in this theory at a very high energy (Figure 2.4).

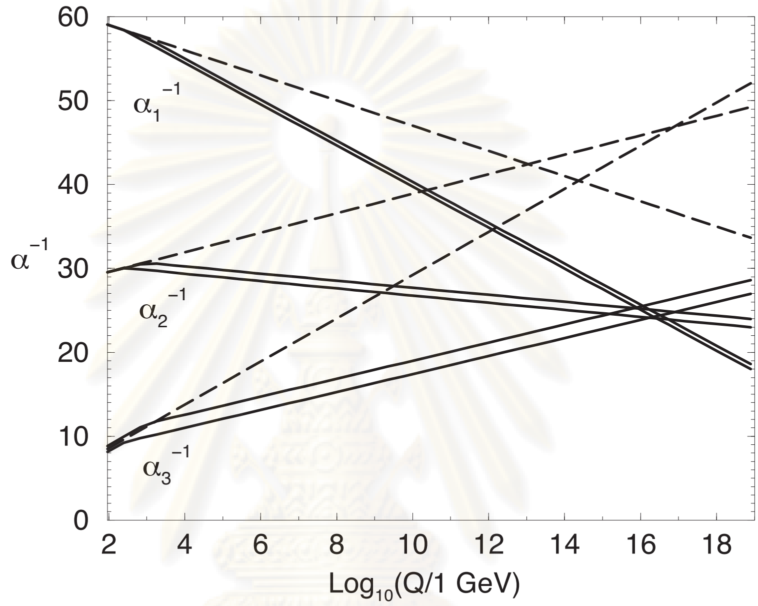

Figure 2.4: The inverse gauge coupling running as the function of energy Q. The dashed lines are for the SM, and the solid lines are for the Minimal Supersymmetric Standard Model (MSSM).

Not only the hierarchy problem and the unification of gauge coupling that can be solved by existence of the supersymmetry, superpartners are also candidates of the dark matter which is thought to exist in the universe. To describe this, the R-parity is needed to be defined first. The R-parity (R_p) is defined by

$$R_p \equiv (-1)^{3(B-L)+2s} \tag{2.8}$$

where B, L and S are Boson number, Lepton number, and spin of the particles, respectively. This implies that all Standard Model particles have $R_p = +1$ while their superpartners have $R_p = -1$. The R_p conservation states that, at every vertices, the multiplication product of R_p around a vertex must be equal to $+1$. With the conservation of the R-parity, sparticles must be produced in pairs. Then, a massive stable superpartner must be absolutely stable, and it can be a candidate for the dark matter. We call it the light supersymmetric particle (LSP). In addition, if it is electrically neutral, it will interact weakly with ordinary matter. That is an excellent candidate for dark matter. More details about supersymmetry can be found in [9].

Names of the superpartners of fermions are formed from the fermion name with a preceding "s". For example, *stop* is the superpartner of top quark, and it can be written by adding tilde above the symbol of fermion, e.g. $\tilde{t}$. For the case of the superpartners of the Standard Model bosons, the names of supersymmetric partners are composed by the name of boson and are appended with "ino", i.e. Wino is the superpartner of W boson. Table 2.4 shows the Standard Model particles and supersymmetric particles

Standard Model particles	**Supersymmetric particles**
γ, Z^0, h^0, H^0	$\tilde{\chi}_1^0, \tilde{\chi}_2^0, \tilde{\chi}_3^0, \tilde{\chi}_4^0$
W^+, H^+	$\tilde{\chi}_1^+, \tilde{\chi}_2^+$
$e^-, \nu_e, \mu^-, \nu_\mu, \nu_\tau$	$\tilde{e}_R^-, \tilde{e}_L^-, \tilde{\nu}_e, \tilde{\mu}_R^-, \tilde{\mu}_L^-, \tilde{\nu}_\mu, \tilde{\nu}_\tau$
τ^-	$\tilde{\tau}_1, \tilde{\tau}_2$
$u, d, s, c,$	$\tilde{u}_R, \tilde{u}_L, \tilde{d}_R, \tilde{d}_L, \tilde{s}_R, \tilde{s}_L, \tilde{c}_R, \tilde{c}_L$
b	$\tilde{b}_1, \tilde{b}_2$
t	$\tilde{t}_1, \tilde{t}_2$

Table 2.4: The Standard Model particles and supersymmetric particles.

2.2.1 The minimal Supergravity (mSUGRA)

The Minimal Supersymmetric Standard Model (MSSM) is the minimal extension to the Standard Model which incorporates supersymmetry by adding the corresponding superpartners to the existing Standard Model particles. Even in the MSSM which is a minimal extension, there still are more than 100 free parameters. We call this unconstrained conditions of MSSM as uMSSM. In the minimal supergravity (mSUGRA), there are only five parameters which allow us to calculate the MSSM particle mass spectra and their interactions [10]. With different values of parameters, different phenomena can be seen. The mSUGRA model offers us a benchmark points of the possible SUSY phenomenology to be studied. The five parameter of mSUGRA are

- m_0: A common mass for all scalar sparticles at the GUT scale.
- $m_{1/2}$: A common gaugino mass at the GUT scale.
- A_0: A constant of proportionality between the SUSY breaking trilinear $Hf\bar{f}$ coupling terms and the SUSY conserving Yukawa couplings.
- $\tan\beta$: The ratio of the vacuum expectation values of the two MSSM Higgs doublets.
- sign(μ): Sign of the SUSY higgsino mass parameter.

Figure 2.5 shows the discovery contour and mSUGRA benchmark points studied by the CMS collaboration. The discovery regions can be separated into three regions by comparing a mass of gluino and masses of squarks [3]. The three regions are

1. Region 1: $m(\tilde{g}) > m(\tilde{q})$ The decays of $\tilde{g} \to \tilde{q}q$ are expected to be dominant. Examples of this points include LM1, LM2, or LM6 which are our study points in this thesis.
2. Region 2: $m(\tilde{g}) < m(\tilde{q})$ The decays of $\tilde{q} \to \tilde{g}q$ are expected to be dominant. An example point in this region is HM4.
3. Region 3: Some squarks are heavier, others are lighter than gluino. At this point, gluino will decay to the lighter squarks. An example point in this region is LM8 in which $\tilde{b}_1$ and $\tilde{t}_1$ are lighter than gluino, but others are not.

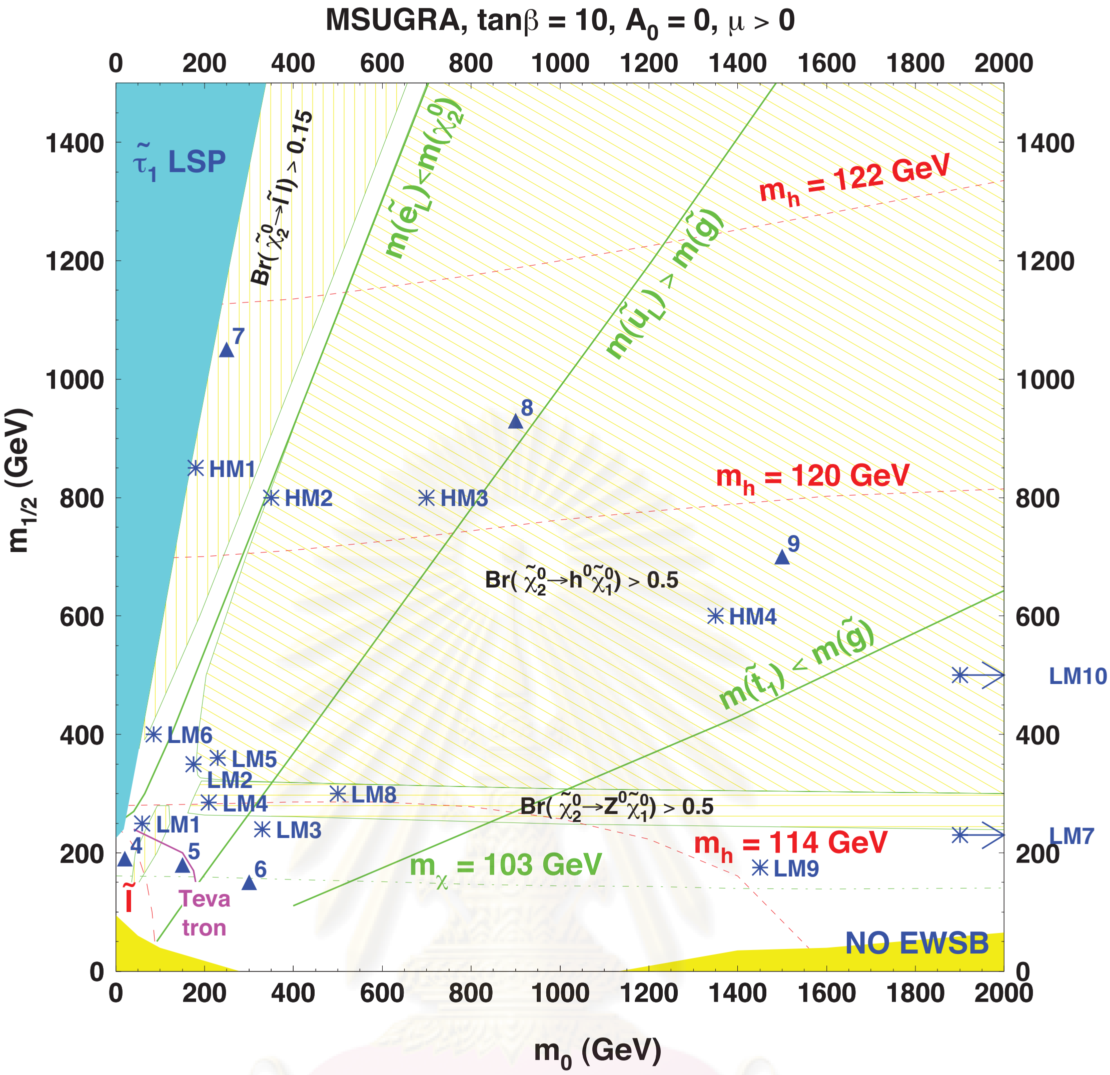

Figure 2.5: The discovery contour which shows the mSUGRA benchmark points studied by the CMS collaboration.

In this thesis, three different benchmark points, called LM1, LM2 and LM6, will be used as examples of differences in decay channels of neutralino and chargino. Tables 2.5 and 2.6 show SUSY masses calculated by `ISAWIG` and mSUGRA parameters of the decay chain of interest at the benchmark points, LM1, LM2 and LM6, respectively. Figure 2.6 shows the mass spectra of each study point.

The characteristic of each study points is as follows,

- LM1: The decays $\tilde{\chi}_2^0 \to l\tilde{l}_R$ and $\tilde{\chi}_2^0 \to \tau_1\tilde{\tau}_1$ are allowed, while $\tilde{\chi}_2^0 \to l\tilde{l}_L$ and $\tilde{\chi}_2^0 \to \tau_2\tilde{\tau}_2$ are forbidden. About 30 % of the decay products of the gluino

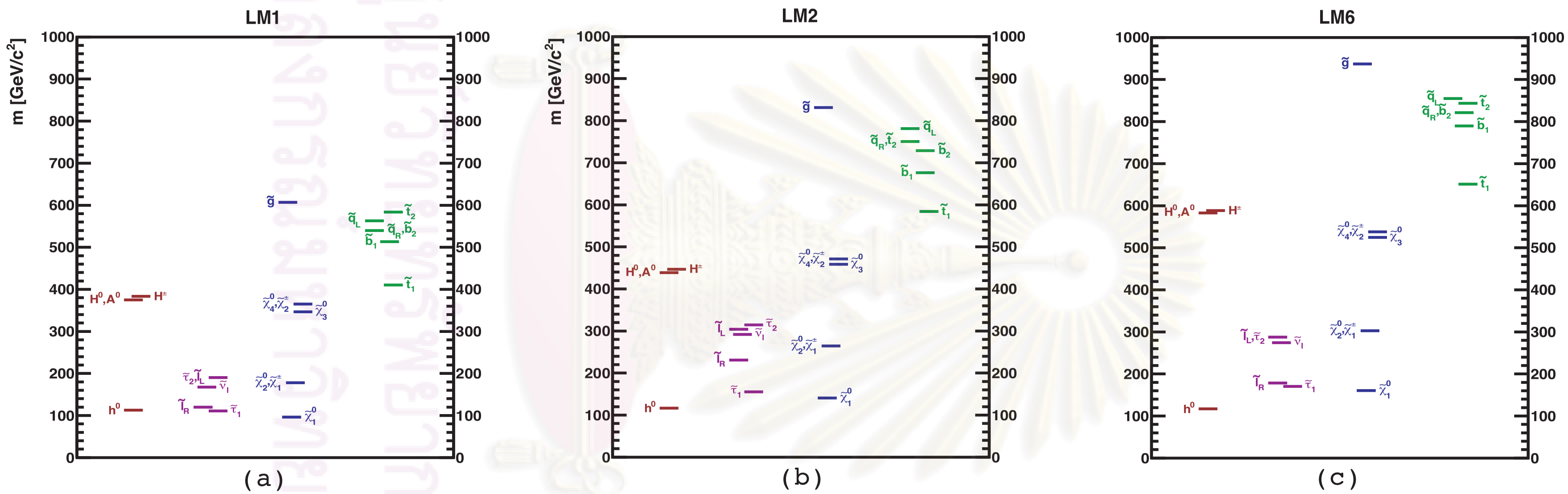

Figure 2.6: The masses of sparticles of each study points.

Model (post-WMAP point [11])	$m_{1/2}$	m_0	A_0	sign μ	tan β
LM1 (B')	250	60	0	+	10
LM2 (I')	350	185	0	+	35
LM6 (C')	400	85	0	+	10

Table 2.5: mSUGRA parameter and our interesting branching ratios at benchmark points, LM1, LM2 and LM6.

Model	$m_{\tilde{g}}$	$m_{\tilde{\chi}_1^0}$	$m_{\tilde{\chi}_2^0}$	$m_{\tilde{\chi}_4^0}$	$m_{\tilde{\chi}_1^+}$	$m_{\tilde{\chi}_2^+}$
LM1	608.074	96.840	178.272	364.331	178.114	363.395
LM2	831.418	141.152	265.021	471.606	265.404	471.781
LM6	937.453	161.434	303.502	537.417	303.985	536.692

	$m_{\tilde{d}_L}$	$m_{\tilde{u}_L}$	$m_{\tilde{s}_L}$	$m_{\tilde{c}_L}$	$m_{\tilde{b}_1}$	$m_{\tilde{t}_1}$
LM1	565.349	559.289	565.349	559.291	516.822	405.003
LM2	783.918	779.495	783.918	779.495	680.616	577.726
LM6	864.770	860.816	864.770	860.816	794.531	644.254

	$m_{\tilde{d}_R}$	$m_{\tilde{u}_R}$	$m_{\tilde{s}_R}$	$m_{\tilde{c}_R}$	$m_{\tilde{b}_2}$	$m_{\tilde{t}_2}$
LM1	541.795	542.136	541.795	542.136	542.259	581.007
LM2	753.436	755.206	753.436	755.206	734.753	752.166
LM6	829.172	831.731	829.172	831.731	826.798	844.434

	$m_{\tilde{e}_L}$	$m_{\tilde{e}_R}$	$m_{\tilde{\mu}_L}$	$m_{m\tilde{u}_R}$	$m_{\tilde{\tau}_1}$	$m_{\tilde{\tau}_2}$
LM1	187.051	117.957	187.051	117.957	110.831	189.503
LM2	304.380	304.380	156.478	229.726	229.726	312.838
LM6	288.178	175.189	288.178	175.189	170.684	288.193

Table 2.6: Masses (GeV/c^2) of selected particles at the interesting benchmark points, LM1, LM2 and LM6.

are sbottom-bottom pairs. The dominant decay process of the squark is $\tilde{q} \to \tilde{\chi}_1^{\pm} + q$, followed by $\tilde{q} \to \tilde{\chi}_2^0 + q$ except for the $\tilde{t}$ which has a branching ratio of $\tilde{t} \to \tilde{\chi}_1^0 + t$ comparable with $\tilde{t} \to \tilde{\chi}_2^0 + t$.

- BR($\tilde{\chi}_2^0 \to l\tilde{l}_R$) = 11.2 % (for e and μ)
- BR($\tilde{\chi}_2^0 \to l\tilde{l}_L$) = 0 % (for e and μ)
- BR($\tilde{\chi}_2^0 \to \tau_1\tilde{\tau}_1$) = 48.6 %

• LM2: The decay chain $\tilde{\chi}_2^0 \to l\tilde{l}_R$ is highly suppressed by $\tilde{\chi}_2^0 \to \tau_1\tilde{\tau}_1$. The decay $\tilde{\chi}_2^0 \to l\tilde{l}_L$ and $\tilde{\chi}_2^0 \to \tau_2\tilde{\tau}_2$ are forbidden. About 25 % of the squark (quark) products from the gluino decay are sbottom-bottom pairs. The dominant decay process of squark is $\tilde{q} \to \tilde{\chi}_1^{\pm} + q$, followed by $\tilde{q} \to \tilde{\chi}_2^0 + q$ except for $\tilde{t}$ which has a branching ratio of $\tilde{t} \to \tilde{\chi}_2^0 + t$ lower than $\tilde{t} \to \tilde{\chi}_1^0 + t$ and $\tilde{t} \to \tilde{\chi}_2^{\pm} + b$. About 25 % and 20 % of gluino decay are sbottom-bottom and stop-top pairs, respectively.

- BR($\tilde{\chi}_2^0 \to \tau_1\tilde{\tau}_1$) = 95.8 %
- BR($\tilde{\chi}_2^0 \to \mu\tilde{\mu}$) = 0.2 %
- BR($\tilde{\chi}_2^0 \to e\tilde{e}$) = 0.2 %
- BR($\tilde{\chi}_1^+ \to \tilde{\tau}_1\nu_\tau$) = 95.3 %

• LM6: The decay from $\tilde{\chi}_2^0$ to slepton-lepton pairs are allowed for all channels. The dominant decay process of squark is $\tilde{q} \to \tilde{\chi}_1^{\pm} + q$, followed by $\tilde{q} \to \tilde{\chi}_2^0 + q$ except for $\tilde{b}$, and $\tilde{t}$. For sbottom decay, the branching ratio of $\tilde{b} \to \tilde{\chi}_2^{\pm} + t$ is comparable with $\tilde{b} \to \tilde{\chi}_2^0 + b$. In the stop case, the branching ratio of $\tilde{t} \to \tilde{\chi}_2^0 + t$ is lower than $\tilde{t} \to \tilde{\chi}_1^0 + t$ and $\tilde{t} \to \tilde{\chi}_2^{\pm} + b$.

- BR($\tilde{\chi}_2^0 \to l\tilde{l}_L$) = 12 % (for e and μ)
- BR($\tilde{\chi}_2^0 \to l\tilde{l}_R$) = 2 % (for e and μ)
- BR($\tilde{\chi}_2^0 \to \tau_1\tilde{\tau}_1$) = 14.6 %
- BR($\tilde{\chi}_2^0 \to \tau_2\tilde{\tau}_2$) = 5.8 %

- BR($\tilde{t}_1 \rightarrow \tilde{\chi}_1^+ b$) = 43.8 %
- BR($\tilde{t}_1 \rightarrow \tilde{\chi}_1^0 t$) = 25.5 %
- BR($\tilde{\chi}_1^+ \rightarrow \tilde{\nu}_\tau \tau$) = 24.4 %
- BR($\tilde{\chi}_1^+ \rightarrow \tilde{\nu}_l l$) = 40 % (for e and μ)

CHAPTER III

Large Hadron Collider and Compact Muon Solenoid experiment

3.1 The Large Hadron Collider (LHC)

At present, the goal of experimental high energy particle physics is to discover the remaining particles in the Higgs sector of the Standard Model and particles which are predicted in the beyond Standard Model theories such as supersymmetry, or extra-dimensions. To discover these signatures, physicists need the collisions at high energies. There are few choices of accelerators we can build with present technology. Electron-positron is one of the choices because their collisions provide clean signals. This is due to the fact that they are structureless. However, the drawback of this kind of accelerator is the limited energy that can be obtained because of synchroton radiation losses. The second choice is a muon collider. With present technology, it is unrealistic to produce and accelerate muons before they decay. The final choice is a hadron collider. In the past, proton (and anti-proton) colliders have proved to be successful. However, anti-proton production is not an easy task and it limits machine luminosity.

Finally, European physicists have decided to build a proton-proton collider at the European Organization for Nuclear Research (CERN) located on the French-Swiss border, west of Geneva. This accelerator is named the Large

Hadron Collider (LHC). This project was approved by the CERN council in December 1994, and would be built in the same tunnel of the old accelerator, the Large Electron-Positron collider (LEP). The LHC will be a proton-proton collider with 14 TeV center-of-mass energy and luminosity of up to $10^{34}\,\mathrm{cm^{-2}s^{-1}}$. It is also a high energy Pb-Pb collider. Table 3.1 summarizes the specifications of the LHC.

Because the LHC is located in the old LEP tunnel, there is not enough space to install two sets of magnets to accelerate two beams of protons in the opposite directions. In addition, physicists and engineers cannot use a unique vacuum tube to accelerate particles which have the same sign in opposite directions. Therefore the LHC is designed with two sets of coils and beam channels sharing the same mechanical structure. Figures 3.1 and 3.2 show the cross-section of the dipole magnet and a plot of dipole magnetic field, respectively [12]. Figure 3.3 presents diagram of the LHC, accelerator chain and experimental stations [13].

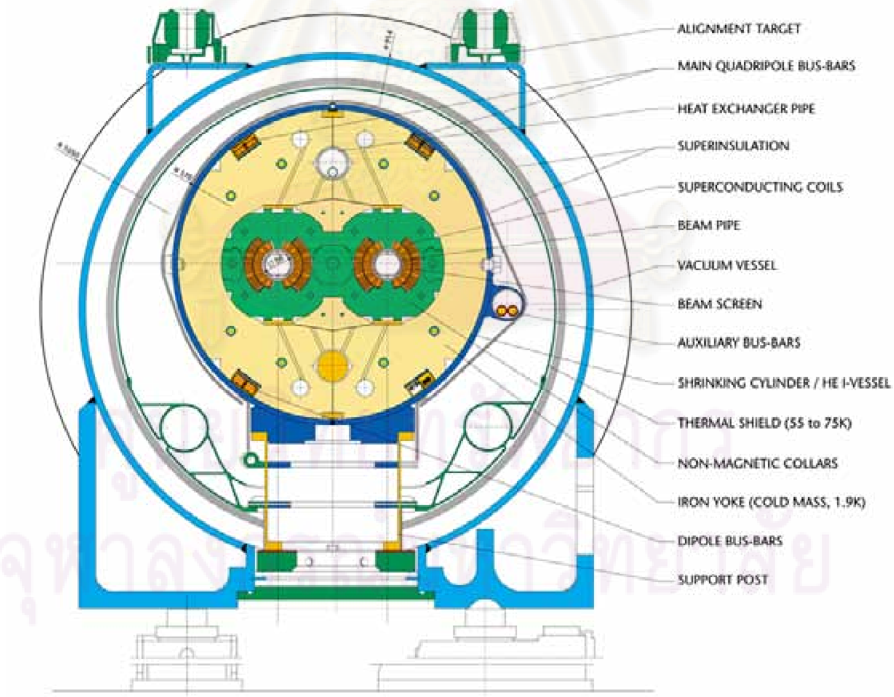

Figure 3.1: Cross-sections of the LHC dipole magnet. Two beam lines can be seen in the central part.

General details	
Name	Large Hadron Collider (LHC)
Circumference	26659 m
Number of magnets	9300
Number of dipoles	1232
Number of quadrupoles	858
proton-proton collisions	
Nominal energy	7 TeV
No. of bunches	2808
Designed Luminosity	$10^{34}\,\mathrm{cm^{-2}s^{-1}}$
Luminosity lifetime	15 hr
Pb-Pb collisions	
Nominal energy (energy per nucleon)	2.76 TeV/u
No. of bunches	592
Designed Luminosity	$10^{27}\,\mathrm{cm^{-2}s^{-1}}$
Luminosity lifetime	6 hr

Table 3.1: The machine parameters of the LHC.

The first proton beam travelled completely around the LHC ring at 10:28 a.m. on September 10th, 2008. On September 19, there was an accident during the commissioning (without beam) of the LHC sector 3-4 at high current for the operation at 5 TeV. After the investigations, the LHC experts concluded that a faulty electrical connection between two magnets caused the mechanical damage and released the helium into the tunnel. After a year of repairs, the LHC started again on November 20th, 2009. The first collisions at 900 GeV, which is equal to the sum of the energy from each proton beam injected from the Super Proton Synchrotron (SPS) to the LHC, were made on November 23rd, 2009. The four main detectors, ALICE, ATLAS, CMS, and LHCb could record the data from these collisions. After a week of operation, the LHC could raise the energy of

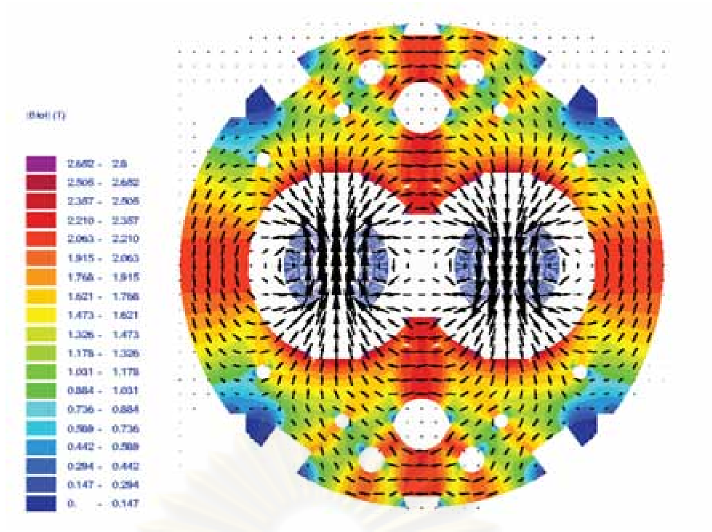

Figure 3.2: Dipole magnetic flux plot.

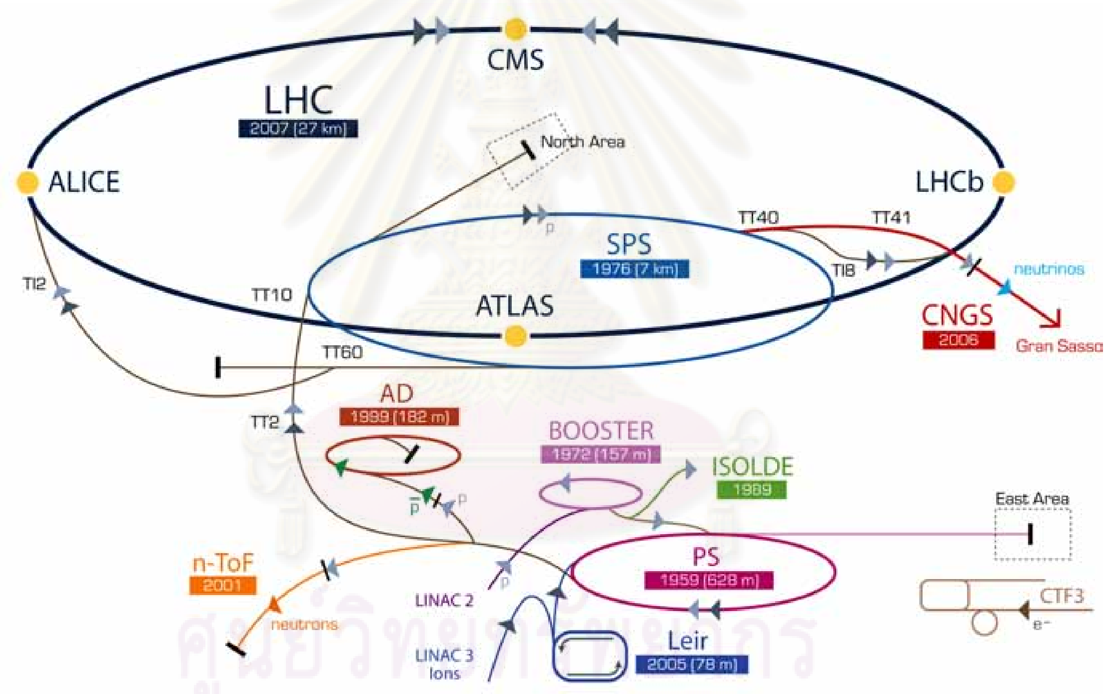

Figure 3.3: LHC complex system.

proton beams to 1.18 TeV in the early morning of November 30th. On March 30, 2010, the LHC can collide the proton beams at 7 TeV. The LHC will run at this energy level for 2-3 years to collect the data before the long shutdown to upgrade the LHC to reach the designed energy at 14 TeV.

3.2 Experiments at the LHC

There are seven experiments installed in the four intersect regions of the LHC as follows:

1. **ALICE (A Large Ion Collider Experiment):** The experiment which is designed to study quark-gluon-plasma (QGP) state using heavy ion collisions. ALICE information can be found on `http://aliceinfo.cern.ch/Public/`.

2. **ATLAS (A Toroidal LHC ApparatuS):** A general purpose detector for the LHC. It is designed to study the Higgs sector, and physics beyond the Standard Model such as supersymmetry, extra dimensions. ATLAS information can be found on `http://atlas.ch/`.

3. **CMS (Compact Muon Solenoid):** A general purpose detector as the ATLAS. CMS information can be found in `http://cmsinfo.cern.ch/outreach/`.

4. **LHCb (LHC-beauty):** The experiment is designed to study *b*-physics, specially to measure CP-violation parameters. LHCb information can be found on `http://lhcb-public.web.cern.ch/lhcb-public/`.

5. **LHCf (LHC-forward):** A special-purpose experiment to study forward high energy particle production in proton-proton collisions. The results from the LHCf can be used to tune the simulation for cosmic rays. It is located near the ATLAS experiment. LHCf information can be found on `http://www.stelab.nagoya-u.ac.jp/LHCf/LHCf/index.html`.

6. **MoEDAL (Monopole and Exotics Detector at the LHC):** The newest experiment for the LHC until now, it was approved by CERN council on December 2nd, 2009. The aim is to search for magnetic monopoles and highly ionizing particles. MoEDAL information can be found on `http://web.me.com/jamespinfold/MoEDAL_site/Welcome.html`.

7. **TOTEM (Total Cross Section, Elastic Scattering and Diffraction Dissociation):** The experiment which is designed to measure the total cross section, elastic scattering and diffractive processes at the LHC. It will be installed near the CMS detector. TOTEM information can be found on `http://cern.ch/totem-experiment/`.

3.3 The Compact Muon Solenoid Experiment

3.3.1 Overview

The Compact Muon Solenoid (CMS) is one of two general purpose detectors for the LHC at CERN. Table 3.2 summarizes general specifications of the CMS detector. A brief description of the sub-systems of the CMS detector is given below. Figures 3.4 and 3.5 show the layout and the complete CMS detector, respectively.

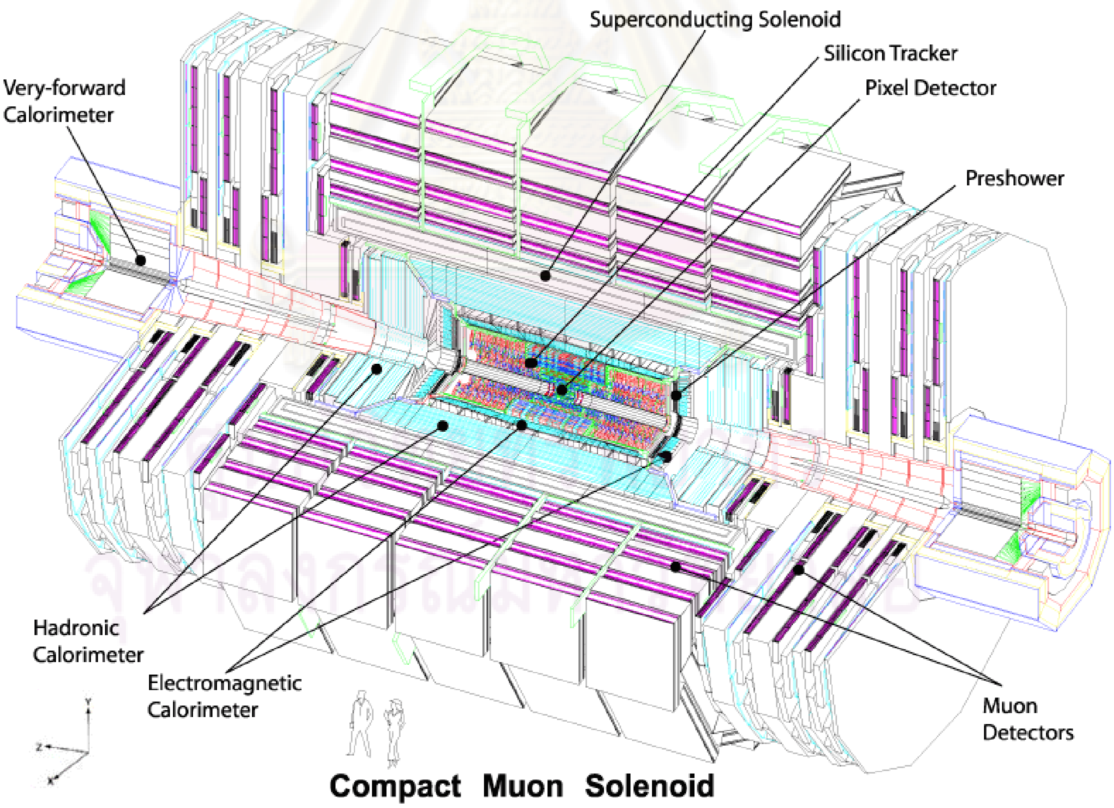

Figure 3.4: The complete layout of the CMS detector.

Figure 3.5: The complete CMS detector in the experimental hall.

1. **Inner Tracking System**: The inner tracker is designed to precisely measure the transverse momentum of charged particles, e.g. leptons, which are bent in the magnetic field. The radius of curvature of the particle's track allows physicists to determine its momentum. We can combine tracker information with information from other detector systems, e.g. calorimeter or muon system information, to identify charged particles of interest.

2. **Calorimeter System**: The purpose of the calorimeter is to precisely measure the energy of particles by absorbing and measuring the shower from an incoming particle. A shower is a cascade of secondary particles produced from a high energy particle when it interacts with a dense matter. When an incoming particle interacts with a dense matter, new particles with less energy are produced. Some of them which have very low energies stop and are absorbed. The remaining particles interact in the same way. These processes continue many times until all of secondary particles are absorbed. The illustration of a shower from a high energy electron is shown in Figure

3.6. There are two types of calorimeter systems in the CMS:

(a) **Electromagnetic Calorimeter (ECAL)**: An electromagnetic calorimeter is optimized for measuring electron and photon energies. The calorimeter detects an electromagnetic shower produced by a cascade of bremsstrahlung and pair production processes. When electrons and photons pass through an ECAL crystal, that crystal will produce light in proportion to the particles energies. A photodetector will then detect the light and then converts it to electrical signal to be measured and recorded by electrical devices.

(b) **Hadronic Calorimeter (HCAL)**: A hadronic calorimeter is optimized for measuring the energy of hadrons, particles made of quarks and gluons such as proton or neutron. HCAL also provides indirect measurement of the neutrinos. The dominant process is inelastic hadron interactions. The HCAL is a sampling calorimeter. A sampling calorimeter composes of "active" and "passive" layers. The passive layer is responsible for creating showers, while the active layer is responsible for an energy measurement and signal generation.

3. **Magnet System**: A long superconducting solenoid has been chosen to produce a uniform magnetic field of 3.8 Tesla in the direction of beam axis. This magnetic field is returned by an iron yoke which is also used as muon filter. The superconducting solenoid has the dimensions of 13 metres long and inner diameter of 6 metres.

4. **Muon System**: Muon chambers are used to identify muons, to trigger on muons, and to measure their momentum. In the muon system, there are three different technologies used to detect and measure muons:

   (a) Drift tubes (DTs) in barrel region.

   (b) Cathode strip chambers (CSCs) in the endcap region.

   (c) Resistive plate chambers (RPCs) in both the barrel and endcap regions.

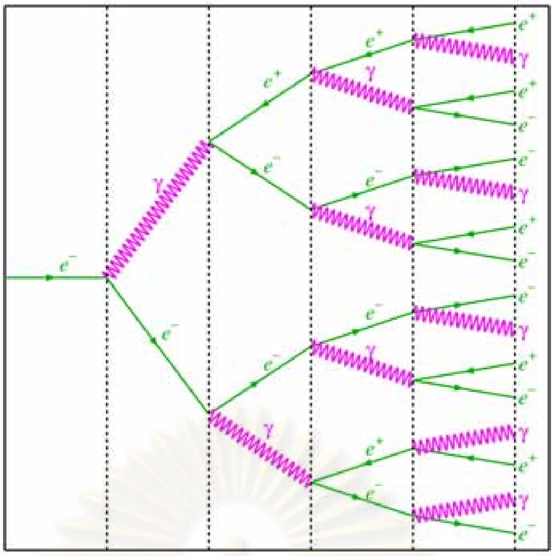

Figure 3.6: The illustration of an electromagnetic shower from a high energy electron.

Name	Compact Muon Solenoid (CMS)
Length	21.6 m
Diameter	15 m
Weight	12,500 Tons
Magnetic Field	3.8 Tesla
	$\sim$ 100,000 times stronger than the Earth's magnetic field
Stored energy (coil)	$\sim$2.7 GJ
Weight (magnet system)	14,000 tons
Location	Point 5, Cessy, France

Table 3.2: The general details of the CMS detector.

3.3.2 The Coordinate System of the CMS

In the coordinate system of CMS, the origin is the point of nominal collision, the x-axis is defined radially inward toward to the center of the LHC ring, while the y-axis is defined vertically upward from the origin. The z-axis is defined along the beam pipe, direction to the Jura mountain. The transverse direction of any quantities are calculated from the x and y components of the corresponding quantities. The coordinate system of the CMS is illustrated in Figure 3.4.

3.3.3 Physics Studies in the CMS Collaboration

The CMS detector was designed to be a general purpose detector, the physics which will be studied at the CMS will be covered from the Standard Model to physics beyond the Standard Model. Examples of physics studies in the CMS are,

1. **Standard Model**: This part of the studies will cover all existing Standard Model signatures. It includes physics of strong interactions, top quark physics, B physics and electroweak physics.

2. **Higgs Bosons**: The Higgs sector is the remaining missing part of the Standard Model. This study does not include only the Standard Model Higgs bosons, but it also includes the study of the Higgs sector for beyond the Standard Model scenarios such as minimal supersymmetric Standard Model (MSSM) Higgs or other non-supersymmetry ideas.

3. **Supersymmetry**: As describe in Section 2.2. If the supersymmetric particles exists at the LHC, the decay products of any sparticle decays, including jets, leptons and missing energy should help us to constrain some free parameters of the theory.

4. **Other beyond Standard Model physics**: This group will cover beyond the Standard Model theory except supersymmetry. Examples of studies are Extra Dimensions or searching for new vector bosons.

5. **Heavy-ion physics**: The LHC will provide high energy collision of heavy ions, which opens a possibility to study Quantum Chromodynamics (QCD) in extreme conditions, such as high temperature or high density.

3.3.4 Detector Components

In this section, each sub-systems of the CMS detector will be described starting from the part which is closest to the beam pipe and moving radially outwards.

3.3.4.1 Inner Tracking System

As mentioned above, the main goal of the tracker is to precisely measure the coordinates of charged particles along their path. With this information, momenta of particles in the central part of the CMS detector can be determined. Information from the tracker can be combined with electromagnetic calorimeter data to completely identify photons and electrons and can be combined with the muon system for muon identification. The tracker can be used to identify secondary vertices which help physicists to tag decays of B-mesons and can be used to estimate isolation and multiplicity which are very important parameters in analyzing the data. The layout of the CMS tracking system is shown in Figure 3.7. The CMS tracker consists of two subsystems [6, 14] as follows:

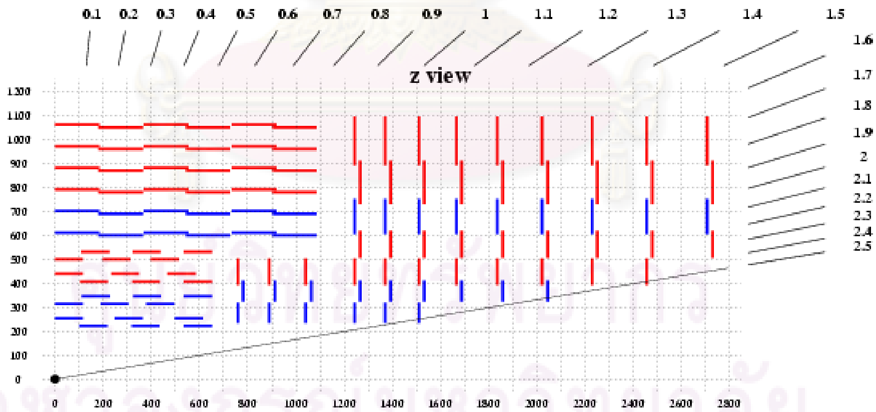

Figure 3.7: The layout of the CMS inner tracking system.

Pixel Detector

In the closest section of the CMS detector to the LHC beam line, the interaction region will be covered by three layers of silicon pixel detectors. These three barrel layers have mean radii of 4.4 cm, 7.3 cm, and 10.2 cm, respectively. The total length of the barrel layer is 53 cm. Two endcaps, extending from 6 to 15 cm of radius, will be placed on each size at $|z| = 34.5$ cm and 46.5 cm. Figure 3.8 shows a three-dimensional view of pixel detector.

The cell size of these detectors is 100 μm by 150 μm, and the resolution is 15 μm using analog readout. The full detector consists of 768 modules of three barrel layers, and 672 modules of four endcap disks. With the pixel detector, the efficiency of finding three pixel hits on a track is larger than 90% in the pseudorapidity region $|\eta| < 2.2$. A detail summary for the CMS pixel detector can be found in [15].

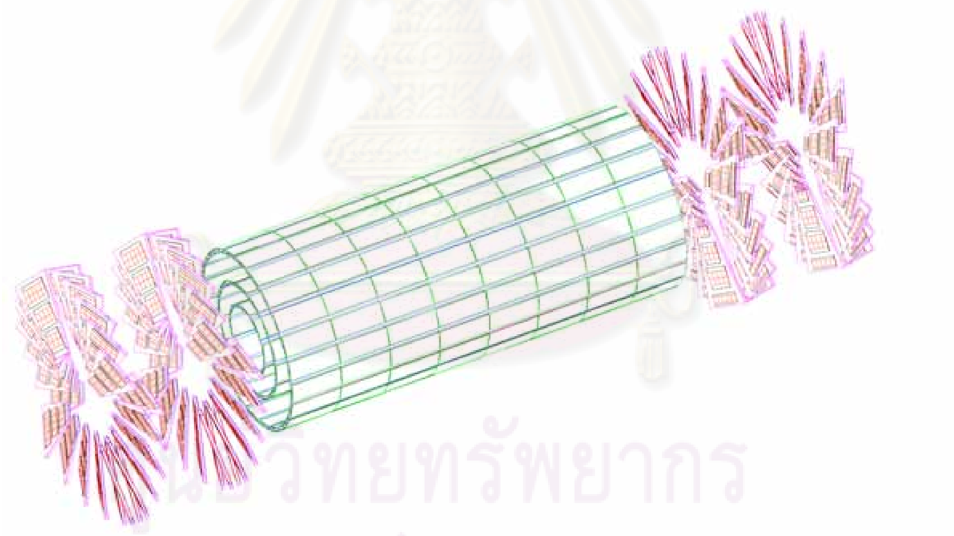

Figure 3.8: Three-dimensional view of the pixel detector with its barrel and endcap regions.

Silicon Strip Detector

The silicon strip detector is placed around the pixel detector, covers the mean radii from 20 cm to 110 cm. In the barrel region, the silicon strip tracker is divided into two parts, the Tracker Inner Barrel (TIB) and the Tracker Outer Barrel (TOB). The TIB consists of four cylindrical layers of the silicon sensors with a thickness of 320 μm and covers up to $|z| < 65$ cm. The TOB consists of six cylindrical layers of the silicon sensors with a thickness of 500 μm and covers up to $|z| < 110$ cm.

For the endcap region, the strip tracker is divided into two parts, the Tracker Endcap (TEC) and the Tracker Inner Disks (TID), which are arranged in rings, centered on the beam line. The TID contains three disks whose 70 cm $< |z| <$ 120 cm, the thickness of the TID is 320 μm. For the TEC, it contains nine disks which 120 cm $< |z| <$ 280 cm.

The thickness of the TEC sensors is 320 μm for the three innermost rings and 500 μm for the six other rings. A detail summary for the CMS silicon strip detector can be found in [14].

The total area of the pixel detectors is ~ 1 m^2, whilst that of the silicon strip detectors is 200 m^2, providing coverage up to $|\eta| < 2.4$. The inner tracker consists of 66 million pixels and 9.6 million silicon strips.

3.3.4.2 Calorimeter System

The calorimeters are located between the tracker and the superconducting solenoid. Electrons, photons, and hadrons will be stopped in the calorimeters allowing to measure their energies. The inner calorimeter is designed to measure the energies of electrons and photons, it is called electromagnetic calorimeter (ECAL) because particles absorbed in this calorimeter interact electromagnetically. The outer calorimeter is designed to absorb hadrons which interact via the strong interaction. It is called hadronic calorimeter (HCAL).

Electromagnetic Calorimeter (ECAL)

A highly accurate measurement and excellent resolution of the energy and position of electrons and photons are the design goals of the CMS electromagnetic calorimeter. Figures 3.9 and 3.10 show the structure of the electromagnetic calorimeter in the barrel and the endcap region.

If the Higgs boson is light ($114\,\mathrm{GeV/c^2} < \mathrm{m}_H < 140\,\mathrm{GeV/c^2}$), a possible decay channel for it is to decay into a photon pair. The excellent resolution of the energy measurement of photons is required in this case. If the mass of the Higgs is higher, the decay into four leptons (via Z bosons) becomes significant.

From studies in the past, the crystal-based scintillating calorimeter is known to offer an excellent performance to achieve these goals. The specification for the crystals are: high density, small Moliere radius, and small radiation length. Lead-tungsten ($PbWO_4$) is chosen for the electromagnetic calorimeter. Lead-tungsten crystals have a Moliere radius of 2.19 cm, a density of 8.28 g/cm^3, and a radiation length of 0.89 cm. Because of the short radiation length, it allows good shower containment in the limited space for the electromagnetic calorimeter. The CMS electromagnetic calorimeter consists of about 80,000 lead-tungsten crystals, in both barrel and two endcaps, with equal number of photodiodes and associated readout electronics. In the barrel region, the Avalanche Photo Diodes (AVD) is used while the Vacuum PhotoTriodes (VPT) is used in the endcap region.

Another part of the electromagnetic calorimeter is the pre-shower detector. It is installed in front of endcaps. Its purpose is to provide separation between photons and neutral pions, since neutral pions will decay into two photons. In addition, pre-shower detectors can improve the estimation of the position of photons. The position of the pre-shower is shown in Figure 3.11.

The energy resolution of the CMS electromagnetic calorimeter is described by the width of gaussian distribution parameters. It can be expressed as

$$\left(\frac{\sigma_E}{E}\right)^2 = \left(\frac{a}{\sqrt{E}}\right)^2 + \left(\frac{b}{E}\right)^2 + c^2 \tag{3.1}$$

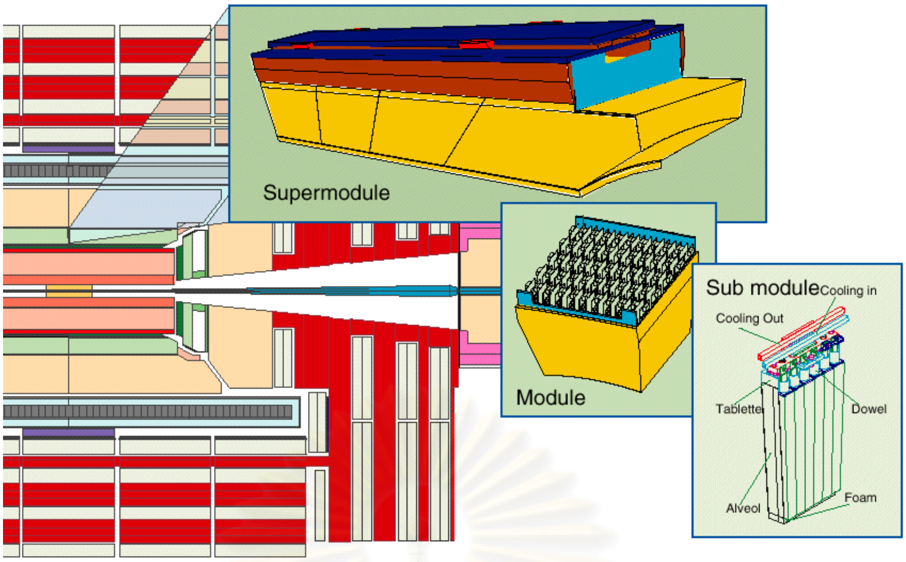

Figure 3.9: Structure of electromagnetic calorimeter in the barrel region.

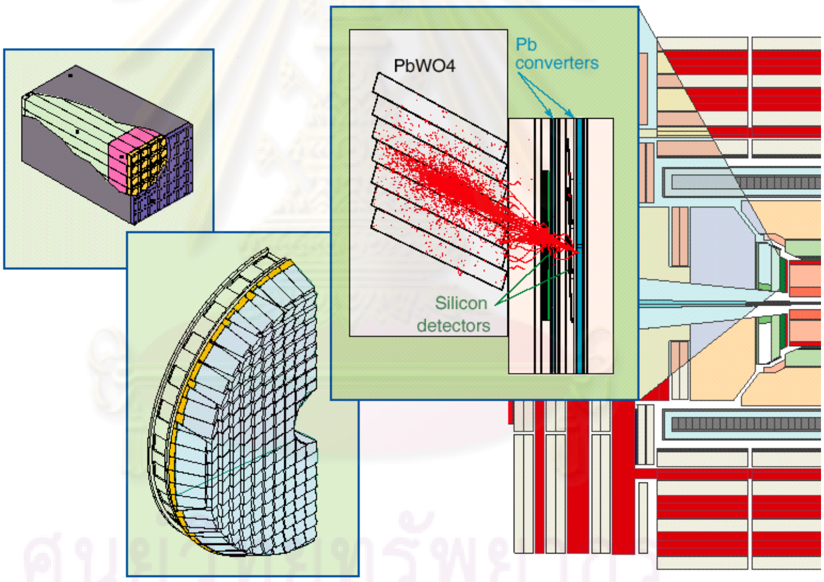

Figure 3.10: Structure of electromagnetic calorimeter in the endcap region.

where the energy is expressed in GeV. The parameter a is called stochastic term and includes the effects of fluctuations in photo-statistics, b is the noise from electronics and pile-up, and c is a constant term from the calibration processes.

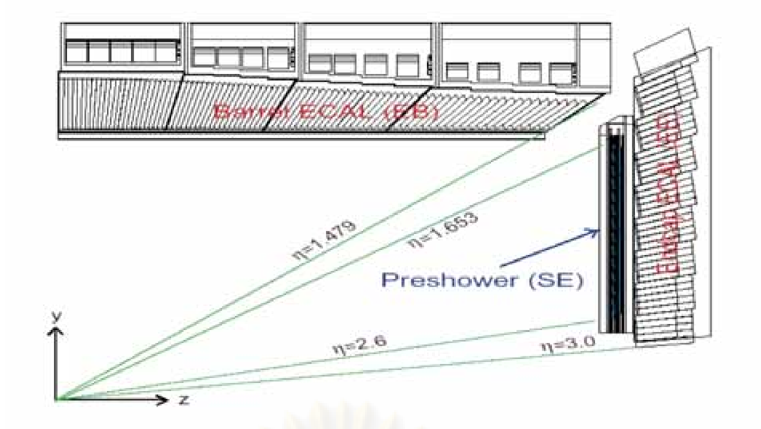

Figure 3.11: Position of the preshower in the endcap region.

The design values [16] for Equation (3.1) are

$$a = 2.7\%\ \text{GeV}^{1/2} \tag{3.2}$$

$$b = 0.155(0.210)\ \text{GeV, for low (high) luminosity} \tag{3.3}$$

$$c = 0.55\% \tag{3.4}$$

From the testbeam data [17], the ECAL energy resolution as a function of electron energy is shown in Figure 3.12. The parameters of the ECAL energy resolution are

$$a = 2.8\%\ \text{GeV}^{1/2} \tag{3.5}$$

$$b = 0.12\ \text{GeV} \tag{3.6}$$

$$c = 0.3\% \tag{3.7}$$

Hadronic Calorimeter (HCAL)

The CMS hadronic calorimeter is designed to measure the direction and energy of jets, and to calculate missing energy. Missing energy is one of key signatures for new physics such as supersymmetry. For this reason, the hadronic calorimeter is designed to cover $|\eta| < 5.0$.

The hadronic calorimeter is divided into four regions. The barrel (HB) and endcap (HE) hadronic calorimeters, which lie inside the solenoid, will cover the

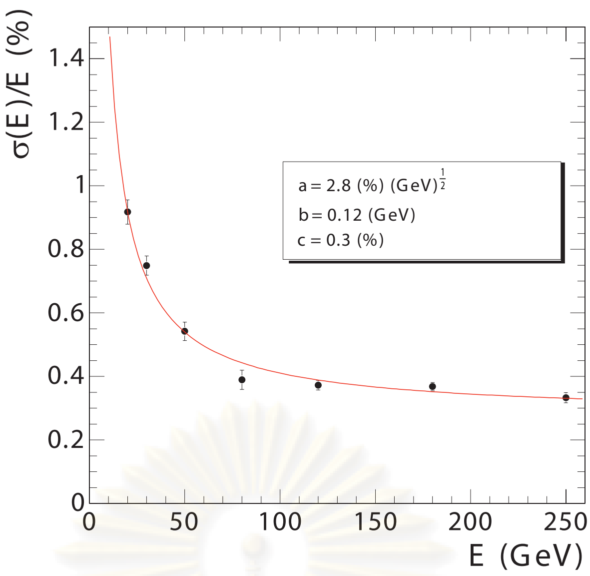

Figure 3.12: The ECAL energy resolution, $\sigma(E)/E$, as a function of electron energy as measured from a beam test.

pseudorapidity region $|\eta| < 3.0$. The barrel is 9 m long and covers the pseudorapidity region $|\eta| < 1.4$. The endcaps are 1.8 m thick and cover the pseudorapidity region $1.3 < |\eta| < 3.0$. Both of them are sampling calorimeter with brass absorber plates interlaced with plastic scintillators. The outer hadronic calorimeter (HO) is placed outside the solenoid, to extend the barrel part of HB and make additional sampling of the shower. Lastly, the two very forward calorimeters (HF) are installed outside the magnet yoke to cover pseudorapidity region $3.0 < |\eta| < 5.0$. The active elements in this calorimeter are quartz fibres inserted in steel absorber plates. Figure 3.13 shows the layout of the CMS hadronic calorimeter except the HFs.

The energy resolution of the HCAL can also be written as

$$\left(\frac{\sigma_E}{E}\right)^2 = \left(\frac{a}{\sqrt{E}}\right)^2 + c^2 \tag{3.8}$$

where the parameter a and c are the same as description used for ECAL resolution. Table 3.3 shows the expected energy resolution of HCAL in any regions.

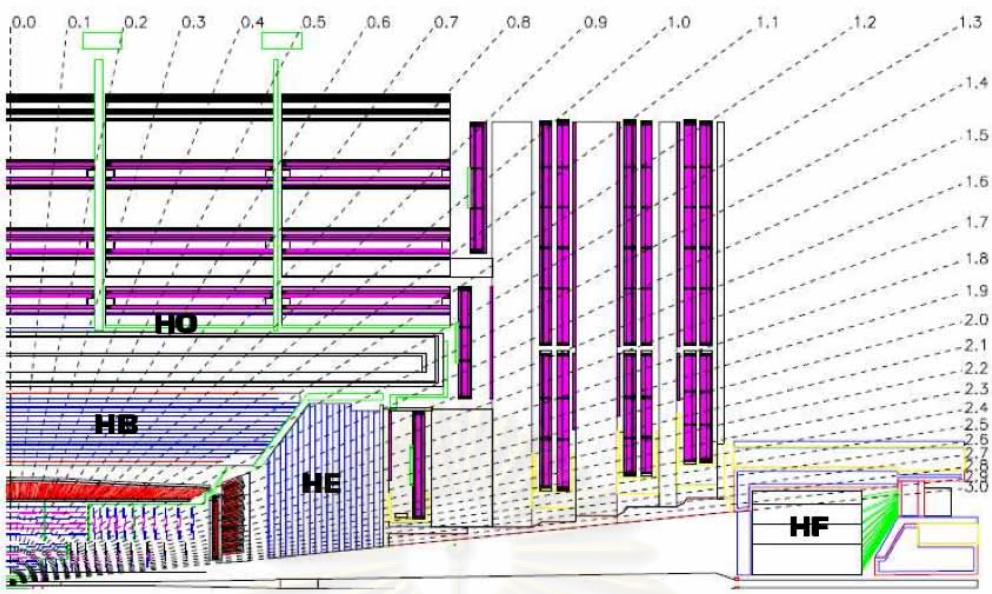

Figure 3.13: The layout of the CMS hadronic calorimeter.

Region	a (GeV$^{1/2}$)	c
Barrel	65%	5%
Endcaps	85%	5%
Very forward	100%	5%

Table 3.3: The expected energy resolutions of the HCAL of the CMS detector.

3.3.4.3 Magnet System

The CMS magnet system, shown in Figure 3.14, consists of a superconducting coil, the magnet yokes, the vacuum tanks, and supporting systems (cryogenics, power supplies, etc). It is the largest superconducting magnet in the world. It will produce a magnetic field of 3.8 Tesla. Equation (3.9) shows the relation between resolution of transverse momentum, magnetic field, and tracker radius.

$$\frac{\Delta P_t}{P_t} \sim \frac{1}{BR^2} \tag{3.9}$$

Following this equation, the resolution can be improved by increasing the radius of tracking system (i.e. a large detector) or by producing a stronger magnetic field. The latter choice has been chosen for CMS. With a strong magnetic field, physicists and engineers designed CMS to be a compact detector.

The central magnet coil will support the tracker and calorimeter systems. For the return yoke, it will support the muon system and have a return magnetic field of 2 Tesla. It will bend muon trajectories in the opposite direction compared to the inner system. The yoke is divided into a barrel and endcaps. The barrel wheels are divided into five wheels, each wheel is composed of three iron layers.

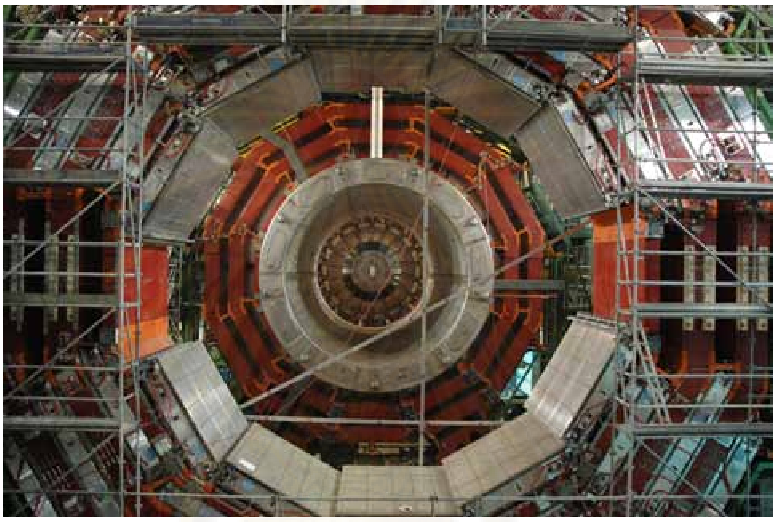

Figure 3.14: The complete CMS magnet coil (central part of picture) and the magnet return yoke (red part around center).

3.3.4.4 Muon System

The muon system is used to identify muons, i.e. to locate their positions, and to measure their momenta. Three different types of detectors were chosen which include: Drift tubes (DTs) and Cathode Strip Chambers (CSCs) are used for the trajectory measurement in the barrel and endcaps region, respectively. The Resistive Plate Chambers (RPCs) are used to provide fast muon information for the Level-1 trigger. The RPC has been installed in both barrel and endcaps regions. The muon system is located inside the magnet return yoke. Figures 3.15 and 3.16 show the layout of muon stations in the longitudinal and transversal views, respectively. The full detail of the CMS muon detector can be found in [18].

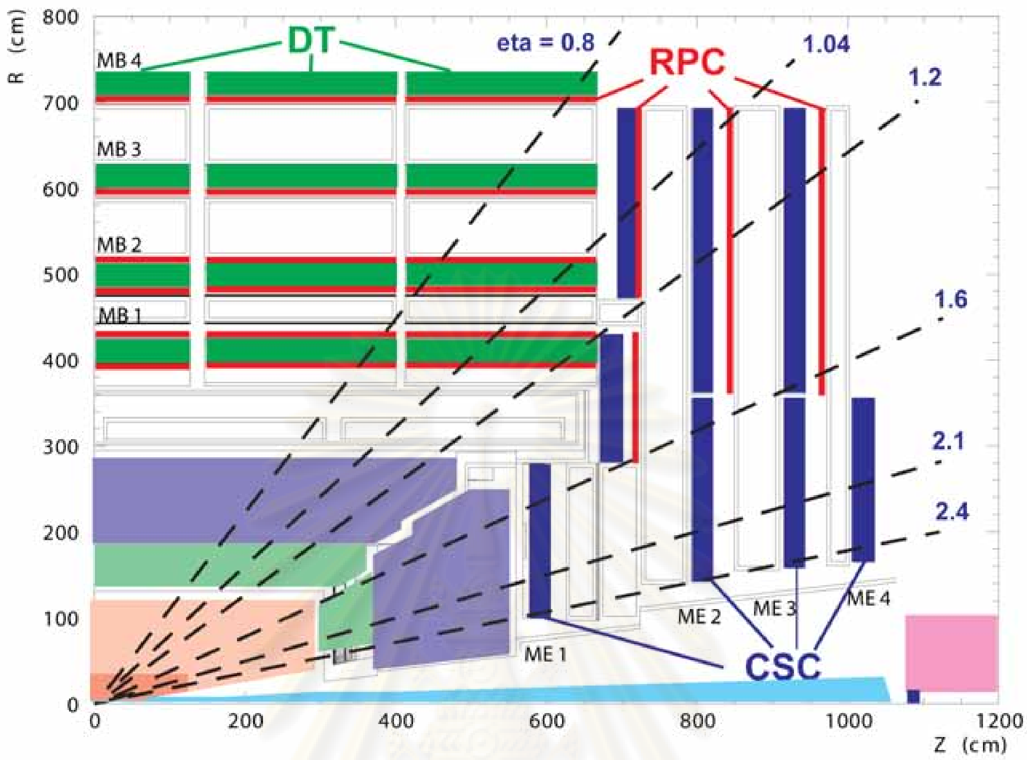

Figure 3.15: Longitudinal view of one quarter of the CMS detector.

The Drift Tube Chambers (DTs)

In the barrel region ($|\eta| < 1.2$), drift tube detectors can be used because of the relatively low particle production rate in the central region and the magnetic field is mainly contained in the iron plates of the magnet return yoke. Figure 3.17 shows the layout of a drift cell.

When an ionizing particle passes through this part, it will liberate electrons which will move along the electric field to the wires. The distance of the ionizing particle track from the wire is calculated by the multiplication of the drift time of electrons (the time it takes for the ionizing electrons to migrate to the wire) and the electron drift velocity in the DTs gas. The DTs gas is composed of 85% of Ar and 15% of CO_2. The drift velocity is about 5.6 cm/μs.

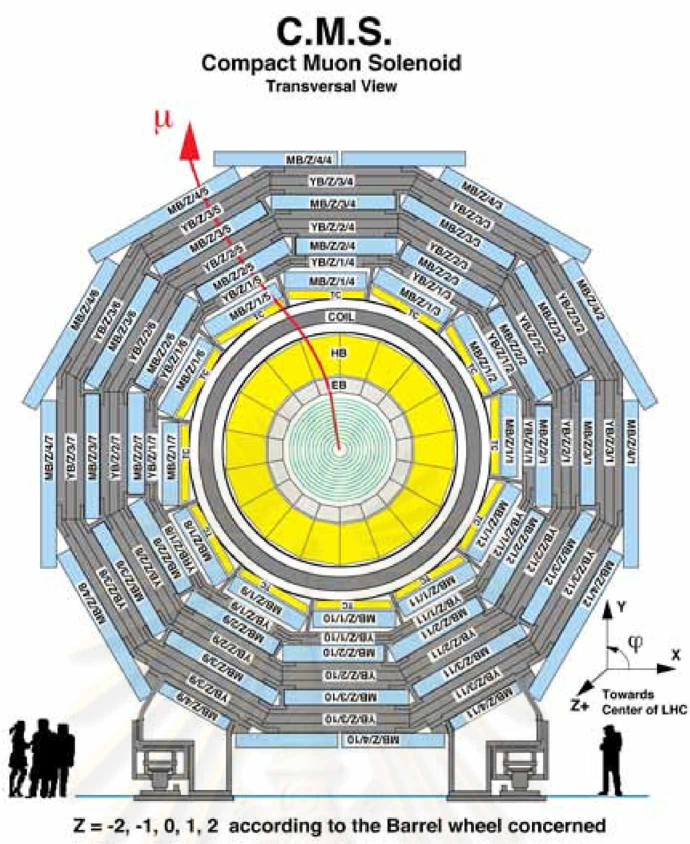

Figure 3.16: Transversal view of the CMS detector. At present, there are some changes in details of geometry.

The muon barrel (MB) system is divided into five wheels along the z-axis or beam line. Each wheel is divided into 12 sectors. The chambers are arranged in four stations (MB1, MB2, MB3, and MB4) as shown in Figure 3.16 , each station consists of 12 DTs, except the MB4 chamber which consists of 14 DTs. In total, there are 250 DTs.

The Cathode Strip Chambers (CSCs)

In the endcaps region ($0.9 < |\eta| < 2.4$), the magnetic field is very intensive and very inhomogeneous. The cathode strip chambers are selected to be the muon tracking detector in this region. CSCs are multi-wire proportional chambers which can give a good spatial and a good time resolution in a large inhomogeneous field [18].

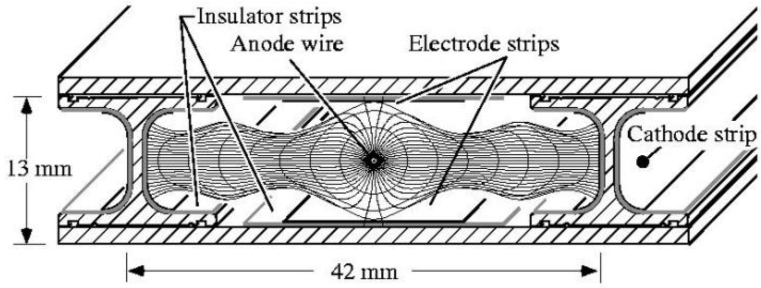

Figure 3.17: A scheme of the drift tube cell.

The cathode strip chambers are divided into four disks placed between the iron disks of the return yoke. These are called ME1, ME2, ME3, and ME4 as shown in Figure 3.15. ME1 consists of three concentric rings. ME2 and ME3 are composed of two rings, while the outermost ME4 is composed of one ring only. In total there are 540 CSCs.

Each chamber is composed of six layers. Each layer consists of an array of anode wires between two cathode planes as shown in Figure 3.18. The gas fills in cathode strip detectors is the mixture of $Ar/CO_2/CF_4$ with ratio 30:50:20.

With the DTs and CSCs, the muon system covers the region $|\eta| < 2.4$.

The Resistive Plate Chambers (RPCs)

The resistive plate chambers have been installed in both barrel and endcap system because they can give an excellent time resolution, of order of few nanoseconds. The information from the 610 RPCs from both barrel and endcap will give us the fast trigger signal to identify muon track.

The structure of the RPC is two parallel phenolic resin (bakelite) plates which have a high bulk resistivity ($10^{10}\,\Omega$cm) [19]. The gap between these two plates is 2 mm, filled with gas which is composed of 97% of freon ($C_2H_2F_4$) and 3% of isobutane.

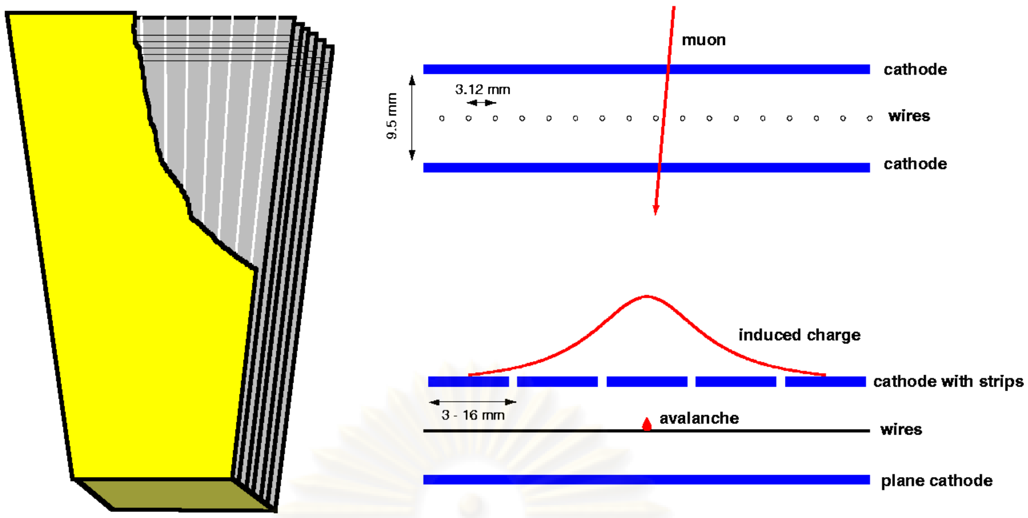

Figure 3.18: (Left) The layout of CSCs layer. A six-plane chamber of a trapezoidal shape with strips along the radial direction and wires lie across. (Right) Orthogonal sections of a CSC layer.

3.3.4.5 The Trigger and Data Acquisition (DAQ)

At the nominal luminosity of the LHC, $10^{34}\text{cm}^{-2}\text{s}^{-1}$, about 20 inelastic proton-proton events occur at the beam crossing rate of 40 MHz. At this level, the input rate is about 10^9 interactions per second. This rate has to be reduced by the factor of 10^7 due to the maximum rate of data archive at CMS is a few 100 Hz. The architecture of the CMS data acquisition system is shown in Figure 3.19. The interaction rate of some selected processes at the proton - (anti)proton collider is shown in Figure 3.20.

The CMS Trigger and Data Acquisition System (TriDAS) is designed to inspect the readout information from each subsystem of the detector at the full crossing frequency and select only the interesting events at the maximum rate of $\sim$ 100 Hz. Two steps of data reduction have been designed for the CMS. For the first step, the Level-1 (L1) system is provided based on customized electronics. This step has been designed to reduce the rate of events to less than 100 kHz. The time to perform the accept-reject decision is very limited due to the bunch crossing at a rate of 40 MHz, and the total time need for decision of the L1 logic system is 3.2 μs. The pipe-line buffer has been designed, to store the data for 128 bunch crossings (3.2 μs/25 ns) before the decision comes. The L1 trigger uses information from calorimeter and muon system. The L1 decision is based on the presence of local objects which include photons, electron, muons and jets.

The second step, the High-Level Trigger (HLT), is designed to reduce the maximum rate of data output from L1 trigger to the final output rate of 100 Hz and to decide which events will be stored for offline analysis. The decision is done by fast reconstruction of the event from ~700 frontends of all sub-system of the detector. This step is provided by software running on the computer farm of commercial processors, so it is highly flexible and depends on the number of CPUs.

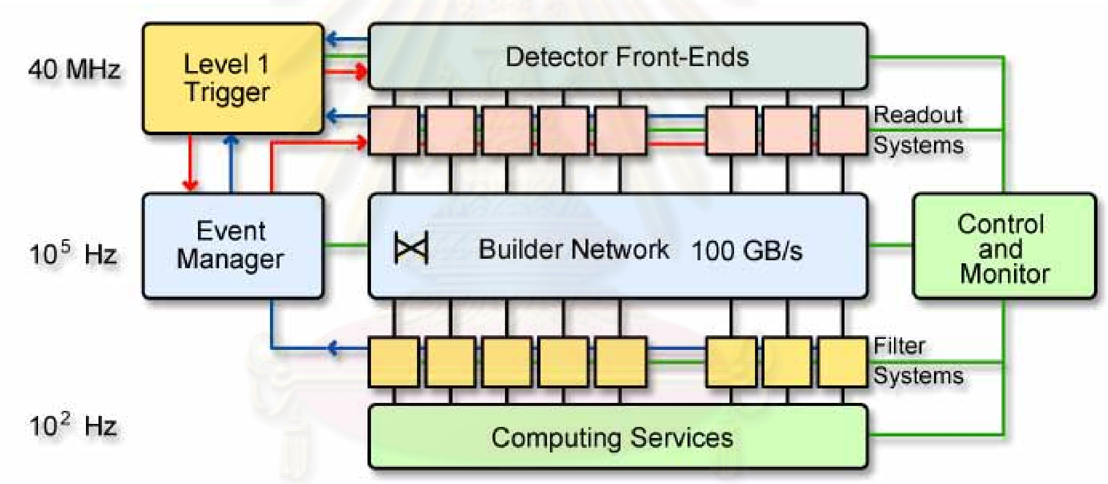

Figure 3.19: The architecture of the CMS DAQ system.

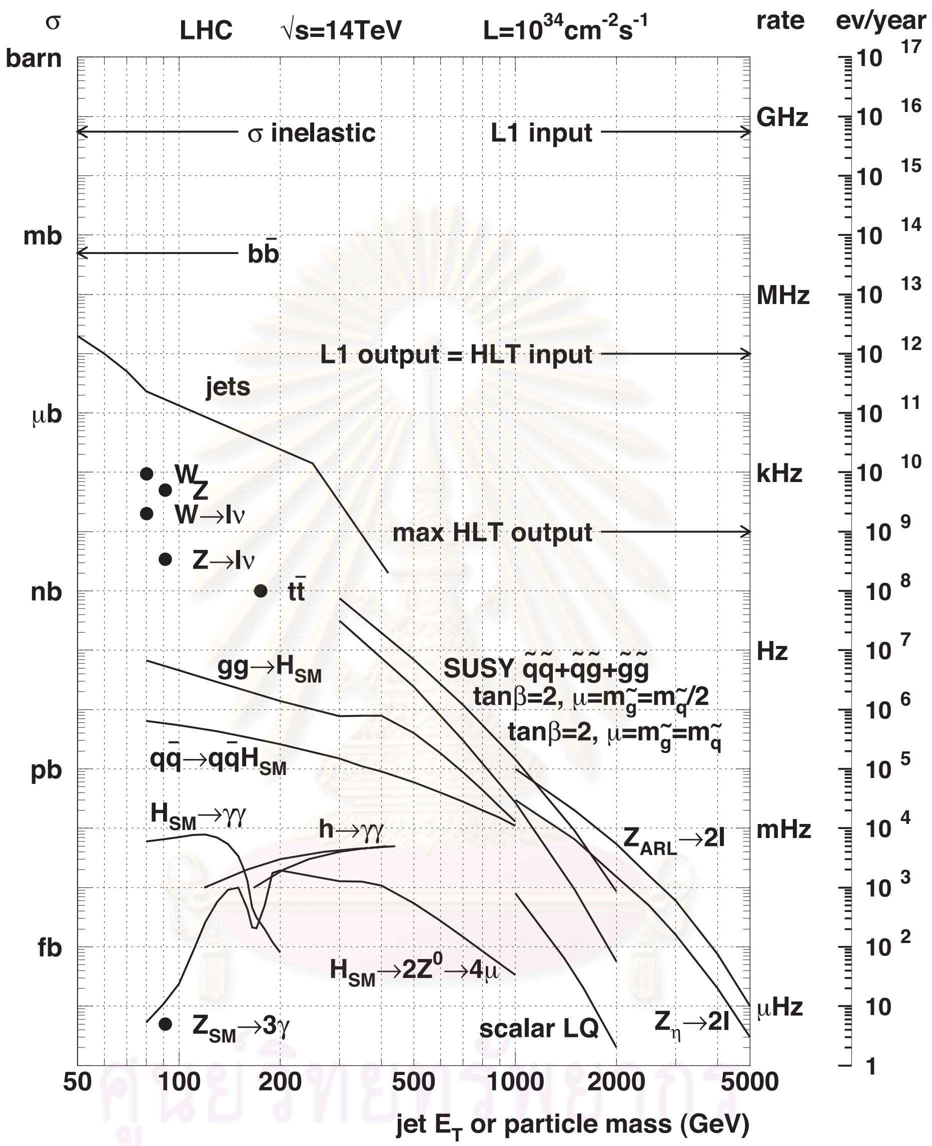

Figure 3.20: The inclusive proton-(anti)proton cross sections for the basic physics process. The right hand scales show the interaction rates at the nominal luminosity of the LHC.

CHAPTER IV

The CMS Computing System

4.1 Introduction

The CMS computing system is one of the most important systems for preparing physicists to analyze data of the LHC. Data from Monte-Carlo simulations are used as samples of events we expect to collect in the real experiment. In 2006, a huge transition from the old full simulation framework, `COBRA`, to the new one, `CMSSW` took place. In this work, the first results came from the fast simulation using `COBRA` framework, called `FAMOS`. The final results came from the `CMSSW` version `2_2_9` and `3_3_4`. The simulation chain is shown in the diagram of Figure 4.1.

In principle, the procedure to study particle physics using computer simulation can be divided into six levels as follows:

1. **Generator level**: In the `COBRA` framework, the Monte-Carlo event generator framework which is used for CMS simulation is `CMKIN`. The `CMKIN` code has an interface to other event generators like `PYTHIA` [20], `HERWIG` [21], or `ISAJET` [22]. The generator produces a list of (quasi)-stable particles with their momenta, vertices, and their relationships with mother and its daughters. In `CMSSW`, most of the standard Monte Carlo generators are modified to work with `CMSSW` directly, i.e. the `Herwig6Interface` package which is used in this thesis.

2. **Simulation of material effects when particles pass through the detector**: This level is the simulation of (quasi)-stable particles that propagate

through subsystems of the detector. This is the most time consuming level. The particles are allowed to decay via their known branching fractions and the kinematics of decayed particles will be calculated. In the COBRA framework, this level is done by OSCAR which is based on GEANT4. The output information from this level are called *SimHits*. *SimHits* is also created in CMSSW.

3. **Simulation of readout electronics (digitization)**: In the real world, when a particle hits a unit of detector, that unit will convert the energy deposited by particle into an electronic signal. Next, the electronic signals are converted to digital information. At the high luminosity of the LHC, a signal will overlap up to 20 minimum bias events. The simulation software will combine a signal event with randomly selected minimum bias events. In the COBRA framework, this level is done by the reconstruction software, ORCA. The output information from this level are called *DIGIs*. In the CMSSW, *DIGIs* comes automatically following *SimHits* in the standard configuration.

4. **Reconstruction**: In this level, *DIGIs* are combined to reconstruct "high-level objects", such as reconstructed hits (RecHits) of particles in tracker, and energy deposited in the calorimeter cells. The high-level objects will be the input for the higher-level algorithms such as electron identification, jet reconstruction, etc. This level is done by ORCA. In the CMSSW, this step is merged into a single framework. The users can reconstruct events and produce particle candidates in a single script running in CMSSW framework.

5. **Analysis**: In this level, sets of cuts are applied to the objects that come from the higher-level algorithms. In the CMSSW framework, the PhysicsTools packages provide the analysis object collections in the meaningful way and such that it can be accessed easily. This topic will be discussed in Section 4.4. In the final step of the analysis chain, the physical quantities, e.g. invariant masses, and asymmetries are calculated in order to study many topics in particle physics, e.g. physics of top quarks, CP-violation, supersymmetry or

extra dimensions. This step can be analyzed on the full framework of CMSSW, or on the framework-lite library with ROOT. The framework-lite concept will be also introduced in Section 4.4.1.

6. **Visualization**: In the COBRA framework, the IGUANA project was created for visualizing the Monte Carlo objects. At present, in the CMSSW, three standalone software, called Fireworks, Frog, and iSpy, have been developed independently on the same concept of IGUANA. Figure 4.2 shows the visualization of a sample of $t\bar{t}$ event using the Fireworks.

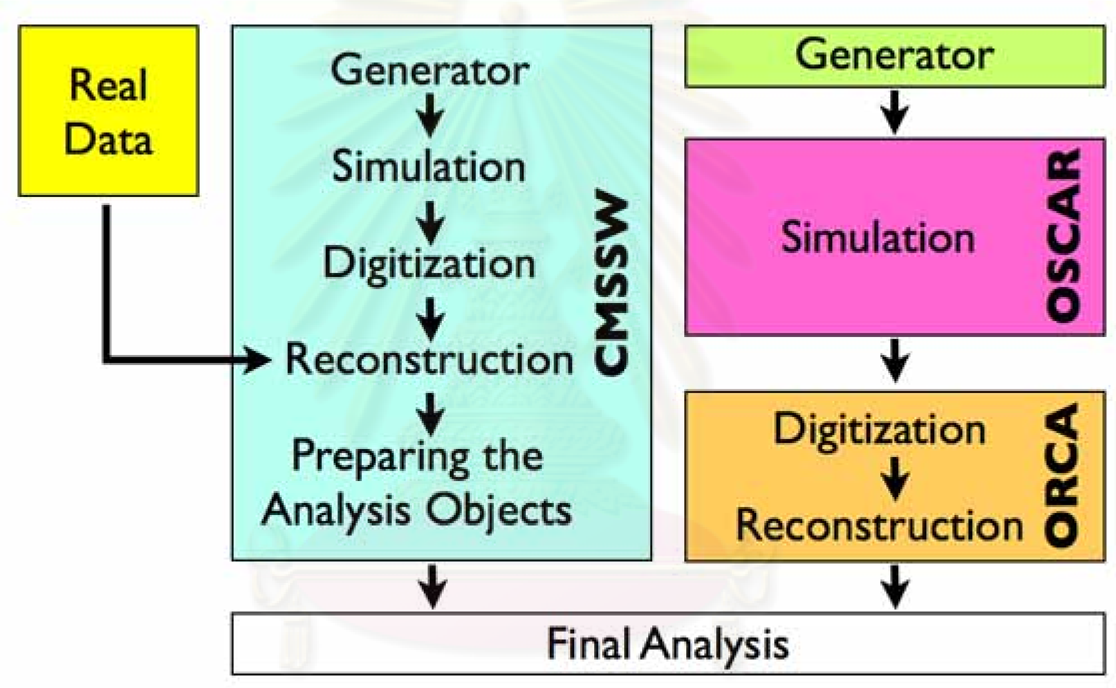

Figure 4.1: Diagram of the simulation chains.

4.2 Monte-Carlo Event Generator

In this work, two generator programs were used in the generator level as follows:

1. ISAWIG

   ISAWIG [23] is software to produce a data file which contains the masses,

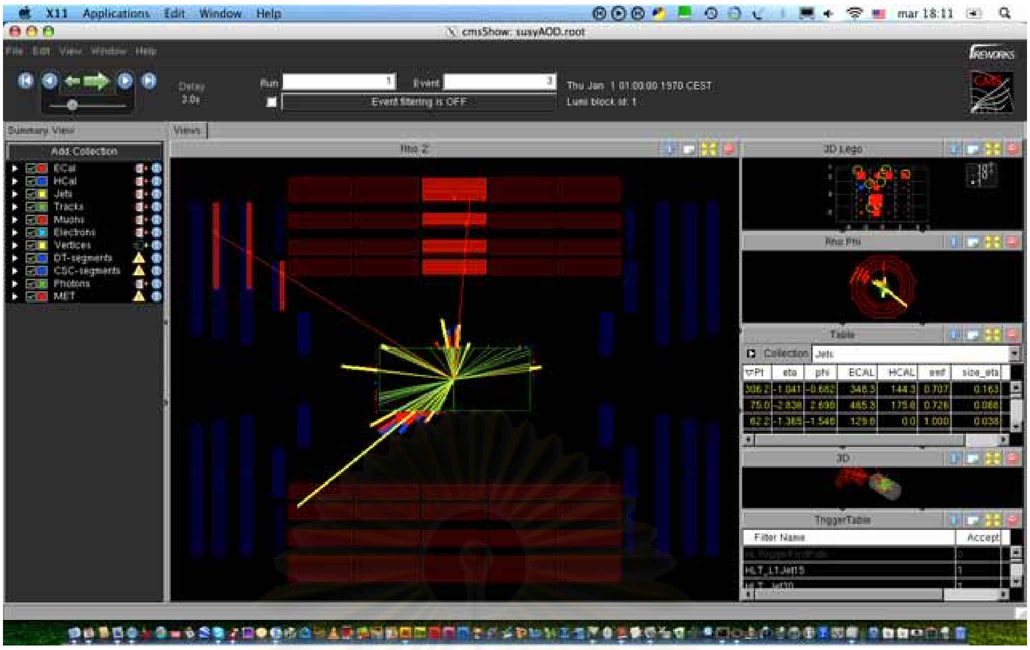

Figure 4.2: The example of visualization from a Monte Carlo $t\bar{t}$ event, using `Fireworks`.

lifetimes and branching ratios of the supersymmetric particles. Inputs for the `ISAWIG` are mSUGRA parameters. The parameters and characteristics of each study point were discussed in Chapter 2.

2. **`CMKIN-ISAWIG` and `Herwig6Interface`**

   The `HERWIG` is chosen to use in this study since it contains the spin correlation algorithm, described in Section 5.4. `CMKIN-ISAWIG` and `Herwig6Interface` are the modified `HERWIG` libraries for working with `COBRA` and `CMSSW`, respectively. They allow to simulate the experimental signatures from collisions. The output contain a list of produced particles, their momenta, original vertices and relationship to their mothers and daugthers. The output from `HERWIG` is then passed to the detector simulation. This step is normally called "generator level" or"parton level".

4.3 Fast Simulating System

Since the full detailed simulation and reconstruction use a lot of CPU time, the fast simulation and reconstruction are proposed to study large samples of the Monte-Carlo events. In the fast simulating system of the `COBRA` framework, simulation and reconstruction are done by object-oriented software called `FAMOS` ([24], [25]). The full details of the `FAMOS` can be found in Chapter 2.6 of [6]. The acronym `FAMOS` stands for Fast MOnte-Carlo Simulation. In the `CMSSW`, these steps are done under `FastSimulation` package. In the beginning, there are five processes which are simulated at the `FAMOS` level.

1. Electron bremsstrahlung.
2. Photon conversion.
3. Ionization by charged particles.
4. Multiple scattering of charged particles.
5. Electron, photon, and hadron showers.

There are many studies which confirm the similarity between results of fast and full simulation in each subdetector. The two examples are given here, as shown in Figures 4.3 and 4.4.

The new `FastSimulation` package covers all fast simulation provided by `FAMOS` with improvements on the simulated process. Examples of the improvements are (1) the simulation of muon propagation and muon hits since `FAMOS` provided only a parametrized muon, (2) implementation of the multiple scattering for muons, (3) improvements in tracking, etc. The detail of the improvements in each CMSSW release can be found on `https://twiki.cern.ch/twiki/bin/view/CMS/SWGuideFastSimTags`. Due to the design of the fast simulation, the output will be written in the same format as the output from the full simulation or real data event, hence the analysis code can be used transparently for all data samples.

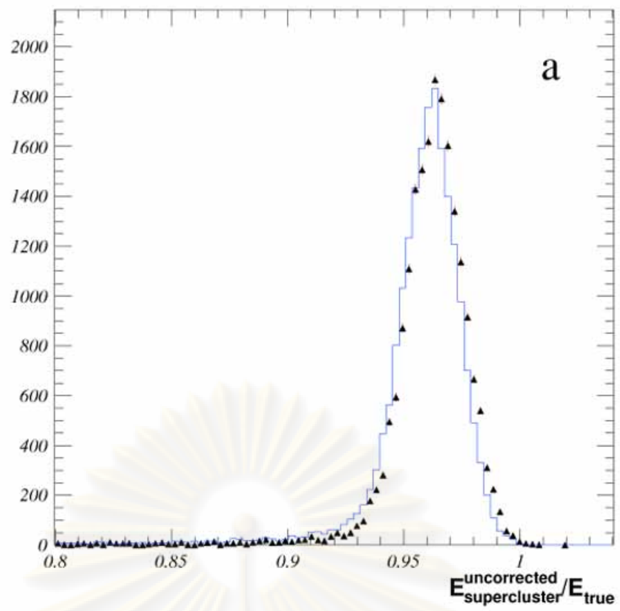

Figure 4.3: Reconstructed supercluster energy over true energy. The triangles with error bars come from fast simulation, while the histogram comes from full simulation.

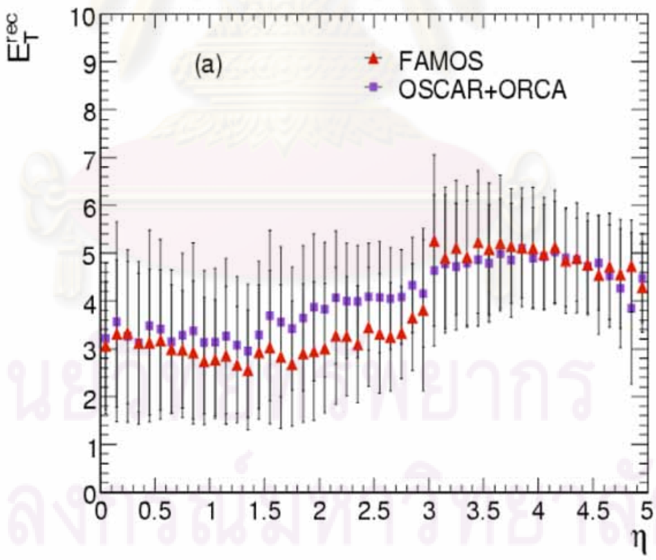

Figure 4.4: Reconstructed transverse energy of pions. The triangles with error bars come from fast simulation, while the squares come from full simulation.

4.4 Physics Analysis Toolkit (PAT)

Physics Analysis Toolkit (PAT) is a part of CMSSW framework which is an interface between the CMS Event Data Model (EDM) and common CMS physics analysis. The CMS EDM is centered around the concept of an Event. An Event is a C++ object container for all raw and reconstructed data related to a particular collision. During processing, data are passed from one module to the next via the Event, and are accessed only through the Event. All objects in the Event may be individually or collectively stored in `ROOT` files, and are thus directly browsable in `ROOT` [26]. Due to a complicated method of calling some quantities from candidates of reconstructed objects, PAT objects are created based on the corresponding reconstructed objects and users can get their quantities of interest by calling member functions of PAT objects. Figure 4.5 shows the main data format of PAT objects which includes pat::Electron, pat::Muon, pat::Tau, pat::Photon, pat::Jet, pat::MET. Figure 4.6 shows the standard workflow of the PAT objects from the reconstruction data. In this thesis, PAT has been used to analyze Monte Carlo data with `CMSSW_3_3_6`.

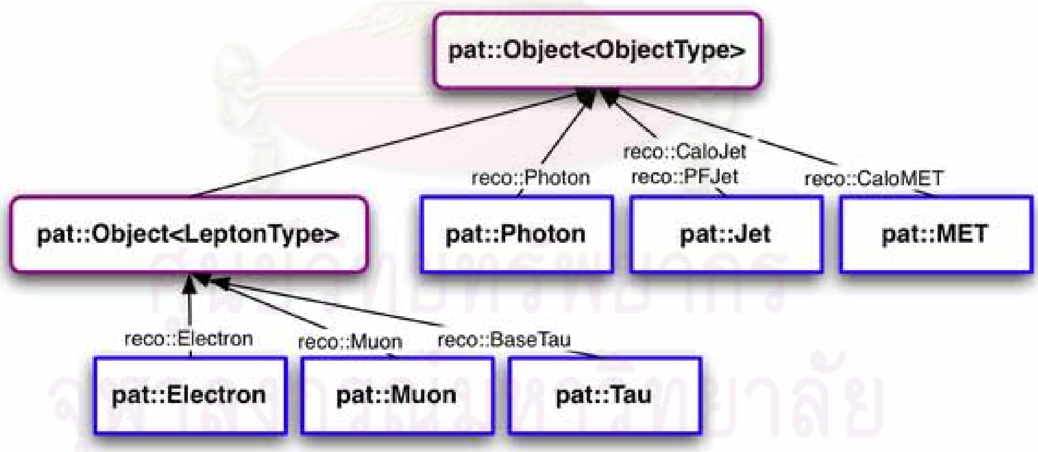

Figure 4.5: The main data format of the PAT objects.

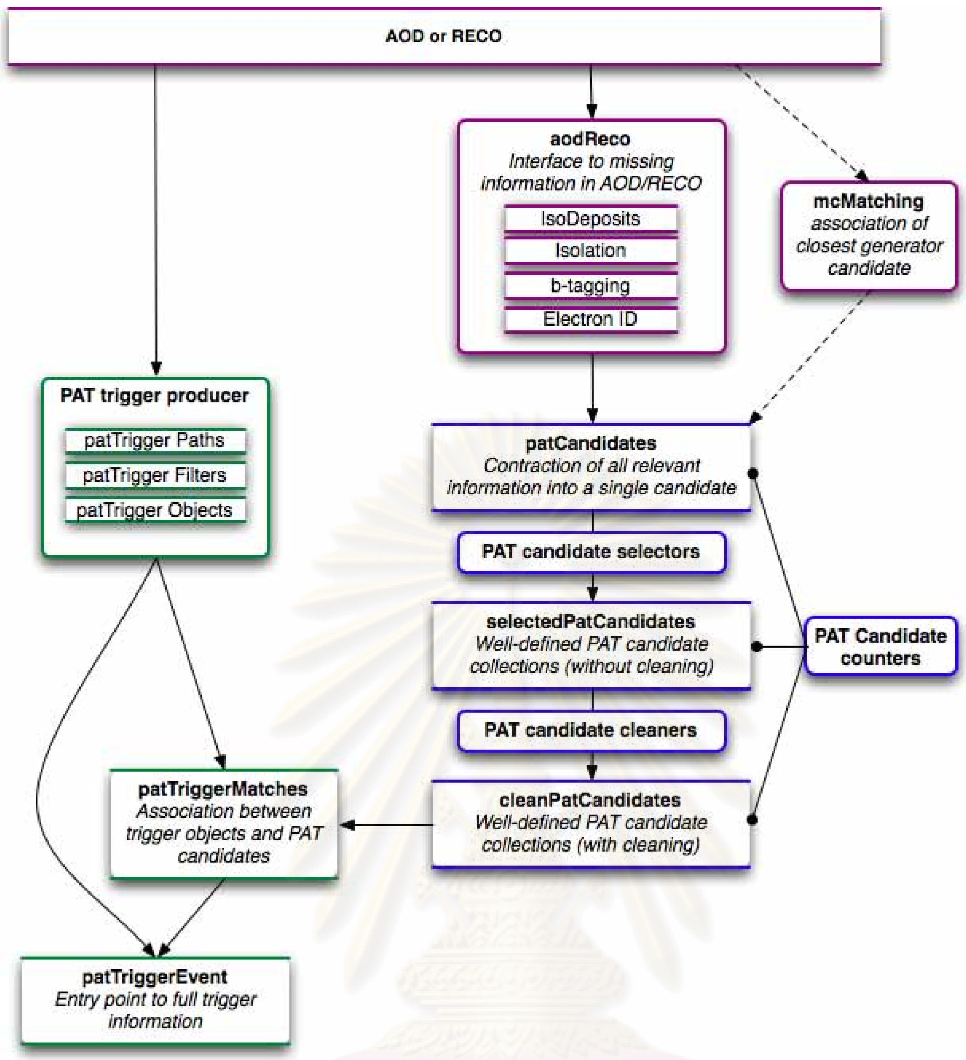

Figure 4.6: The standard workflow of the PAT objects from the reconstruction data.

4.4.1 Analysis in FWLite

Since CMS uses ROOT to store data objects, if the shared libraries of CMS data formats are loaded into ROOT directly, CMS users can analyze CMS data without installing the whole CMS framework on their computers. FWLite (pronounced "framework-light") is the ROOT session with shared libraries of CMS data formats loaded. With FWLite, CMS users do not need to install the CERN Scientific Linux and CMS framework on their own machines, they just install ROOT, which is supported in wide range of operating systems, and download the appropriate

FWLite version. After that, CMS users can analyze the collision or Monte Carlo data on their own machines.

4.5 The CMS Computing Model

Due to a huge amount of data that LHC will produce each year, in a unit of pentabyte (PB), the CMS computing and storage requirements would be difficult to build in one place for both technical and funding reasons. This motivates the creation of the CMS computing environment which can distribute the computing resources and interact with other systems. This is the concept of grid computing. The CMS computing environment includes data processing, data archiving, Monte Carlo simulation, and other kinds of computing-related analysis activities.

The CMS computing model is available around the world by using distribution and configuration in a tiered architecture that functions as a single coherent system. This tier structure was proposed by the Models of Networked Analysis at Regional Centres (MONARC) project. The tier structure includes

1. Tier-0 (T0): This tier is at CERN only and is directly connected to the CMS experiment for the initial processing and data archiving. The first data that come out from CMS online data acquisition and trigger system is called raw data. The T0 does not provide analysis resources, the CMS-CAF (CERN Analysis Facility) is set up to offer services associated with Tier-1 and Tier-2 centers for very fast physics validation and analysis. T0 also performs the first pass reconstruction which will produce a reconstruction data set (RECO) and analysis object data (AOD) files.

2. Tier-1 (T1): The Tier-1 provides substantial CPU power for re-reconstruction, skimming, calibration and AOD extraction. It is also responsible for the second copy of the raw data which is transfered from T0, and for Monte Carlo events generated by the T2 centres.

3. Tier-2 (T2): The Tier-2 provides substantial CPU power for user analysis, calibration studies, and Monte Carlo production. Tier-2 centers provide limited disk space, and no tape archiving, the generated Monte Carlo events are sent to an associated Tier-1 site for distribution among the CMS community.

Figures 4.7 and 4.8 show the charts of the detector data and Monte Carlo data flows through the CMS tiers, respectively. Figure 4.9 shows the tier structure of the CMS collaboration.

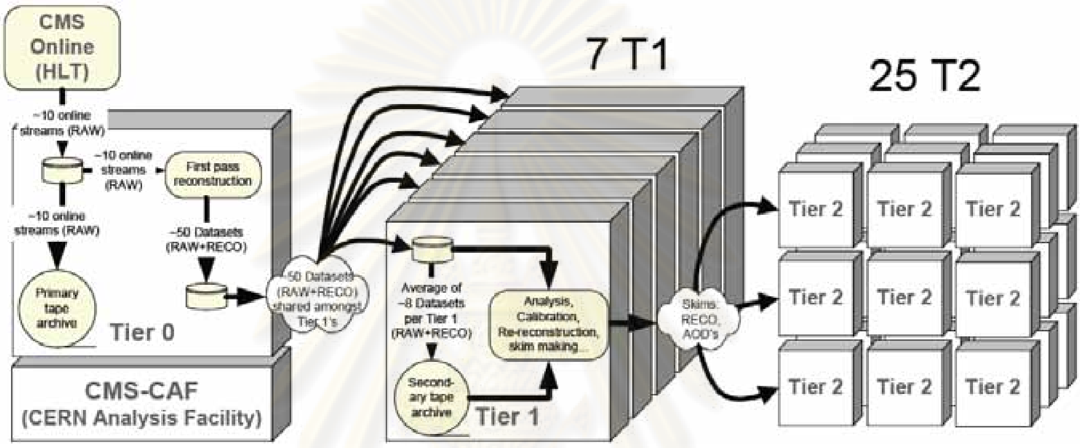

Figure 4.7: Detector data (real data) flow through Hardware Tiers

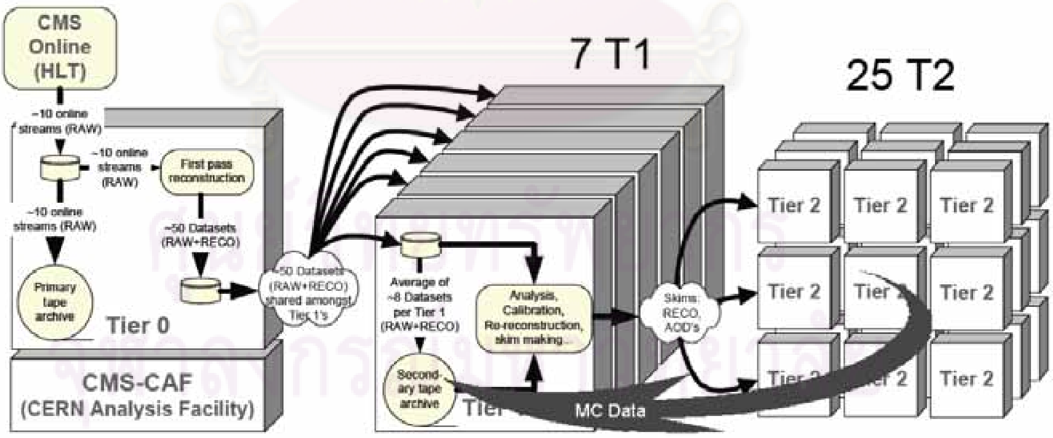

Figure 4.8: Monte Carlo data flow through Hardware Tiers

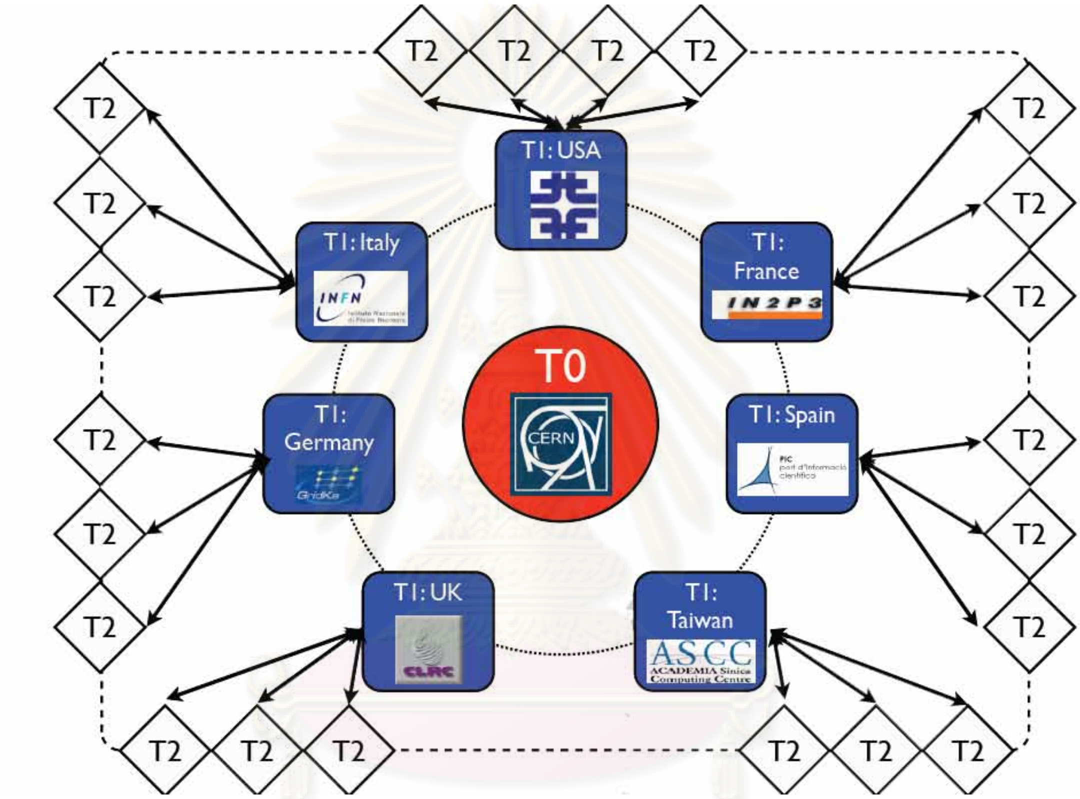

Figure 4.9: The tier structure of the CMS collboration. Note that, this figure does not represent the actual T2 groupings under the T1s.

CHAPTER V

The study of spin correlations in the supersymmetric decay chains

5.1 Introduction

The search for supersymmetric particles is one of the main topics to be studied with the Compact Muon Solenoid (CMS) experiment. To identify supersymmetric particles, first, signals of supersymmetric particles need to be shown up and next the properties of the new particles, such as masses, the production cross section, will be determined. A crucial question, however, will be whether the newly produced superpartners of the Standard Model particles will have the correct spin as predicted by the supersymmetry theory, i.e. spin-0 for the superpartners of the fermions. In this work, variables which are sensitive to the spin of the produced particle will be studied using three minimal Supergravity (mSUGRA) benchmark points, discussed in Chapter 2.

In this section, we study two supersymmetric decay chains of interest, $\tilde{q} \to q\tilde{\chi}_2^0 \to ql^{\pm}_{near}\tilde{l}^{\mp} \to ql^{\pm}_{near}l^{\mp}_{far}\tilde{\chi}_1^0$ and $\tilde{t}^{\pm} \to b^{\mp}\tilde{\chi}_1^{\pm} \to b^{\mp}l^{\pm}\tilde{\nu}_l \to bl^{\pm}\nu_l\tilde{\chi}_1^0$, in three mininal supergravity (mSUGRA) benchmark points, LM1, LM2 and LM6. The first decay chain was studied in ([27], [28], [29]). Using the terminology of [28], the "near" lepton is the lepton from the decay of $\tilde{\chi}_2^0$ and the "far" lepton is the lepton from the decay of slepton ($\tilde{l}$). With the spin correlation, it is shown that the kinematics of final particles, which are composed of two leptons, a quark jet and missing energy, can show a lepton charge asymmetry of invariant masses between

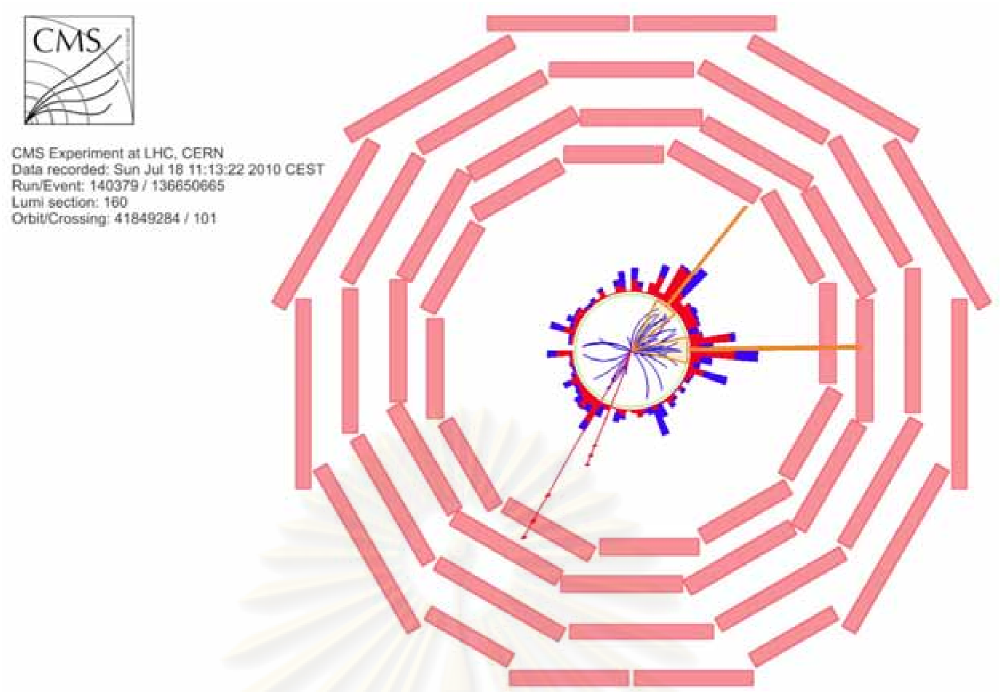

Figure 5.1: A candidate for production of a top quark pair in CMS from data in 2010 [4]. The result shows two muons (red tracks) and two jets (orange cones) tagged as b-jets.

quark-lepton (plus) and quark-lepton (minus). For the second decay chain, the spin correlation affects the characteristics of the invariant mass between b-quark and lepton. For our study, we will go beyond existing studies and we cover all three generations of leptons and quarks since the present experiments, such as CMS and ATLAS, have developed advanced algorithms to identify tau leptons and b-jets among the reconstructed jets. Both of them are important for discovering new physics phenomena, such as Higgs bosons or supersymmetric particles. Figure 5.1 shows a candidate for production of a top quark pair in CMS from data in 2010 [4]. Both top quarks decay to Ws and b-quarks, and both Ws decay to muons and neutrinos (as missing energy). In this thesis, Standard Model processes were also generated and studied as the background of the supersymmetric decay chains of interest.

The parton (generator) distributions, the distributions of interesting quantities of parton objects, and event selection method at the parton level are presented using the CMSSW_3_3_4. We used the benefits of the new framework to generate a huge Monte Carlo data sample, including supersymmetry and Standard Model background, using the HERWIG6 interface module. Since this study started in 2005, when the fast simulation was done by FAMOS_1_6_0, hence the results will be presented from both FAMOS_1_6_0 and CMSSW_3_3_4. One can see the evolution of the event selection method from the previous simulation, to the present simulation and the final algorithms for selecting the decay chains of interest. Table 5.1 shows the cross-section and integrated luminosity of processes of interest.

	Cross-Section (pb)	Integrated luminosity (fb^{-1})		
		FAMOS_1_6_0	CMSSW_2_2_6	CMSSW_3_3_4
LM1	43.28	66.6	60	100
LM2	7.27	-	250	250
LM6	3.84	400.0	500	1000
$t\bar{t}$	421.0	65.0	-	25
WW	69.88	65.8	-	25
WZ	26.84	65.2	-	25
ZZ	11.0	72.7	-	100
DY	7612.0	1.04	-	-
Z+Jets	2.85×10^4	1.04	-	0.25
W+Jets	8.28×10^4	1.08	-	0.1

Table 5.1: The cross-sections and the integrated luminosities of generated events.

5.2 Relevant kinematics

5.2.1 Angles

In experimental particle physics, two important angles, the **azimuthal angle** (ϕ) and the **pseudorapidity** (η) are introduced. The azimuthal angle is the angle which is measured in the transverse plane (XY-plane) while the pseudorapidity describes the particle's direction relative to the beam axis. The pseudorapidity is defined as

$$\eta = -ln \left[\tan \frac{\theta}{2} \right] \tag{5.1}$$

where θ is the angle between the particle momentum and the beam axis. One may write the pseudorapidity in terms of momentum as

$$\eta = \frac{1}{2} ln \left[\frac{|\vec{p}| + p_z}{|\vec{p}| - p_z} \right] \tag{5.2}$$

The name "pseudorapidity" sometimes is confused with "rapidity (y)" which is defined in special relativity. The rapidity is defined as

$$y = \frac{1}{2} ln \left[\frac{E + p_z}{E - p_z} \right] \tag{5.3}$$

The value of rapidity and pseudorapidity will be the same when the particle travels near the speed of light, and the rest mass is very small compared to its momentum. The energy can be approximated as the magnitude of momentum.

Normally in experimental particle physics, we describe the directions of particles with the azimuthal angle and pseudorapidity. To measure the difference of the particle directions in this coordinate, the parameter ΔR or d is defined in the same way as the difference between two points in the Cartesian coordinate system.

$$\Delta R = \sqrt{(\eta_1 - \eta_2)^2 + (\phi_1 - \phi_2)^2} \tag{5.4}$$

The ΔR value will be used in our data analysis to define isolated objects.

5.2.2 Two successive two body decays

First, we calculate the kinematics of two successive two body decays, shown in Figure 5.2. In the rest frame of b, the Feynman diagram can be drawn as shown in Figure 5.3. In this frame, the kinematic freedom is the angle θ between q and p.

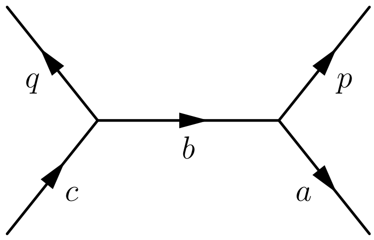

Figure 5.2: Two successive two body decays. Arrows indicate the directions of motion of particles.

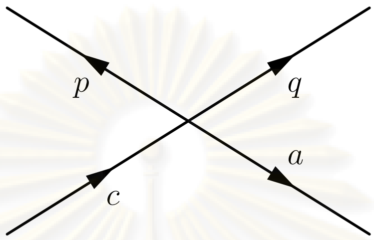

Figure 5.3: Two successive two body decays in the b rest frame.

Consider the decay of particle c to q and b in the b-rest frame, we find

$$(E_c + E_b)^2 - P_c^2 = E_q^2 - P_q^2 \tag{5.5}$$

Applying conservation of momentum, we can evaluate Equation (5.5) as follows,

$$\begin{aligned} E_c^2 + 2E_cE_b + E_b^2 &= E_q^2 \\ E_c^2 + E_b^2 - E_q^2 &= -2E_cE_b \\ E_c^4 + E_b^4 + E_q^4 + 2E_c^2E_b^2 - 2E_c^2E_q^2 - 2E_b^2E_q^2 &= 4E_c^2E_b^2 \end{aligned} \tag{5.6}$$

We then write the energy in terms of momentum and mass, Equation (5.6) can be written as

$$P_c^2 = \frac{m_c^4 + m_b^4 + m_q^4 - 2m_c^2m_b^2 - 2m_c^2m_q^2 - 2m_q^2m_b^2}{4m_b^2} \tag{5.7}$$

$$P_a^2 = \frac{m_a^4 + m_b^4 + m_p^4 - 2m_a^2m_b^2 - 2m_a^2m_p^2 - 2m_p^2m_b^2}{4m_b^2} \tag{5.8}$$

Equation (5.8) can be proven in the same way as Equation (5.7). In the b rest frame, the maximum invariant mass $(m_{pq})_{max}$ can be calculated from

$$(m_{pq})^2_{max} = m_p^2 + m_q^2 + 2(E_pE_q + |P_p||P_q|) \tag{5.9}$$

We can find $|P_p||P_q|$ from Equations (5.7) and (5.8). Finally, we will get

$$(m_{pq})^2_{max} = \frac{(m_c^2 - m_b^2)(m_b^2 - m_a^2)}{m_b^2} \tag{5.10}$$

Equation (5.10) comes with the condition from the order of the decaying particles shown in Figure 5.2. c decays into q and b and then b decays into a and p, so the condition on masses of particles in the decay chain can be written as $m_c > m_b > m_a$.

We can use Equation (5.10) to determine the maximum invariant masses of Standard Model products from the decay chains of interest. For example, we can treat two leptons (plus and minus) as particles p and q, $\tilde{\chi}_2^0$ as c, $\tilde{l}$ as b, and $\tilde{\chi}_1^0$ as a. The maximum invariant mass of dilepton, $m(l^+l^-)_{max}$, can be written as

$$m^2_{max}(l^+l^-) = \frac{(m^2_{\tilde{\chi}_2^0} - m^2_{\tilde{l}})(m^2_{\tilde{l}} - m^2_{\tilde{\chi}_1^0})}{m^2_{\tilde{l}}}. \tag{5.11}$$

5.2.3 Three successive two body decays

The diagram of the three successive two body decays is shown in Figure 5.4. To calculate the maximum invariant mass of $m(pq_1q_2)$, it can be solved using two successive two body decays. We can treat the first two ejected particles as an effective particle with a mass equals to the invariant mass of its constituents. In Figure 5.5, we treat particle q as an effective particle which corresponds to particle q_1 and q_2.

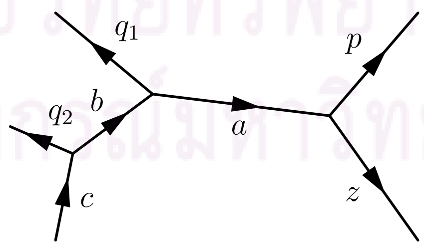

Figure 5.4: Three successive two body decays. Arrows indicate the directions of motion of particles.

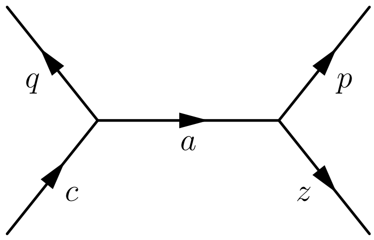

Figure 5.5: Three successive two body decays with an effective particle q.

From Equation (5.10), we can write the invariant mass of particle q as

$$(m_q)^2 = \lambda \frac{(m_c^2 - m_b^2)(m_b^2 - m_a^2)}{m_b^2}, \quad \lambda \in [0,1] \tag{5.12}$$

If we put Equation (5.12) into Equation (5.9), we can find the maximum invariant mass of particles q_1, q_2, and p.

$$(m_{q_1 q_2 p})^2_{max} = m_p^2 + \lambda \frac{(m_c^2 - m_b^2)(m_b^2 - m_a^2)}{m_b^2} + 2(E_p E_q + |P_p||P_q|) \tag{5.13}$$

From the massless condition of the Standard Model particles, a mass of p can be approximated to be zero ($m_p \approx 0$). The energy and momentum of the particles p and q can be calculated from Equations (5.7) and (5.8). Note that, in this case, the calculation is done in the rest frame of a.

$$P_q = \sqrt{\frac{m_q^4 + m_a^4 + m_c^4 - 2(m_q^2 m_a^2 + m_q^2 m_c^2 + m_c^2 m_a^2)}{4m_a^2}} \tag{5.14}$$

$$E_q = \sqrt{m_q^2 + \frac{m_q^4 + m_a^4 + m_c^4 - 2(m_q^2 m_a^2 + m_q^2 m_c^2 + m_c^2 m_a^2)}{4m_a^2}} \tag{5.15}$$

$$P_p = \sqrt{\frac{m_a^4 + m_z^4 - 2m_a^2 m_z^2}{4m_a^2}} \tag{5.16}$$

$$E_p = P_p \tag{5.17}$$

To calculate $(m_{q_1 q_2 p})^2_{max}$, we put Equations (5.14) -(5.17) into Equation (5.13). Consequently, we can arrange the equation as

$$(m_{q_1 q_2 p})^2_{max} = m_q^2 + \frac{(m_a^2 - m_z^2)}{2m_a^2}\left[\sqrt{\{m_q^2 - (m_c^2 + m_a^2)\}^2 - 4m_a^2 m_c^2} + \sqrt{\{m_q^2 - (m_c^2 - m_a^2)\}^2}\right] \tag{5.18}$$

To solve Equation (5.18), we have to maximize it into three cases, when $\lambda = 0$, $\lambda = 1$, and $0 < \lambda < 1$.

For convenience, we use a notation x instead of m_x^2 in our equation, for example, m_c^2 will be written as c.

1. For $\lambda = 0$ (or $q = 0$) the Equation (5.18) becomes

$$
\begin{aligned}
(m_{q_1q_2p})^2_{max} &= \frac{(a-z)}{2a}\left[\sqrt{(c+a)^2-4ac}+\sqrt{(c-a)^2}\right] \\
&= \frac{(c-a)(a-z)}{a} \\
&= \frac{(m_c^2-m_a^2)(m_a^2-m_z^2)}{m_a^2} \qquad (5.19)
\end{aligned}
$$

2. For $0 < \lambda < 1$, We differentiate Equation (5.18) with respect to q, and set the derivative to zero, we find

$$
0 = \begin{cases} 1+\frac{(a+z)}{2a}\left(\frac{1}{2}\frac{(a+c)-q}{\sqrt{\{(a+c)-q\}^2-4ac}}+1\right) & \text{if } q > c-a \\ 1+\frac{(a+z)}{2a}\left(\frac{1}{2}\frac{(a+c)-q}{\sqrt{\{(a+c)-q\}^2-4ac}}-1\right) & \text{if } q < c-a \end{cases} \qquad (5.20)
$$

For the condition $q > c-a$ in Equation (5.20), it is not possible to use this condition since it conflicts with the condition $q \leq \frac{(c-b)(b-a)}{b}$ of Equation (5.10). To prove this, we start from $c-a > (\sqrt{c}-\sqrt{a})^2$ and then determine whether $(\sqrt{c}-\sqrt{a})^2$ is greater than q^2 by assuming that

$$
\begin{aligned}
(\sqrt{c}-\sqrt{a})^2 &> \frac{(c-b)(b-a)}{b} \\
b(c-2\sqrt{c}\sqrt{a}+a) &> cb-ca-b^2+ab \\
(b-\sqrt{c}\sqrt{a})^2 &> 0
\end{aligned}
$$

From the last equation, we can conclude that $c-a > (\sqrt{c}-\sqrt{a})^2 > \frac{(c-b)(b-a)}{b}$, hence the condition $q > c-a$ cannot be used.

For $q < c-a$: We substitute $u = \{(a+c)-q\}$ into Equation (5.20), and rearrange the equation. We get

$$\begin{aligned} 0 &= (a+z) + (a-z)\left\{\frac{u}{\sqrt{u^2-4ac}}\right\} \\ \frac{u^2}{u^2-4ac} &= \frac{(a+z)^2}{(a-z)^2} \\ q &= (a+c) - (a+z)\left(\frac{c}{z}\right)^{1/2} \\ &= \frac{(m_c m_z - m_a^2)(m_c - m_z)}{m_z} \end{aligned} \tag{5.21}$$

One may wonder whether the first differentiation gives a stationary point, maximum point, or minimum point. But in this case, we do not need to calculate the second-order differentiation to check that the stationary point is maximum or minimum point. It was proven from the condition $\lambda > 0$ or $q > 0$, that Equation (5.21) will give a positive value and it is a single value in the region $0 < \lambda < 1$. It cannot be a minimum value in any case. We now would consider the conditions of the result in Equation (5.21).

- For $\lambda > 0$, we can show from the first nominator term that $m_c m_z > m_a^2$.
- For $\lambda < 1$, we compared the Equation (5.21) with q_{max} (Equation 5.12).

$$\begin{aligned} \frac{(m_c^2 - m_b^2)(m_b^2 - m_a^2)}{m_b^2} &> \frac{(m_c m_z - m_a^2)(m_c - m_z)}{m_z} \\ -m_z m_b^4 - m_c^2 m_a^2 m_z &> -m_c m_z^2 m_b^2 - m_a^2 m_c m_b^2 \\ (m_a^2 m_c - m_b^2 m_z)(m_b^2 - m_c m_z) &> 0 \\ \therefore m_a^2 m_c > m_b^2 m_z \quad &\text{and} \quad m_b^2 > m_c m_z \end{aligned} \tag{5.22}$$

Combine the conditions $\lambda > 0$ and $\lambda < 1$, we get $m_b^2 > m_c m_z > m_a^2$ and $m_a^2 m_c > m_b^2 m_z$ are the conditions when $0 < \lambda < 1$. Finally, we substitute Equation (5.21) into (5.18). The maximum invariant mass of q_1, q_2, and p can be written as

$$(m_{q_1 q_2 p})^2_{max} = m_c - m_z. \tag{5.23}$$

3. For $\lambda = 1$, the equation can be written as

$$(m_{q_1 q_2 p})^2_{max} = q + \frac{(a-z)}{2a}\left[\sqrt{(q-c-a)^2 - 4ac} + \sqrt{(q-(c-a))^2}\right]$$

We then substitute $q = \frac{(c-b)(b-a)}{b}$ into the equation, and use the fact that $q < c - a$, the solution can be written as

$$(m_{q_1 q_{2p}})^2_{max} = \frac{1}{2ab}\left[2a(c-b)(b-a) + (a-z)\{|b^2 - ac| + b^2 - 2ab + ac\}\right]$$

If $b^2 > ac$, the solution can be written as

$$(m_{q_1 q_{2p}})^2_{max} = \frac{(b-a)(ca-zb)}{ab}, \tag{5.24}$$

while for $b^2 < ac$, the solution can be written as

$$(m_{q_1 q_{2p}})^2_{max} = \frac{(c-b)(b-z)}{b} \tag{5.25}$$

Finally, we can rewrite the maximum invariant masses $m_{l^+l^-q}$ from Equations (5.19) - (5.25) in the compact form as

$$m^2_{max}(l^+l^-q) = \begin{cases} \frac{(m^2_{\tilde{q}} - m^2_{\tilde{\chi}^0_2})(m^2_{\tilde{\chi}^0_2} - m^2_{\tilde{\chi}^0_1})}{m^2_{\tilde{\chi}^0_2}} & \text{iff } m^2_{\tilde{\chi}^0_2} < m_{\tilde{\chi}^0_1} m_{\tilde{q}}, \\ \frac{(m^2_{\tilde{q}} - m^2_{\tilde{l}})(m^2_{\tilde{l}} - m^2_{\tilde{\chi}^0_1})}{m^2_{\tilde{l}}} & \text{iff } m_{\tilde{\chi}^0_1} m_{\tilde{q}} < m^2_{\tilde{l}}, \\ \frac{(m^2_{\tilde{q}} m^2_{\tilde{l}} - m^2_{\tilde{\chi}^0_2} m^2_{\tilde{\chi}^0_1})(m^2_{\tilde{\chi}^0_2} - m^2_{\tilde{l}})}{m^2_{\tilde{\chi}^0_2} m^2_{\tilde{l}}} & \text{iff } m^2_{\tilde{l}} m_{\tilde{q}} < m_{\tilde{\chi}^0_1} m^2_{\tilde{\chi}^0_2}, \\ (m_{\tilde{q}} - m_{\tilde{\chi}^0_1})^2 & \text{otherwise} \end{cases} \tag{5.26}$$

Note that, "iff" stands for "if and only if".

5.2.4 Hemisphere separation

The idea of hemisphere separation was proposed by F. Moortgat and L. Pape [3]. In summary, if R-parity is conserved, supersymmetric particles are produced in pairs. Hemispheres were defined in order to separate the decay products, i.e. jets, electrons, muons, of the decay chain into two clusters. It helps us reducing the fake rate of pairing the unmatched objects in the event selection. For example, if one wants to measure the lepton+jet invariant mass, the selected lepton(s) and jet(s) should belong to the same hemisphere. In addition, hemisphere separation can also reduce the factor of combinatorial background of Standard Model processes.

In brief, the calculation steps of hemisphere separation are as follows,

1. **Selecting two initial axes:** This step is normally called "Seeding" method. At present, two seeding methods exist. For the first one, the first axis is chosen from the highest momentum object, and the second axis is chosen from the object which has the largest value of $p\Delta R$ with ΔR calculated with respect to the first axis. For the second method, the axes are chosen from the two objects which have the maximum invariant mass or maximum transverse mass.

2. **Pairing the objects to one of these initial axes:** This step is called "Association" method. Three association methods were studied for the physics analysis.

   (a) The scalar product for the momentum of the object and the initial axis is maximized.

   (b) The hemisphere squared massesare minimized. This requires that

   $$m_{ik}^2 + m_j^2 \leq m_{jk}^2 + m_j^2 \tag{5.27}$$

   From the above equation, object with label k is associated with hemisphere i rather than hemisphere j.

   (c) The Lund distance measure is minimized. This requires that

   $$(E_i - p_i \cos\theta_{ik})\frac{E_i}{(E_i + E_k)^2} \leq (E_j - p_j \cos\theta_{jk})\frac{E_j}{(E_j + E_k)^2} \tag{5.28}$$

   As for the previous association method, the object with label k will be associated with hemisphere i rather than hemisphere j.

3. **Redefining the initial axes by summing all momenta of all objects in the same axis:** This step will be done after the completion of previous steps for all objects.

4. **Iterating the pairing again with the new axes:** This step will last until no objects change their axes.

From the studies, it was found that the second seeding method (seeded by the invariant mass) and the Lund distance measure as the association method gives the best efficiency for the hemisphere algorithm. In this thesis, this configuration will be used when we discuss that the hemisphere separation.

5.3 Physics objects

In this section, we will discuss the physics analysis objects which will be used to study the decay chains of interest. In the event selection methods, each selected object will be required to pass the basic requirements defined in this section. The photon will be ignored in our discussion since it is not an object in our decay chains of interest.

5.3.1 Electrons

When electrons emit from the interaction point, they will leave tracks in the inner tracking system and then will deposit their energies in the crystals of ECAL. The ECAL material can cause bremsstrahlung of electrons. It means a single electron can be detected as group of electrons and photons from the bremsstrahlung. Due to the strong magnetic field, electrons in a group inside ECAL will spread as clusters. The "supercluster" algorithm is used to cluster the individual cluster, said otherwise, to reconstruct electron. Details of the supercluster algorithms and energy corrections for the CMS detector can be found in [6]. The requirements for selecting electrons in this thesis are as follows,

1. $|\eta| < 2.5$
2. $P_T > 7$ GeV/c
3. $\frac{P_T}{P_T + \text{Tracker Isolation}} > 0.85$

The "electron tracker isolation" is the summation of the transverse momenta of tracks around the supercluster in a defined cone size, which is 0.35, 0.4 in `FAMOS_1_6_0`, and `CMSSW_3_3_4`, respectively. This summation excludes the electron track candidate. To select electrons, not only the basic kinematic cuts are applied, but also the electron identification methods are included.

5.3.1.1 Electron identification

The electron identification methods are used to select the good quality electrons, it means we can trust that the selected electrons are real electrons from the interactions, and are not fake electrons. Fake electrons come from, i.e. hadron overlaps in jets, prompt electrons from semi-leptonic decays of most c or b quarks, or electrons from early photon conversions in the tracker material. In this thesis, three methods of electron identification, called manual selection, electron likelihood ratio, and robust electron, have been used. The first two methods were used with the analysis results from `FAMOS_1_6_0` and the beginning of the analysis using `CMSSW`, while the last method has been used with the results from `CMSSW_3_3_4` or later. Three electron identification methods are

1. **Manual selection**: An electron is characterized by a reconstructed track and a corresponding narrow cluster in the ECAL. A set of selection variables were defined in order to separate electrons from the background. A set of selection variables, listed in Table 5.2, are

   1.a **The cluster isolation** ($ISO_{cluster}$): This is a ratio of a sum of the momentum of all tracks which lie inside a cone of 0.35 in ΔR around the supercluster axis excluding the electron track candidate divided by a transverse energy of corresponding supercluster.

   1.b **Hadronic energy over electromagnetic energy (HOE)**: Electrons should lose most of their energies in the electromagnetic calorimeter (ECAL), therefore the ratio between the detected energy in the hadronic calorimeter and electromagnetic calorimeter, called "HOE", should be closed to zero.

1.c **Electromagnetic energy over track momentum (EOP)**: The momentum of the matched track should be almost equal to the deposit energy of electron in the electromagnetic calorimeter. The ratio of these quantities should be closed to unity.

1.d **The ratio of the deposited energy of electron in the crystal size 3X3 over in the crystal size 5X5 (E_{3X3}/E_{5X5})**: As described in (b), electron clusters are expected to deposit their energies in electromagnetic calorimeter. They are expected to deposit all energy in the 3X3 crystals array, hence the ratio of the energy deposited between 3X3 arrays and 5x5 arrays should be closed to unity. This measurement is sometimes called the shower shape measurement.

1.e **The shower shape σ along η ($\sigma_{\eta\eta}$)**: Like the concept of the shower shape described above, the energy of an electromagnectic cluster should be extended in 3X3 crystals. Due to the strong magnetic field of the CMS, the electromagnetic cluster will be narrow in the η direction, while it may extend in the ϕ direction. This measurement will measure the differences of pseudorapidity in units of crystal cells.

1.f **The difference of pseudorapidities between the track and supercluster ($\Delta\eta$)**: This will measure the difference in the η direction between matched track and corresponding supercluster of electron candidates.

1.g **The difference of azimuthal angles between the track and supercluster ($\Delta\phi$)**: The same as $\Delta\eta$, but this will measure in the ϕ difference.

Electrons whose their identification variables agree with cuts shown in Table 5.2 are considered to be electron candidates for further analyses.

variable	cut
$ISO_{cluster}$	< 0.2
HOE	< 0.05
EOP	> 0.8
E_{3X3}/E_{5X5}	> 0.9
$\sigma_{\eta\eta}$	< 0.0002
$\|\Delta\eta\|$	< 0.005
$\|\Delta\phi\|$	< 0.02

Table 5.2: The electron isolation variable cuts used in this thesis.

2. **Electron likelihood ratio**: We apply the concept of a likelihood ratio test. The concept is that if we have an electron candidate, we can find the probability that this candidate will be a real or a fake electron. The probability is obtained from the multiplication of the probabilities of the n experimental independent observed variables, as discussed previously in manual selection. The likelihood ratio can be described mathematically as

$$L(\vec{x};\psi) = \prod_{i=1}^{n} P_i(x_i;\psi) \tag{5.29}$$

where $P_i(x_i;\psi)$ is the probability density function for variable i having value x_i, with a given hypothesis ψ. The likelihood ratio used to separate between real and fake electrons is given by,

$$\text{Electron identification (likelihood ratio)} = \frac{L(\vec{x};Elec)}{L(\vec{x};Elec) + L(\vec{x};Jet)} \tag{5.30}$$

The method of this identification was mainly used with the electron collection of `FAMOS_1_6_0`. Figure 5.6 shows examples of electron likelihood distributions for QCD and W+jet events. In this thesis, electrons with the likelihood ratio above 0.65 is treated as electron candidates for analyses.

3. **Robust Tight/Loose electrons**: The robust tight/loose electron identification is the method which contains the basic identifications as described previously in the manual selection. For CMS, robust electron means that

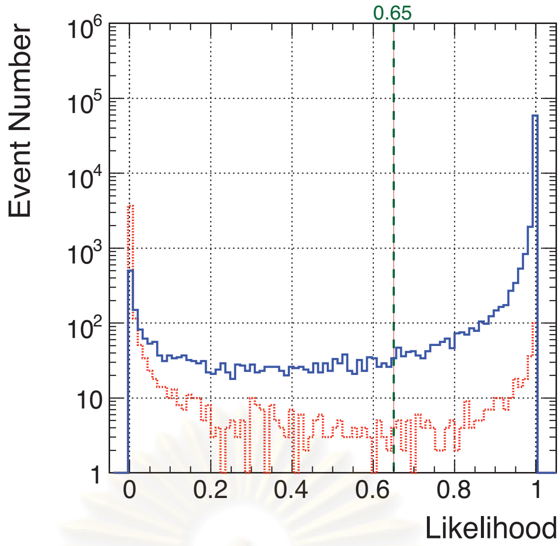

Figure 5.6: The distributions of electron likelihood ratio for QCD events (dotted red curve) and W+jet events (solid blue curve) [5].

the electron identification includes four simple cuts, namely HOE, $\Delta\eta$, $\Delta\phi$, and $\sigma_{\eta\eta}$. The "Tight" and "Loose" in the name refers to the tighter and looser thresholds used for the cuts, respectively. The cut values are shown in Table 5.3. In this thesis, the robust tight electron identification was used with the electron collection of `CMSSW_3_3_4`.

Region	HOE	$\Delta\eta$	$\Delta\phi$	$\sigma_{\eta\eta}$
Robust Tight Electron Cuts				
Barrel region	0.01	0.0099	0.025	0.0040
Endcap	0.01	0.028	0.020	0.0066
Robust Loose Electron Cuts				
Barrel	0.075	0.0132	0.058	0.077
Endcap	0.083	0.027	0.042	0.01

Table 5.3: The selection criteria for robust electron identification.

5.3.2 Muons

The muon reconstruction begins with the local reconstruction from hits in the muon systems, which includes DTs, CSCs, and RPCs. The details of the muon system are given in Section 3.3.4.4. The local reconstruction will collect the hits and form track segments. Then, after matching and combining the track segments, the muon trajectories and transverse momentum will be predicted. These muon candidates are called **standalone muons**. To make precise measurement, the hit information from the silicon tracker will be used. To do this, the muon trajectories from the innermost systems will be extrapolated to the outer part of silicon tracker. Energy losses and multiple scattering are included. The extrapolated tracks will be matched with hits in layers of silicon tracker. From this combination, a better determination of the muon kinematics is made. The muon candidates from this step are called **global muons**. In this study, the requirements for the muons are,

1. Muons are global muons.
2. $|\eta| < 2.1$
3. $P_T > 7$ GeV/c
4. $\frac{P_T}{P_T + \text{Tracker Isolation} + \text{ECAL isolation}} > 0.9$

The meaning of isolation is the same as the one used in the previous section. The tracker and ECAL isolation are just the summation of the transverse momenta and energies of reconstructed charged particle tracks around the muon candidate track in a defined cone size in the tracker and the ECAL, respectively.

5.3.3 Missing transverse energy

The missing transverse energy (MET, $\vec{\not{E}}$) is one of the important quantities used for separating Standard Model background from new physics. In an electron-positron accelerator, the total energy of the collision is the sum of the energy from the electron and positron. In this case, the missing energy mostly comes from undetectable particles, such as neutrinos, which will escape from the detector. However, this concept cannot be used in a hadron collider, such as the LHC. The hadron has an internal structure, hence we cannot determine the energy of the collision because the energy is shared among the components of the hadron. To calculate the missing energy in a hadron collider, we calculate the missing transverse energy instead as the transverse components of colliding particles sum up to zero (particles travel along the $+z$ and $-z$ axes of the detector). The missing transverse energy is calculated using

$$\vec{E}_T^{miss} = -\sum_n \left(\frac{E_n \cos(\varphi_n)}{\cosh(\eta_n)} \hat{x} + \frac{E_n \sin(\varphi_n)}{\cosh(\eta_n)} \hat{y} \right), \tag{5.31}$$

where the sum is for detectable and stable particles at the parton level, or the detected objects for the detector level in the experiment. The φ_n and η_n represent the azimuthal angle and the pseudorapidity of the particles or reconstructed objects, respectively.

To determine the proper selection criteria for the missing transverse energy, its distributions in the supersymmetric processes and the Standard Model background processes are compared. The cut is set at the value which can reject most of the Standard Model background and keep sufficient statistics for analyzing the interesting processes. This value will be discussed in Section 5.4.2.1 for the SUSY decay chain with neutralino-2, and in Section 5.5.1.1 for the SUSY decay chain with chargino-1.

5.3.4 Jets

A jet is one of the most important objects used to search for physics beyond the Standard Model. It is produced from the high transverse momentum quarks and gluons. According to the quark confinement, if we give energy to the quark or gluon to escape from the hadrons, it will create a pair of quark-antiquark, and the process will continue if the remaining energy in the system is enough to create more pairs. This process is called "hadronization". Finally, we will observe a group of mesons and baryons that travel inside a cone which is called a "jet". The mesons and baryons will deposit their energies in the HCAL. The HCAL will measure the energy deposits and shows a hit pattern in (η, ϕ) space. Figure 5.7 shows an example of the tower pattern in the (η, ϕ) space, while the Figure 5.8 shows in the (ρ, ϕ) space of the same event.

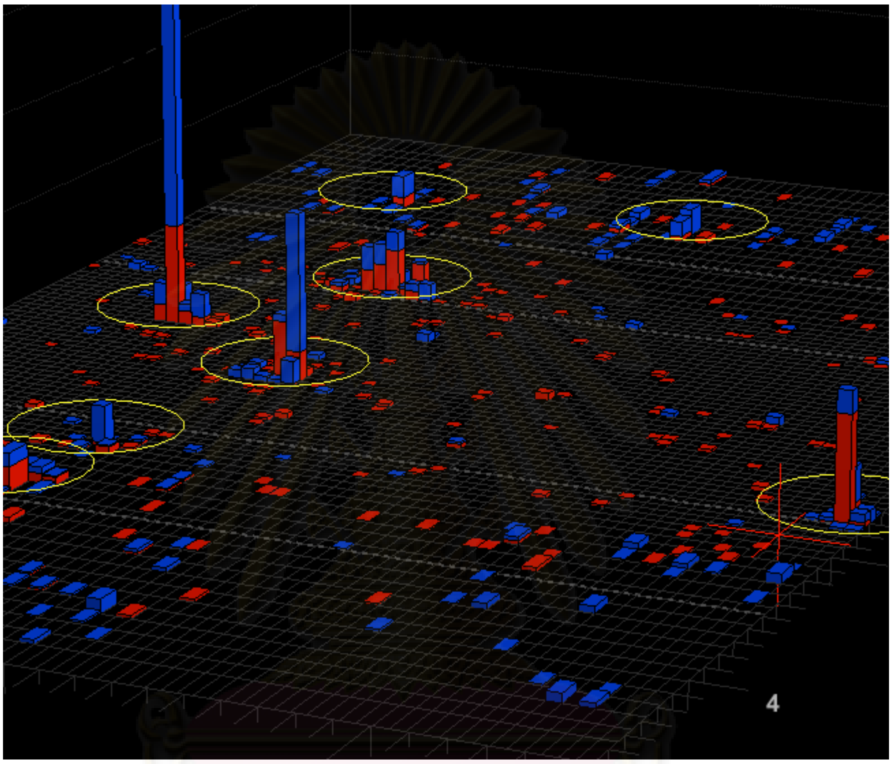

Figure 5.7: The representation of energy deposit in the (η, ϕ) space from a $t\bar{t}$ sample. The blue towers come from the HCAL readout cells, while the red towers come from the ECAL readout cells. The height of towers represents the amount of energy deposited.

The requirements for the jets are as follows,

1. $|\eta| < 5.0$

2. $P_T > 50$ GeV/c

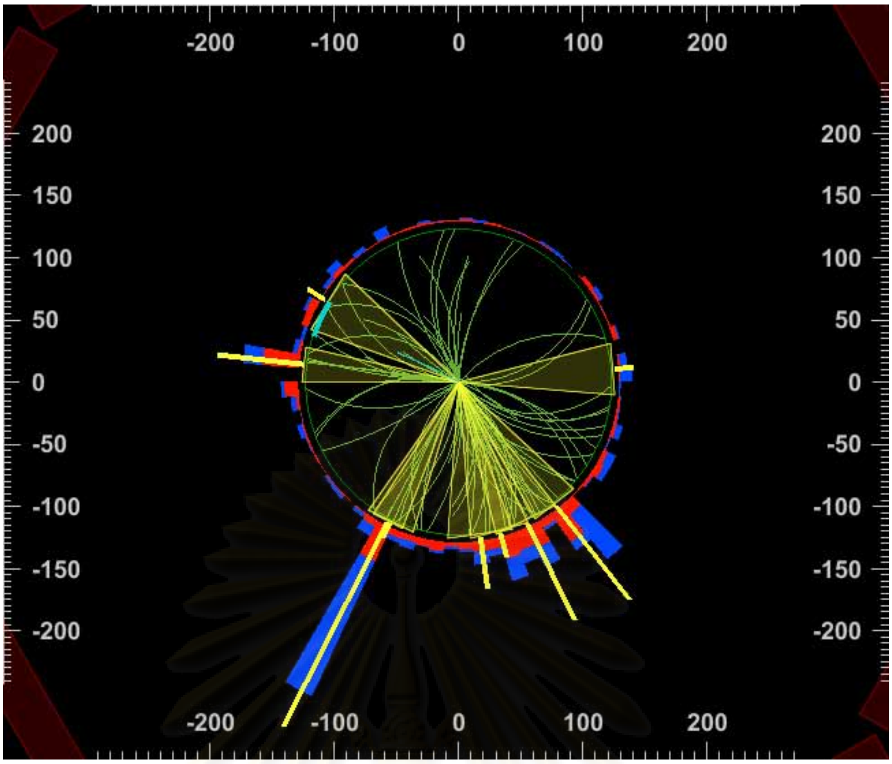

Figure 5.8: The representation of energy deposit in the (ρ, ϕ) space using the same event with Figure 5.7.

Note that, in CMSSW framework, the jet correction is divided into several sub-corrections depending on parts of detector and physics effects. In this thesis, energy of jets are corrected based on the default jet correction of CMS. These corrections are

1. Level 1 - Offset: To reduce effects from pile-up events and electronic noise. Pile-up events are events which are produced as separate events in a single bunch crossing. In the high luminosity accelerator, they are non-negligible effects.

2. Level 2 - Relative: It has been found that the jet response depends on pseudorapidity. This correction is added in order to remove this variation.

3. Level 3 - Absolute: This step aims to correct the observed calorimeter jet energy back to the true jet energy of the stable particles in the jet in the

barrel region ($|\eta| < 1.3$).

The detail of jet corrections can be found in [30].

In this thesis, two algorithms of jet reconstruction which are the "Iterative cone" and the "Inclusive k_T" algorithms are used. These two algorithms will be presented in this section. The input objects in both algorithms are particles or calorimeter towers. One may use the following algorithms to reconstruct parton jets from hadrons in the hadronization step of the event generators. The parton jets is the best reconstructed jet which we can get from parton level data. The iterative cone algorithm is simple and fast, so it is used in the trigger, while the inclusive k_T algorithm is widely used for the offline analysis. The detail of CMS jet algorithms can be found in [6], while the details of the general jet algorithms can be found at [31] and [32].

5.3.4.1 Iterative cone algorithm

In this algorithm, the input objects are ordered by the transverse energy. The cone size R and the energy threshold have to be defined. Starting from the highest E_T object with an energy above a defined threshold, its direction and energy will be used as the primary axis. The calculation loop will look for objects which lay inside the defined cone size, then the direction and the energy of the axis will be recalculated. With the new axis, the process will restart again from the beginning, but using the results from the previous calculation. The process will be repeated until the energy of jet changes by less than 1% and the direction changes by $\Delta R < 0.01$. After the termination, all associated objects will be removed from the input object list, and the jet will be added to the jet list. The procedure will be repeated again to find other jets. The whole process will be finished when the new jet has an energy less than the defined threshold.

5.3.4.2 Inclusive k_T algorithm

For each object i of the input objects, two parameters are calculated as follows,

$$d_i = P_{T,i}^2 \quad (5.32)$$

$$d_{ij} = \min(P_{T,i}^2, P_{T,j}^2)\Delta R_{ij} \quad (5.33)$$

where ΔR_{ij} can be calculated from

$$\Delta R_{ij} = \sqrt{(\eta_i - \eta_j)^2 + (\phi_i - \phi_j)^2} \quad (5.34)$$

If the smallest value between d_i and d_{ij} is d_{ij}, the object i and j will be removed from the input objects, and by merging these two objects, a new object will be added to the input objects. In the case that d_i is smallest, the object i will be removed from the input objects, and it will be added to the list of final jets.

5.3.5 τ-Tagging

The tau is an important physics object for searching for new physics such as Higgs bosons, or supersymmetry. τ-tagging is an algorithm to find tau from jet objects. About 65% of the taus will decay hadronically, and produce jets, we called these jets "hadronic τ jet". Above 70% of hadronic tau decay will give one charged hadron and a number of neutral pions (π^0), this is called "one-prong" decay. In addition, about 10% of hadronic tau jet will go to "three-prong" decay which consists of three charged pions and a number of π^0's. Table 5.4 shows the branching ratios of tau decay. From the τ jet decay product, most of the tau jet will produce a narrow jet in the calorimeter system.

A possible way to identify tau object is to use ECAL isolation, since the τ jet products will deposit their energies in the electromagnetic calorimeter. In CMS, we defined the variable $P_{iso} = \sum_{\Delta R<0.40} E_T - \sum_{\Delta R<0.13} E_T$, where the summation is over all calorimeter cells inside the cone limit with respect to the jet direction. Jets with $P_{iso} < P_{iso}^{cut}$ are tagged as τ candidates. The full details of tau reconstruction and identification in CMS can be found in [33].

$\tau^- \to e^- \bar{\nu}_e \nu_\tau$	17.85%
$\tau^- \to \mu^- \bar{\nu}_\mu \nu_\tau$	17.36%
$\tau^- \to \pi^- \nu_\tau$	10.91%
$\tau^- \to \pi^- \pi^0 \nu_\tau$	25.52%
$\tau^- \to \pi^- 2\pi^0 \nu_\tau$	9.49%
$\tau^- \to \pi^- 3\pi^0 \nu_\tau$	1.00%
$\tau^- \to \pi^- \pi^+ \pi^- \nu_\tau$	8.99%
$\tau^- \to \pi^- \pi^+ \pi^- \pi^0 \nu_\tau$	2.70%
others	6.18%

Table 5.4: τ^- decay branching ratio.

5.3.6 *b*-Tagging

A b-tagging algorithm is an algorithm added on top of the jet reconstruction, to determine whether the jet is a *b*-jet, e.g. from B-hadrons decay. The key point in determining which jet can be tagged as *b*-jet comes from the spatial resolution of charged particle tracks. Figure 5.9 shows a representation of a hadronic jet originating from a B-hadron [34].

In this study, the "Track counting *b*-tagging" algorithm was used to determine the flavor of the jets. In summary, the tracks within a jet are used to compute an impact parameter. The impact parameter is the parameter used to determine whether the track comes from the primary interaction or from the decay of particle which can travel with a significant distance from the vertex. As shown in Figure 5.9, large impact parameter can be found with tracks originating from B-hadron. If the number of tracks which have an impact parameter significance, defined as impact parameter divided by its uncertainty, exceeding a given value is greater than a cut, the jet will be labeled as *b*-jet. A new parameter, called "bDiscriminator", was introduced. In the "track counting *b*-tagging" algorithm, the bDiscriminator was defined as the impact parameter significance of the *n*-th track, where tracks were ordered by decreasing impact parameter significance.

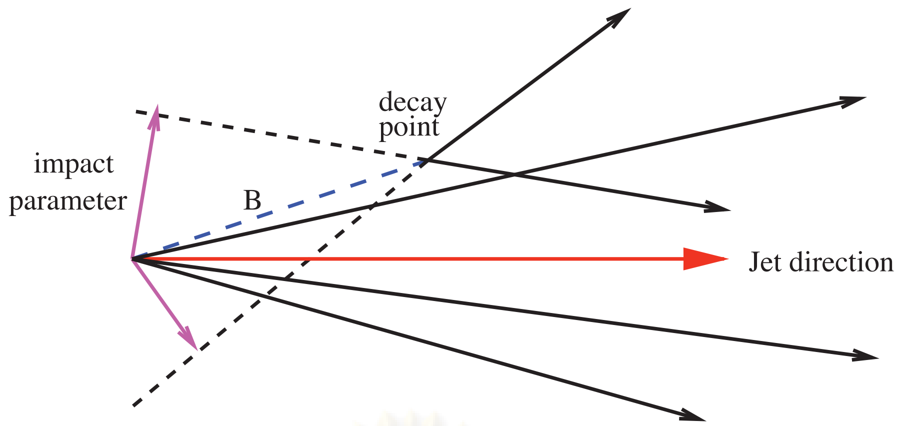

Figure 5.9: Representation of a hadronic jet originating from a B-hadron (not to scale). In this figure, the definition of the impact parameter is shown. It is the parameter used for determination that originals of tracks are at primary vertex or at the secondary vertex which comes from the decay of particle that can travel with asignicant distance from the primary vertex.

Figure 5.10 shows the bDiscriminator distribution calculated from "track counting b-tagging" algorithm of the 2^{nd} track [6]. In this case, if the 2^{nd} track of a jet has the impact parameter significance > 0.53, this jet is tagged as b-jet. In the figure, the fraction ratio of various type of jets is shown as a function of bDiscriminator. For more details on the b-tagging algorithms for the CMS detector, see [34].

In this study, the requirements for selected b-jets are as follows,

1. bDiscriminator ≥ 5.3
2. $|\eta| < 2.4$
3. $P_T > 50$ GeV/c

Note that, the pseudorapidity coverage is less than the jet selection since the b-tagging uses the track information from tracker, and the pseudorapidity coverage of tracker is 2.4, as discussed previously in Section 3.3.4.1.

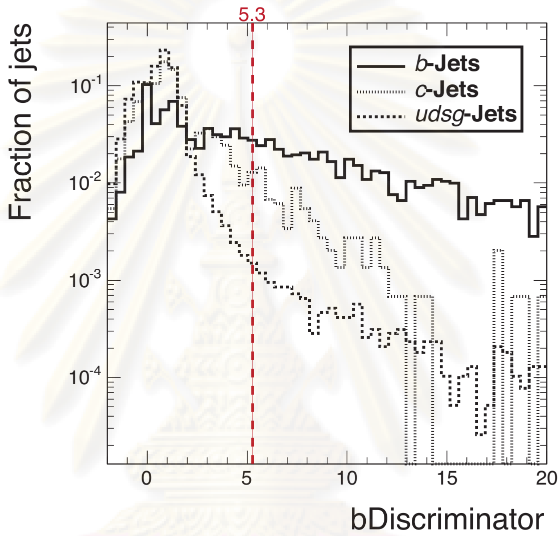

Figure 5.10: The bDiscriminator distribution of the 2^{nd} track for the "track counting *b*-tagging" algorithm. This figure is taken from [6].

5.4 Spin correlations via neutralino-2 decay chain

In this section, we analyze the decay chain, shown in Figure 5.11,

$$\tilde{q}_\beta \to q\tilde{\chi}_i^0 \to q l_{near}^{\pm} \tilde{l}_\alpha^{\mp} \to q l_{near}^{\pm} l_{far}^{\mp} \tilde{\chi}_1^0. \tag{5.35}$$

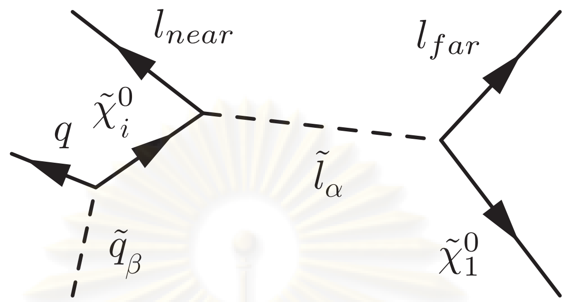

Figure 5.11: The decay chain of interest which decay via neutralino-i. The l_{near} is the lepton from the neutralino-i decay, while the l_{far} lepton comes from the slepton decay.

The suffixes $\beta(=1,2)$, $i(=2,3,4)$, and $\alpha(=1,2)$ are the mass eigenstates of squark, neutralino, and slepton, respectively. Since the branching ratios of the decay chain of interest via $\tilde{\chi}_3^0$ and $\tilde{\chi}_4^0$ are highly suppressed by $\tilde{\chi}_2^0$, so we consider only for $i=2$ in the theoretical distribution. However, contaminations from $\tilde{\chi}_3^0$ and $\tilde{\chi}_4^0$ are also considered in the parton level and detector level analyses.

5.4.1 Theoretical angular distribution

In [28] and [29], the authors proposed probability density function of the decay chain of interest by describing it in terms of three angular variables, $\theta_{\tilde{l}}$, $\theta_{\tilde{\chi}_1^0}$, and $\phi_{\tilde{\chi}_1^0}$. It is given by

$$\begin{aligned}\frac{d^3\Gamma}{dcos\,\theta_{\tilde{l}}\,dcos\,\theta_{\tilde{\chi}_1^0}\,d\phi_{\tilde{\chi}_1^0}} =& \frac{1}{8\pi}\Gamma(\tilde{q}_\beta \to q\tilde{\chi}_2^0)\mathrm{Br}(\tilde{\chi}_2^0 \to l_{near}^{\pm}\tilde{l}_\alpha^{\mp})\mathrm{Br}(\tilde{l}_\alpha^{\mp} \to l_{far}^{\mp}\tilde{\chi}_1^0) \\ & \times \left[1 \pm A(l) cos\,\theta_{\tilde{l}}\right], \end{aligned} \tag{5.36}$$

where $\theta_{\tilde{l}}$ is the angle between momenta of the quark and the l_{near} in the $\tilde{\chi}_2^0$ rest frame, $\theta_{\tilde{\chi}_1^0}$ is the angle between two lepton momenta in the slepton rest frame, and $\phi_{\tilde{\chi}_1^0}$ is the angle between the planes of $\tilde{q}_\beta \to q l^{\pm}_{near} \tilde{l}_\alpha^{\mp}$ and $\tilde{\chi}_2^0 \to l^{\pm}_{near} l^{\mp}_{far} \tilde{\chi}_1^0$. The asymmetry term $A(l)$ is written as

$$A(l) = \frac{|L^q_{2\beta}|^2 - |R^q_{2\beta}|^2}{|L^q_{2\beta}|^2 + |R^q_{2\beta}|^2} \cdot \frac{|L^l_{2\alpha}|^2 - |R^l_{2\alpha}|^2}{|L^l_{2\alpha}|^2 + |R^l_{2\alpha}|^2}, \tag{5.37}$$

where the definition of both the quark and charged lepton sectors, $L^q_{2\beta}$, $R^q_{2\beta}$, $L^l_{2\alpha}$, $R^l_{2\alpha}$, are described in [29]. The factor "2" in both quark and charged lepton sectors is the suffix of the mass eigenstate of $\tilde{\chi}_2^0$. Note that, the left-right mixing of squarks ($\tilde{q}_\beta$) will be ignored in this study because of the dominant decay of the $\tilde{q}_L$ to $\tilde{\chi}_2^0$. The first fraction of Equation (5.37) can be approximated to be unity. For the charge lepton sectors, they can be written as [29]

$$L^l_{21} = -[(U^*_N)_{22} + (U^*_N)_{21} \tan\theta_W] \cos\theta_l + \frac{m_l}{m_W \cos\beta}(U^*_N)_{23} \sin\theta_l, \tag{5.38}$$

$$L^l_{22} = +[(U^*_N)_{22} + (U^*_N)_{21} \tan\theta_W] \sin\theta_l + \frac{m_l}{m_W \cos\beta}(U^*_N)_{23} \cos\theta_l, \tag{5.39}$$

$$R^l_{21} = 2(U_N)_{21} \tan\theta_W \sin\theta_l + \frac{m_l}{m_W \cos\beta}(U_N)_{23} \cos\theta_l, \tag{5.40}$$

$$R^l_{22} = 2(U_N)_{21} \tan\theta_W \cos\theta_l - \frac{m_l}{m_W \cos\beta}(U_N)_{23} \sin\theta_l, \tag{5.41}$$

where θ_W is the Weinberg angle or weak mixing angle and θ_l is the slepton mixing angle, defined by

$$\begin{pmatrix} \tilde{l}_1 \\ \tilde{l}_2 \end{pmatrix} = \begin{pmatrix} \cos\theta_l & \sin\theta_l \\ -\sin\theta_l & \cos\theta_l \end{pmatrix} \begin{pmatrix} \tilde{l}_L \\ \tilde{l}_R \end{pmatrix}. \tag{5.42}$$

The slepton mixing angle can be calculated by diagonalizing the slepton mass matrix which is

$$M^2_{\tilde{l}} = \begin{pmatrix} m^2_{\tilde{l}_L} + m^2_l + m^2_Z \cos 2\beta(\sin^2\theta_W - \frac{1}{2}) & -m_l(A^*_l + \mu\tan\beta) \\ -m_l(A_l + \mu^*\tan\beta) & m^2_{\tilde{l}_R} + m^2_l - m^2_Z \cos 2\beta \sin^2\theta_W \end{pmatrix}. \tag{5.43}$$

Values of θ_l for each lepton in each study point are shown in Table 5.5. One can see that the slepton mixing angle of e and μ are in order of $O(10^{-4})$ and $O(10^{-2})$, respectively. Consequently, the $\tilde{l}_1$ is $\tilde{l}_R$-like, while $\tilde{l}_2$ is $\tilde{l}_L$-like. The slepton mixing angle will become significant when stau is considered. U_N is a unitary matrix calculated from $U^* M_{\tilde{\chi}_0} U^\dagger =$ diagonal (see Appendix C).

Model	Particle	$\cos\theta_l$	$\lvert L^l_{21}\rvert$	$\lvert R^l_{21}\rvert$	$\lvert L^l_{22}\rvert$	$\lvert R^l_{22}\rvert$
LM1	e	7.632×10^{-5}	9.700×10^{-5}	0.117	0.952	3.315×10^{-5}
	μ	0.015	0.019	0.117	0.952	0.007
	τ	0.268	0.337	0.090	0.895	0.113
LM2	τ	0.429	0.618	0.045	0.779	0.227
LM6	e	4.633×10^{-5}	6.298×10^{-5}	0.052	0.976	1.921×10^{-5}
	μ	9.696×10^{-3}	0.012	0.052	0.975	0.004
	τ	0.176	0.229	0.041	0.949	0.066

Table 5.5: The slepton mixing angles and charged lepton sectors

5.4.1.1 The $m(l_{near}q)$ distributions

To study the spin correlation effect, we start by considering the decay of interest according to phase-space (spin correlations are not included in the calculation). The invariant mass of quark and lepton-near can be calculated from

$$(m_{lq})^2 = (m_l)^2 + (m_q)^2 + 2(E_l E_q - |p_l||p_q|\cos\theta_{\tilde{l}}). \tag{5.44}$$

Since considered particles are high energy particles, one can ignore their rest masses. The total energy can be approximated by a magnitude of momentum. With this approximation, Equation (5.44) can be rewritten as

$$(m_{lq})^2 = (m_{lq})^2_{max}\sin^2(\theta_{\tilde{l}}/2), \tag{5.45}$$

where $(m_{lq})^2_{max} = 2|p_l||p_q|$. The maximum invariant mass can be obtained when the lepton and quark are back-to-back of each other ($\theta_{\tilde{l}} = \pi$) in the $\tilde{\chi}^0_2$ rest frame. The ratio of invariant mass and maximum invariant mass has been define as [28]

$$x = (m_{lq})/(m_{lq})_{max}. \tag{5.46}$$

This ratio is sometimes called rescale parameter. The probability density function of the phase-space decay can be written as

$$\frac{d\Gamma_{PS}}{dx} = 2x = 2\sin(\theta_{\tilde{l}}/2). \tag{5.47}$$

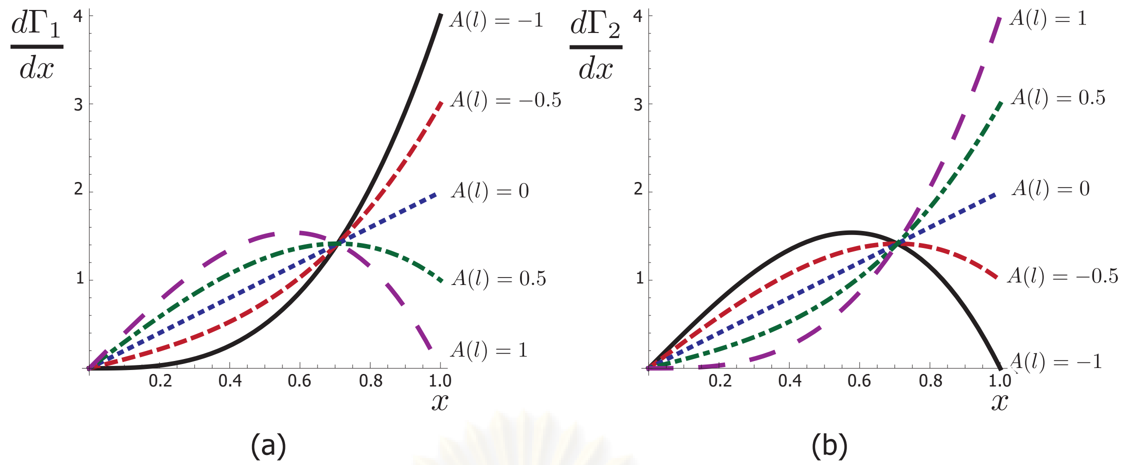

Figure 5.12: The calculated $m(ql_{near})$ distributions in terms of rescale invariant mass x defined in Equation (5.46). The spin projection factor $A(l)$ is varied in the range of [-1,1]. (a) $d\Gamma_1/dx$, and (b) $d\Gamma_2/dx$.

Equation (5.47) can be compared with the result from the integration of Equation (5.36) with respect to $\cos(\theta_{\tilde{\chi}_1^0})$ and $\phi_{\tilde{\chi}_1^0}$. The spin correlation factor comes from the extra factor $[1 \pm A(l) \cos\theta_{\tilde{l}}]$. The probability density function of $m(l_{near}q)$ of the same sign lepton and quark, $m(l^+_{near}q)$ and $m(l^-_{near}\bar{q})$ can be written as

$$\frac{d\Gamma_1}{dx} = 2(1 + A(l))x - 4A(l)x^3, \tag{5.48}$$

and for the opposite sign lepton and quark, $m(l^-_{near}q)$ and $m(l^+_{near}\bar{q})$, the probability density function can be written as

$$\frac{d\Gamma_2}{dx} = 2(1 - A(l))x + 4A(l)x^3. \tag{5.49}$$

Figure 5.12 shows the calculated distributions from Equations (5.48) and (5.49).

If $A(l) \approx -1$ for the electron and muon, the probability density functions of Equations (5.48) and (5.49) can be rewritten as

$$\frac{d\Gamma_1}{dx} = 4x^3 \qquad \text{for} \quad l^+_{near}q, l^-_{near}\bar{q} \tag{5.50}$$

$$\frac{d\Gamma_2}{dx} = 4x(1 - x^2) \qquad \text{for} \quad l^-_{near}q, l^+_{near}\bar{q} \tag{5.51}$$

This case was first studied in [28].

To calculate the maximum invariant mass of $m(l_{near}q)$, it can also be calculated from Equation (5.10) as

$$m^2_{max}(l_{near}q) = \frac{(m^2_{\tilde{q}} - m^2_{\tilde{\chi}^0_2})(m^2_{\tilde{\chi}^0_2} - m^2_{\tilde{l}})}{m^2_{\tilde{\chi}^0_2}}. \quad (5.52)$$

5.4.1.2 The $m(l_{far}q)$ distributions

The $m(l_{far}q)$ distributions depend on three angles, $\theta_{\tilde{l}}$, $\theta_{\tilde{\chi}^0_1}$, and $\phi_{\tilde{\chi}^0_1}$. They can be described by [29]

$$\begin{aligned} m^2(l_{far}q) &= \frac{1}{4}\frac{(m^2_{\tilde{q}} - m^2_{\tilde{\chi}^0_2})(m^2_{\tilde{l}} - m^2_{\tilde{\chi}^0_1})}{m^2_{\tilde{\chi}^0_2}m^2_{\tilde{l}}} \\ &\times[m^2_{\tilde{\chi}^0_2}(1+\cos\theta_{\tilde{l}})(1-\cos\theta_{\tilde{\chi}^0_1}) \\ &+m^2_{\tilde{l}}(1-\cos\theta_{\tilde{l}})(1+\cos\theta_{\tilde{\chi}^0_1}) \\ &+2m_{\tilde{\chi}^0_2}m_{\tilde{l}}\sin\theta_{\tilde{l}}\sin\theta_{\tilde{\chi}^0_1}\cos\phi_{\tilde{\chi}^0_1}]. \end{aligned} \quad (5.53)$$

The probability density functions depend on the helicity of the far-lepton and the quark [35, 36, 37]. For the same sign far-lepton and quark, $m(l^+_{far}q)$ and $m(l^-_{far}\bar{q})$, the probability density function can be written as

$$\frac{d\Gamma_3}{dx_f} = \frac{-4x_f}{(1-y)^2}\begin{cases} (1-y+\log y) & 0 \le x_f \le \sqrt{y} \\ (1-x_f^2+\log x_f^2) & \sqrt{y} < x_f \le 1 \end{cases} \quad (5.54)$$

and for the opposite sign far-lepton and quark, m$(l^-_{far}q)$ and m$(l^+_{far}\bar{q})$, it can be written as

$$\frac{d\Gamma_4}{dx_f} = \frac{4x_f}{(1-y)^2}\begin{cases} (1-y+y\log y) & 0 \le x_f \le \sqrt{y} \\ (1-x_f^2+y\log x_f^2) & \sqrt{y} < x_f \le 1 \end{cases} \quad (5.55)$$

where $y = m^2_{\tilde{l}}/m^2_{\tilde{\chi}^0_2}$ and x_f is rescale parameter defined by

$$\begin{aligned} x_f &\equiv m^{far}_{lq}/(m^{far}_{lq})_{max} \\ &= \frac{1}{2}[(1+y)(1-\cos\theta_{\tilde{l}}\cos\theta_{\tilde{\chi}^0_1}) + (1-y)(\cos\theta_{\tilde{l}} - \cos\theta_{\tilde{\chi}^0_1}) \\ &-2\sqrt{y}\sin\theta_{\tilde{l}}\sin\theta_{\tilde{\chi}^0_1}\cos\phi_{\tilde{\chi}^0_1}]^{1/2}. \end{aligned} \quad (5.56)$$

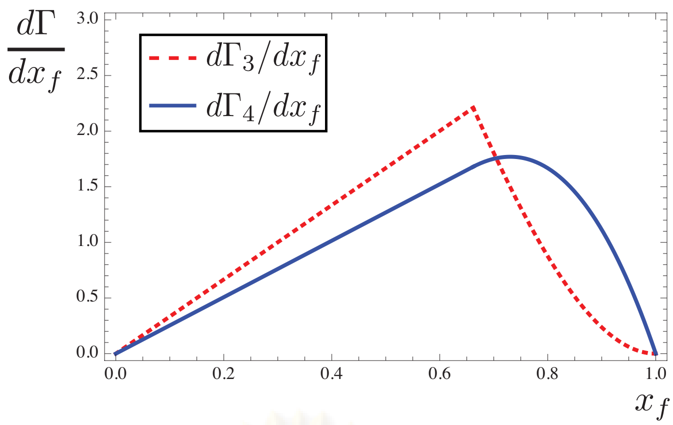

Figure 5.13: The $m(ql_{far})$ distributions in terms of rescale invariant mass x_f defined in Equation (5.56). The factor y is calculated with $m_{\tilde{l}} = m_{\tilde{e}_R} = 118.88$ GeV/c^2 and $m_{\tilde{\chi}_2^0} = 179.596$ GeV/c^2.

The probability density functions in Equations (5.54) and (5.55) are written when we assume that the far-lepton is left-handed. For the right-handed far-lepton, the probability density functions need to be swapped. Figure 5.13 shows the $m(l_{far}q)$ distributions calculated from Equations (5.54) and (5.55) using the LM1 parameters.

To determine the maximum invariant mass of Equation (5.53), we examine the calculation when $\phi_{\tilde{\chi}_1^0}$ are 0, $\frac{\pi}{4}$, $\frac{\pi}{2}$ and π. From the contour plots shown in Figure 5.14, the maximum value of Equation (5.53) always occurs when $\theta_{\tilde{l}}$ goes to zero and $\theta_{\tilde{\chi}_1^0}$ goes to π, for all values of $\phi_{\tilde{\chi}_1^0}$. Consequently, the maximum value of $m^2(l_{far}q)$ can be approximated by

$$m^2_{max}(l_{far}q) = \frac{(m^2_{\tilde{q}} - m^2_{\tilde{\chi}_2^0})(m^2_{\tilde{l}} - m^2_{\tilde{\chi}_1^0})}{m^2_{\tilde{l}}}. \tag{5.57}$$

5.4.1.3 Lepton charge asymmetry

Since charges of jets cannot be determined from experiments, the invariant mass distributions have to be calculated in forms of $m(l^+q)$ and $m(l^-q)$. These distributions can be described by the sum of the probability density functions in

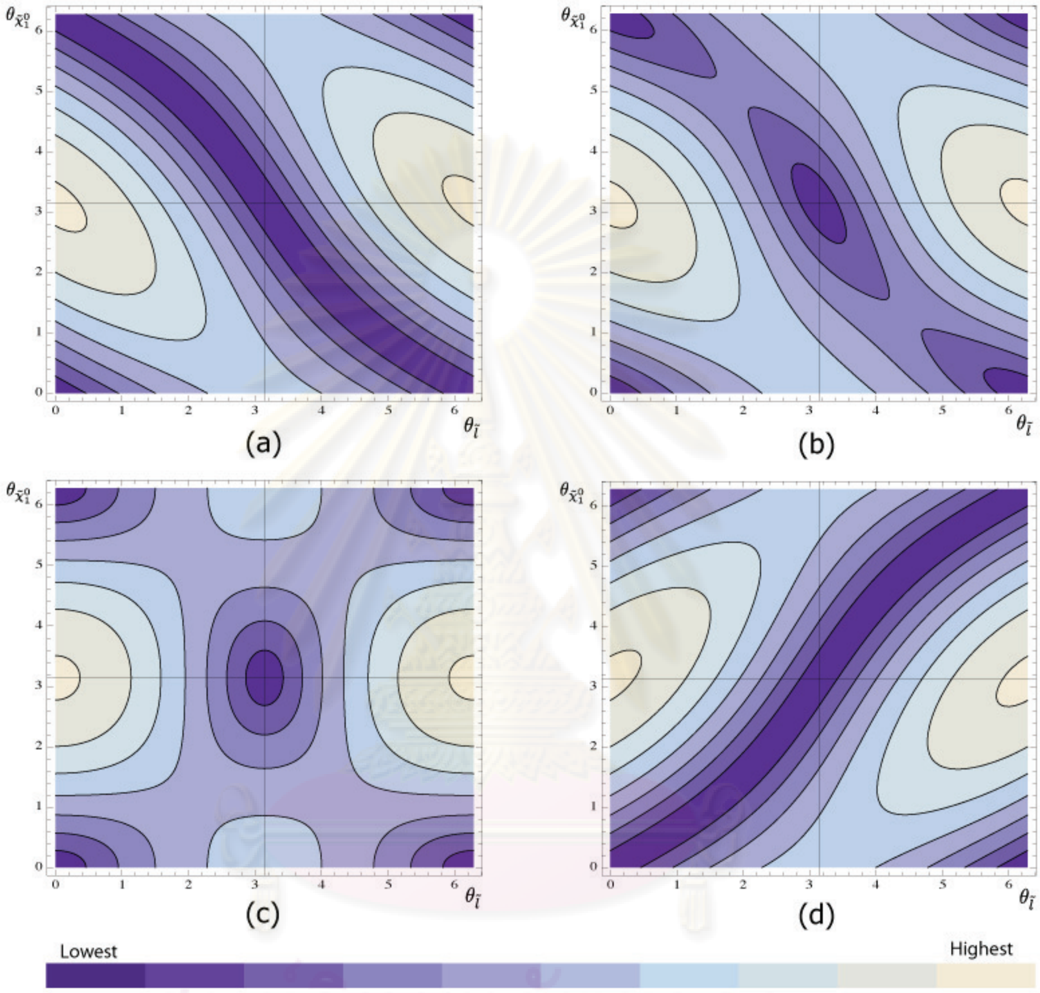

Figure 5.14: The contour plots represent the value of the Equation (5.53) when $\phi_{\tilde{\chi}_1^0}$ is equal to (a) 0, (b) $\frac{\pi}{4}$, (c) $\frac{\pi}{2}$ and (d) π. The x-axis shows the variation in $\theta_{\tilde{l}}$ while the y-axis shows in $\theta_{\tilde{\chi}_1^0}$.

Equations (5.48), (5.49), (5.54), and (5.55), which are [36]

$$\frac{d\Gamma}{dm_{l^+q}} = \frac{f_q}{2}\left(\frac{d\Gamma_1}{dx} + \frac{d\Gamma_3}{dx_f}\right) + \frac{f_{\bar{q}}}{2}\left(\frac{d\Gamma_2}{dx} + \frac{d\Gamma_4}{dx_f}\right), \tag{5.58}$$

$$\frac{d\Gamma}{dm_{l^-q}} = \frac{f_q}{2}\left(\frac{d\Gamma_2}{dx} + \frac{d\Gamma_4}{dx_f}\right) + \frac{f_{\bar{q}}}{2}\left(\frac{d\Gamma_1}{dx} + \frac{d\Gamma_3}{dx_f}\right). \tag{5.59}$$

The factor 1/2 in Equations (5.58) and (5.59) is normalization factors. The factors f_q and $f_{\bar{q}}$ are the quark and anti-quark fractions, respectively. The spin-dependent factors are hidden in $d\Gamma_1/dx$ and $d\Gamma_2/dx$. If the production rates of quark and anti-quark are equal ($f_q = f_{\bar{q}}$), we cannot obtain the spin information from experiments. At the LHC, the squark production rate are expected to be higher than anti-squark production from the presence of valance quarks of protons. This is due to the process of $gq \to \tilde{g}\tilde{q}$. The imbalance of the squark and anti-squark productions will lead to the imbalance of the probability density functions in Equations (5.48) and (5.49) which allows us to obtain the spin information from the decay chain of interest. Note that, the imbalance can be seen only through the first generation of squark since the types of valance quarks of protons are u and d. Figure 5.15 shows the invariant mass distributions of $m(l_{near}q)$, $m(l_{near}\bar{q})$, and their sum when the types of quarks are d, u, and others.

The lepton charge asymmetry defined in [28] is sensitive to the imbalance of the probability density functions in Equations (5.58) and (5.59). It was defined by

$$A \equiv \frac{d\Gamma/d(m_{l^+q}) - d\Gamma/d(m_{l^-q})}{d\Gamma/d(m_{l^+q}) + d\Gamma/d(m_{l^-q})}. \tag{5.60}$$

Figure 5.16 shows the calculated $m(l^+q)$ and $m(l^-q)$ distributions, and their lepton charge asymmetries for each study point. It is assumed that the anti-squark production rate is lower than squark production rate by 50% and only the first generation of squarks is used in the calculation of the edge limits of Equations (5.52) and (5.57). The left- and right-handed mixing of sleptons is also considered for the LM6. In experiment, an asymmetry dilution results from many reasons, which are

- The anti-squark production.

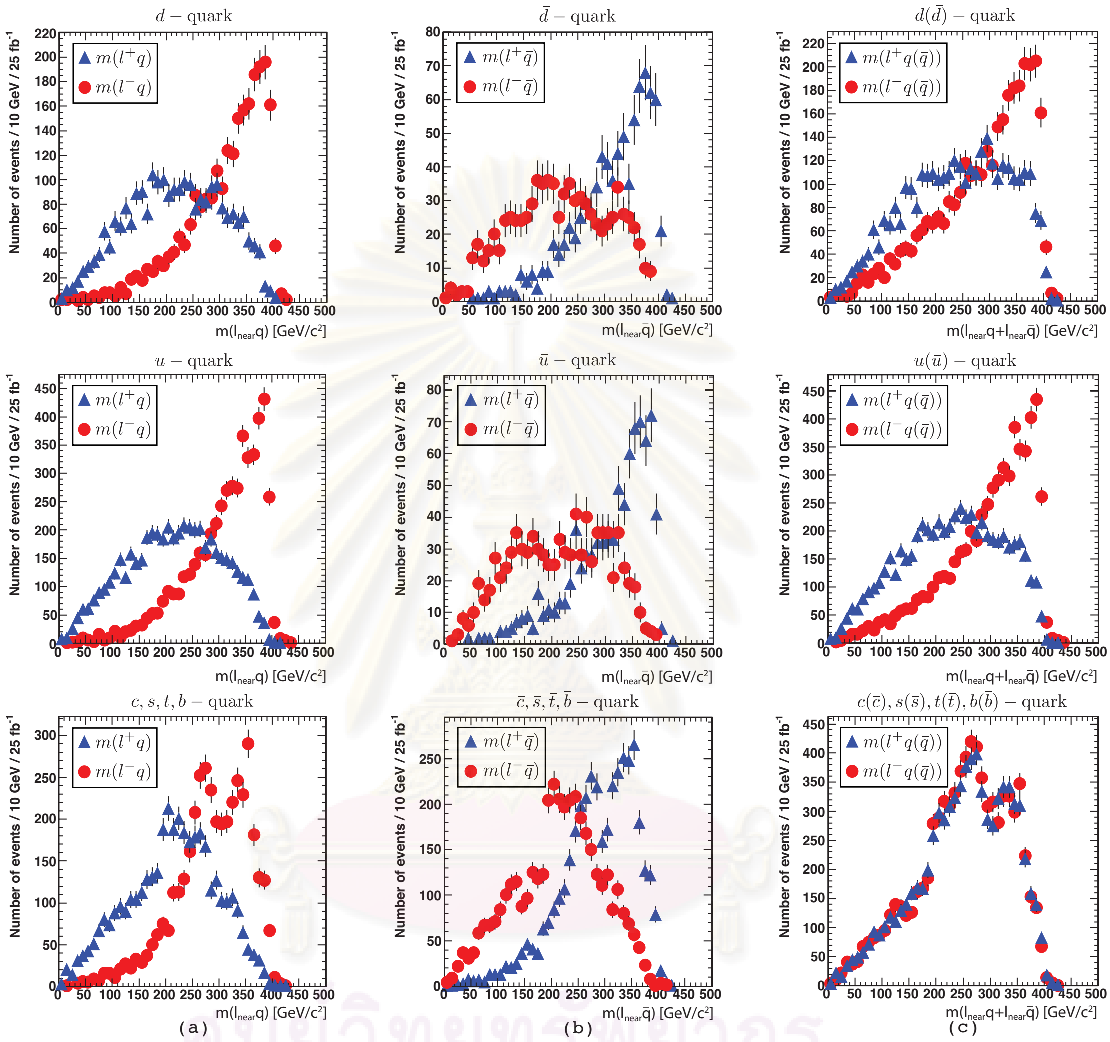

Figure 5.15: The sample of inclusive SUSY events at LM1 with integrated luminosity of 25 fb^{-1}. (a) The $m(l^{\pm}_{near}q)$ distributions. (b) The $m(l^{\pm}_{near}\bar{q})$ distributions. (c) The $m(l^{\pm}_{near}q) + m(l^{\pm}_{near}\bar{q})$ distributions.

- The contamination of reconstructed jets from the second and the third generations.

- The contamination of wrong reconstructed jets.

The double peaks of $m(l^{\pm}q)$ distributions shown in Figure 5.16 can be easily understood. They come from peaks of $m(l^{\pm}_{near}q)$ and $m(l^{\pm}_{far}q)$. To see clearly, the distributions of $m(l^{\pm}_{near}q)$, $m(l^{\pm}_{near}\bar{q})$ and $m(l^{\pm}_{far}q) + m(l^{\pm}_{far}\bar{q})$ will be shown separately in the next section.

5.4.2 Parton level analysis

In this section, we consider the results from the parton (generator) level. We, first, start by considering the missing transverse energy in parton level, then the distributions of interest, $m(l^{\pm}q)$, $m(l^{+}l^{-})$, $m(l^{+}l^{-}q)$, and asymmetry, are considered. Finally, the event selection is applied to see the sensitivity of the distributions of interest.

5.4.2.1 Missing transverse energy at the parton level

To define the missing transverse energy (MET) cut for the event selection, the missing transverse energy of the supersymmetric processes and some of Standard Model processes are plotted for comparison. MET can be calculated from Equation (5.31). Since the cross-sections of Standard Model processes are higher than SUSY processes, four cuts were applied at the parton level as a pre-selection to reduce the number of events from Standard Model processes. These cuts are listed in Table 5.6.

Figure 5.17 shows the MET distributions of the SUSY and Standard Model events which survive from the pre-selection cuts. From the figure, it is shown that we can set the missing transverse energy cut around 300 GeV to reject most on the Standard Model background, except Z + jet and $t\bar{t}$. It is noted that this cut

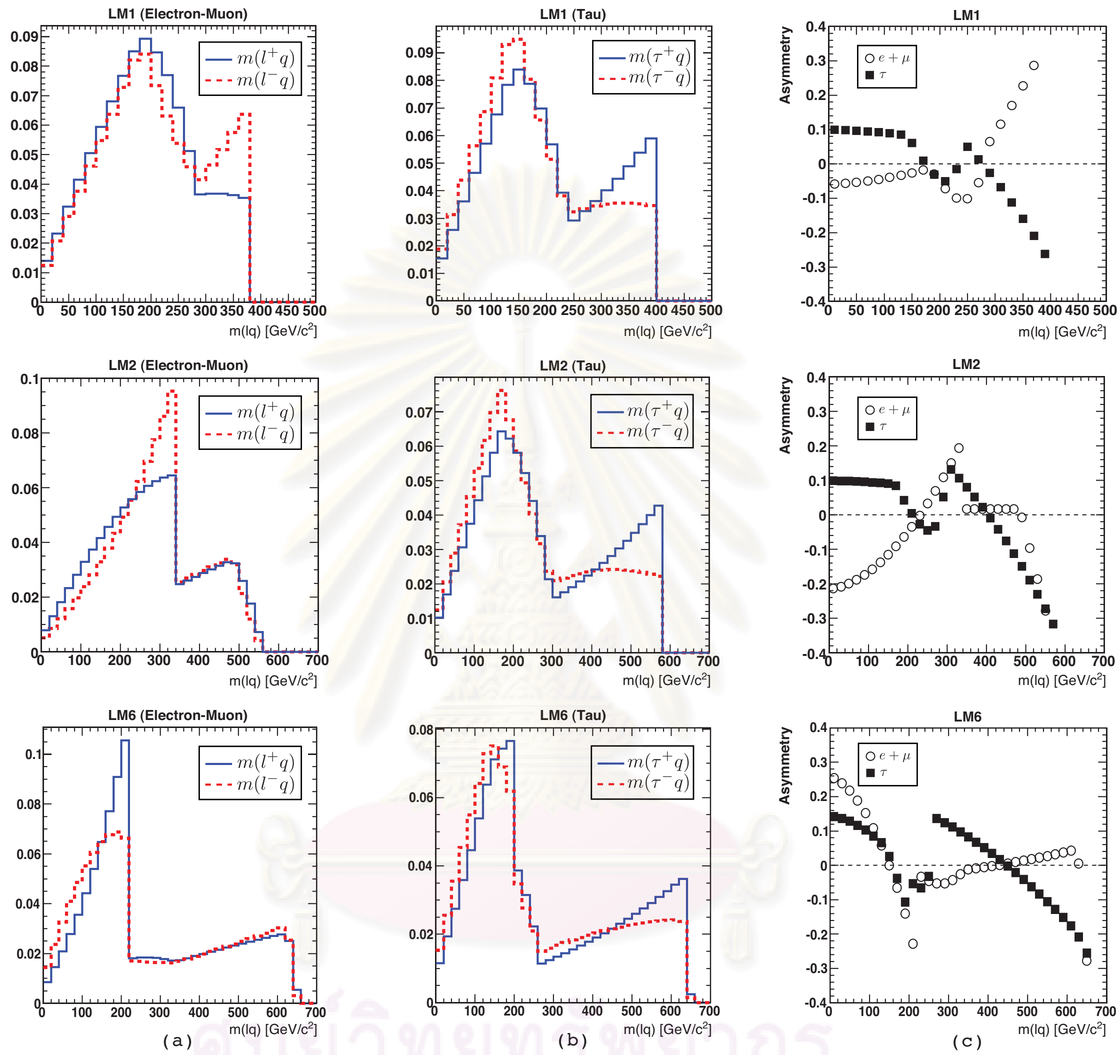

Figure 5.16: The calculated $m(l^{\pm}q)$ (a), and $m(\tau^{\pm}q)$ (b) distributions of LM1, LM2, and LM6. These distributions are normalized. The corresponding lepton charge asymmetries are shown in (c).

Cut	Threshold
(1) n_{quark} ($P_T > 50$ GeV/c)	≥ 3
(2) $n_{b-quark}$ ($P_T > 50$ GeV/c)	≤ 1
(3) The highest P_T quark	$P_T \geq 100$ GeV/c
(4) The type of highest P_T quark	not b-quark
(3) Leptons ($P_T > 10$ GeV/c)	At least, a pair of SFOS leptons exist.

Table 5.6: The pre-selection cuts. The SFOS lepton stands for "Same Flavor and Opposite Sign" lepton. Number of quarks are counted before hadronization step in parton level.

is approximate. In the detector level simulation and/or real data analysis, there are many selections we can add to reject the Standard Model background and the missing transverse energy can then be chosen to be somewhat lower than 300 GeV.

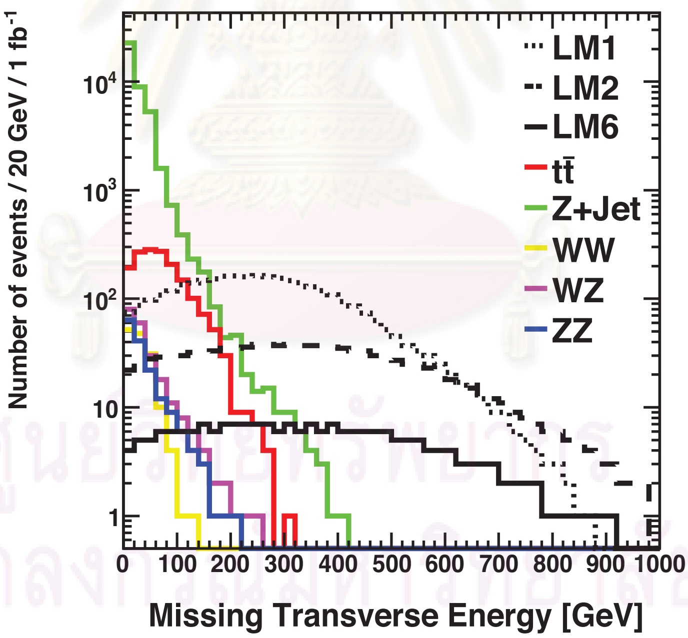

Figure 5.17: The generated missing transverse energy distributions of the SUSY and Standard Model events which pass the pre-selection criteria, described in Section 5.4.2.1.

5.4.2.2 Parton distributions

Figures 5.18 - 5.22 show the parton distributions of our three study mSUGRA points, LM1, LM2 and LM6. Each of the figures, (a) - (d) show the invariant mass distribution of $l_{near}q$, $l_{near}\bar{q}$, $l_{far}q + l_{far}\bar{q}$, $l^{\pm}q$, respectively. (e) shows the parton asymmetry plot and (f) shows the asymmetry after event selection. (g) and (h) show the invariant mass of the dilepton ($m_{l^+l^-}$), and the dilepton plus jet ($m_{l^+l^-q}$). An event selection was applied to demonstrate the sensitivity of the charge asymmetry. The event selection are

1. The parton MET is larger than 300 GeV.
2. The P_T of the selected quark and the leptons are larger than 100 and 20 GeV/c, respectively.
3. The pseudorapidity cut of jet and lepton follows the basic object selection discussed in Section 5.3. It includes $|\eta_{electrons}| < 2.5$, $|\eta_{muons}| < 2.1$, $|\eta_{taus}| < 2.4$, and $|\eta_{jets}| < 5.0$. The limit of pseudorapidity cut is based on the CMS.
4. The ΔR, calculated by Equation (5.4), between each pair of selected objects is larger than 0.3.
5. There are, at least, two of same flavor opposite sign (SFOS) leptons.

To be explicit about the effect of the left and right lepton mixing, shown in Figure 5.21(g), the dilepton invariant mass is shown separately, where the red line represents the lepton-far coming from the right-handed slepton, and the blue line represents the lepton-far coming from the left-handed slepton.

The double peaks of $m(l^{\pm}q)$ distributions can be seen clearly in this section. They come from superpositions of $m(l^{\pm}_{near}q(\bar{q}))$ and $m(l^{\pm}_{far}q(\bar{q}))$. One can also see the double or triple peaks in $m(l^{\pm}_{near}q(\bar{q}))$ or $m(l^{\pm}_{far}q(\bar{q}))$, i.e. in Figures 5.21(c), 5.22(a) and 5.22(b). To understand these, Equations (5.52) and (5.53) are considered. The maximum invariant masses of $m(l^{\pm}_{near}q)$ and $m(l^{\pm}_{far}q)$ depend

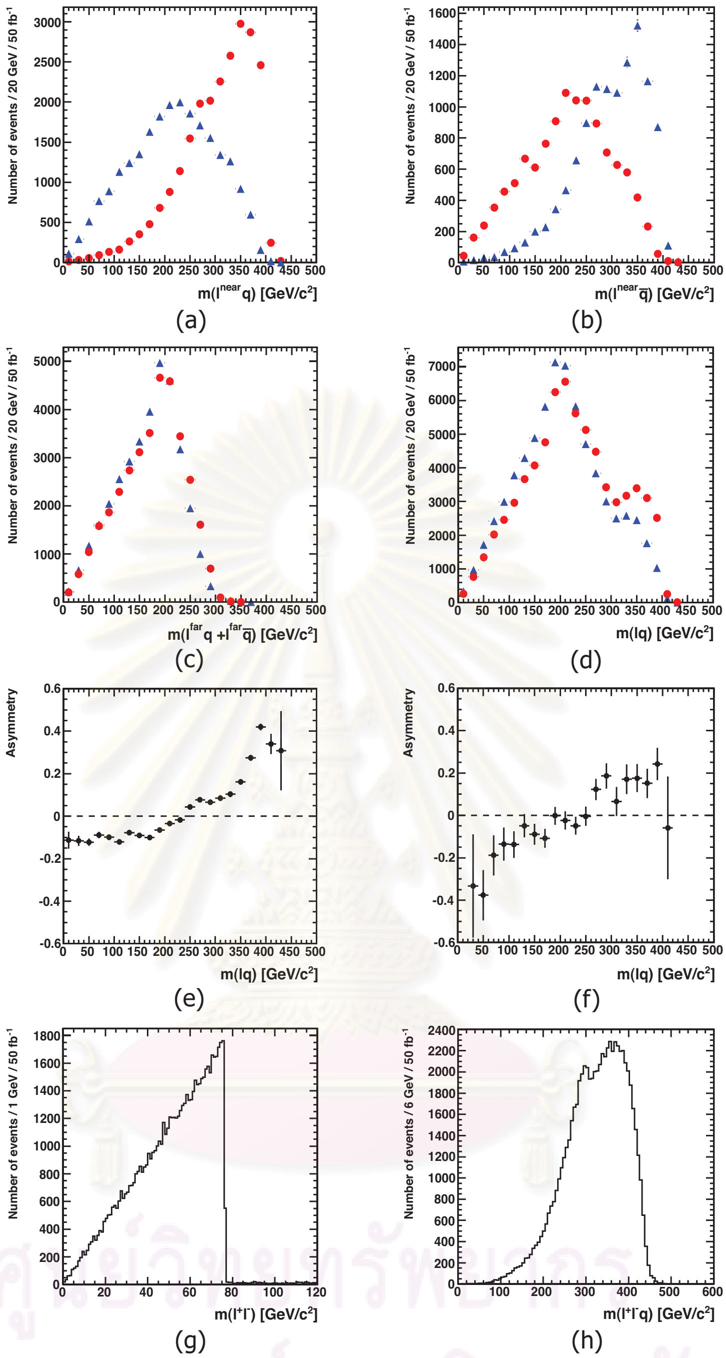

Figure 5.18: The invariant mass distributions of (a) $m(l_{near}q)$, (b) $m(l_{near}\bar{q})$, (c) $m(l_{far}q) + m(l_{far}\bar{q})$, and (d) $m(l^{\pm}q)$ for LM1 at 50 fb^{-1}. The blue-triangles (red-circles) refer to the negatively (positively) charged leptons. The parton electron-muon charge asymmetry distributions without (e) and with (f) kinematic cuts, and the invariant mass distributions of (g) $m(l^{+}l^{-})$, (h) $m(l^{+}l^{-}q)$.

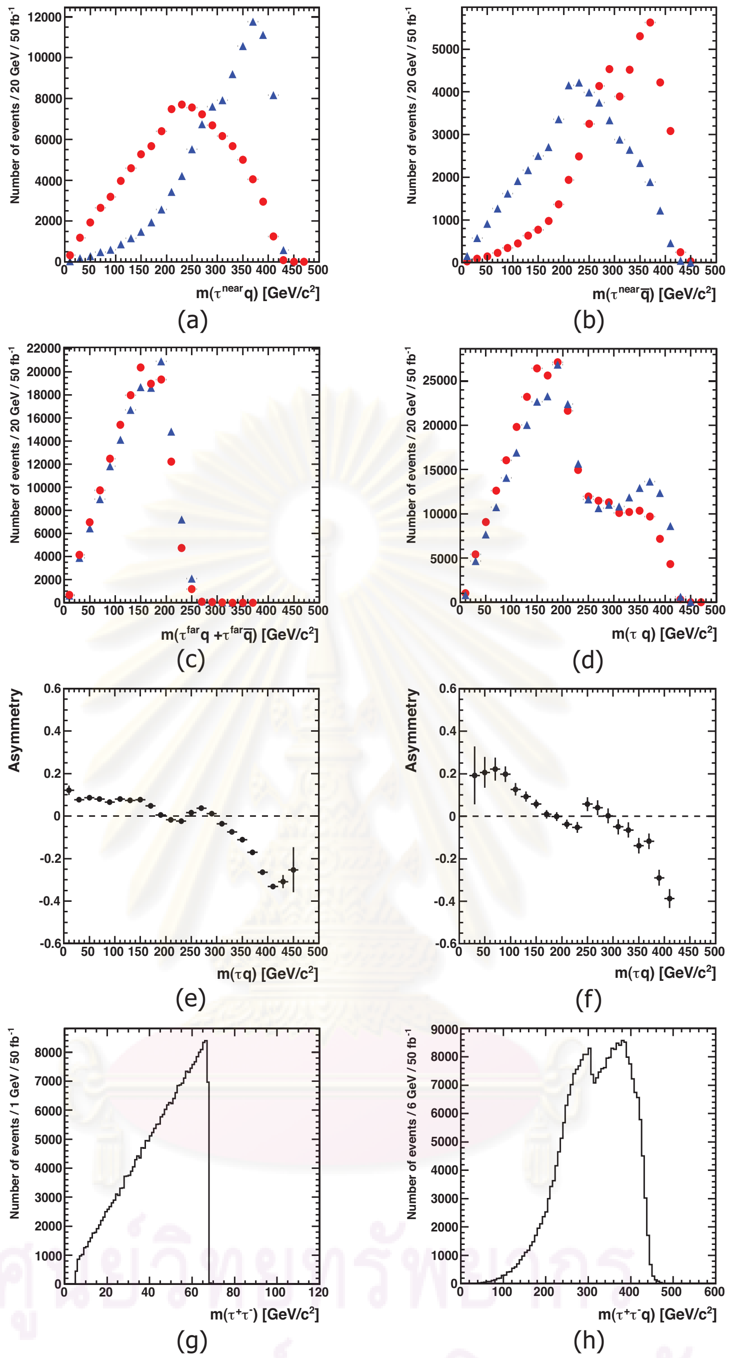

Figure 5.19: The invariant mass distributions of (a) $m(\tau_{near}q)$, (b) $m(\tau_{near}\bar{q})$, (c) $m(\tau_{far}q) + m(\tau_{far}\bar{q})$, and (d) $m(\tau^{\pm}q)$ for LM1 at 50 fb^{-1}. The blue-triangles (red-circles) refer to the negatively (positively) taus. The parton tau charge asymmetry distributions without (e) and with (f) kinematic cuts. The invariant mass distributions of (g) $m(\tau^+\tau^-)$, (h) $m(\tau^+\tau^-q)$.

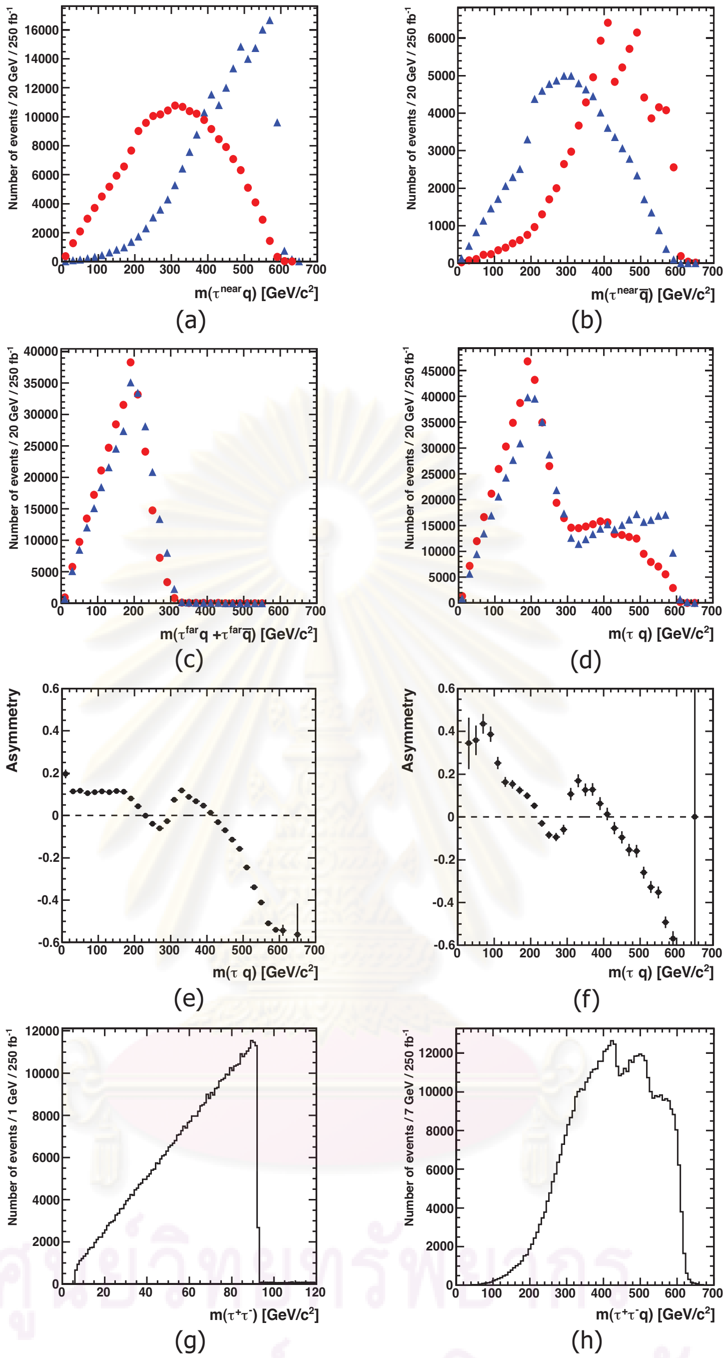

Figure 5.20: The invariant mass distributions of (a) $m(\tau_{near}q)$, (b) $m(\tau_{near}\bar{q})$, (c) $m(\tau_{far}q) + m(\tau_{far}\bar{q})$, and (d) $m(\tau^{\pm}q)$ for LM2 at 250 fb^{-1}. The blue-triangles (red-circles) refer to the negatively (positively) taus. The parton tau charge asymmetry distributions without (e) and with (f) kinematic cuts. The invariant mass distributions of (g) $m(\tau^{+}\tau^{-})$, (h) $m(\tau^{+}\tau^{-}q)$.

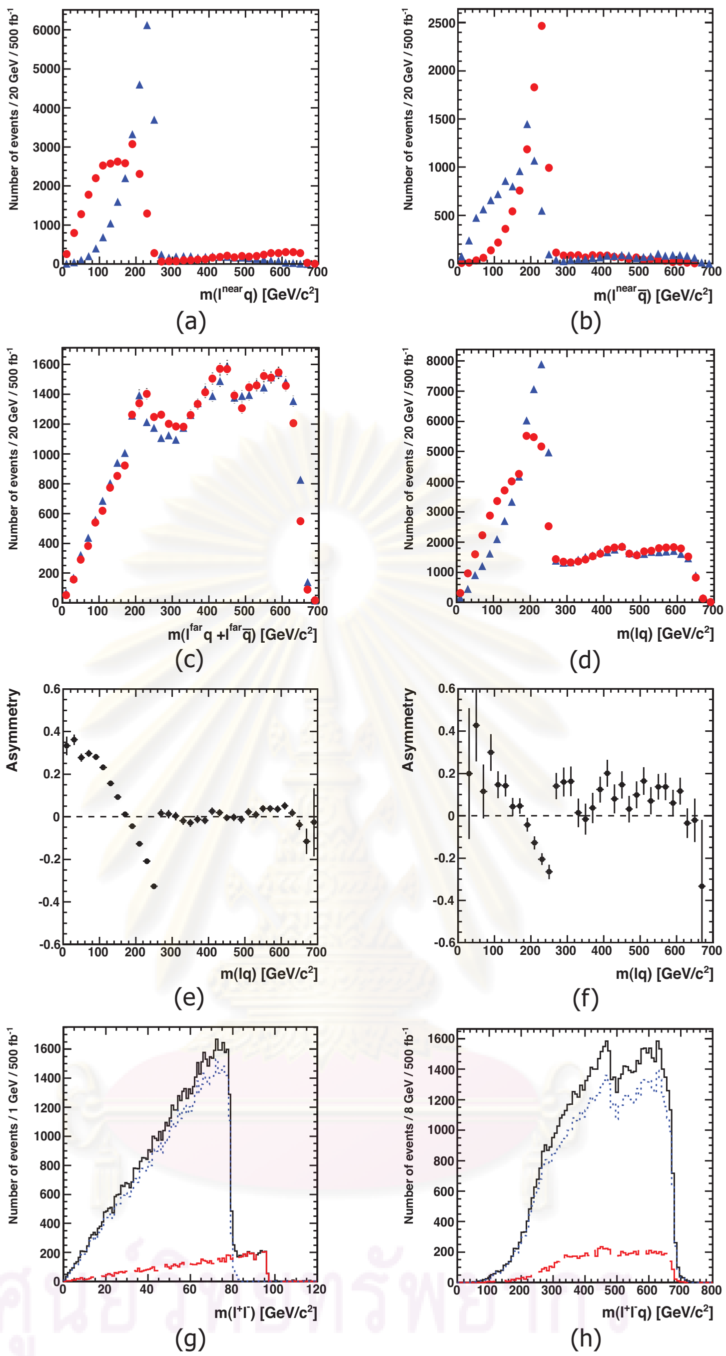

Figure 5.21: The invariant mass distributions of (a) $m(l_{near}q)$, (b) $m(l_{near}\bar{q})$, (c) $m(l_{far}q)+m(l_{far}\bar{q})$, and (d) $m(l^{\pm}q)$ for LM6 at 500 fb^{-1}. The blue-triangles (red-circles) refer to the negatively (positively) charged leptons. The parton electron-muon charge asymmetry distributions without (e) and with (f) kinematic cuts. The invariant mass distributions of (g) $m(l^+l^-)$, (h) $m(l^+l^-q)$. The red dashed line is for leptons coming from right-handed slepton, while the blue dotted line is for leptons coming from left-handed slepton. The solid line is the sum of all leptons.

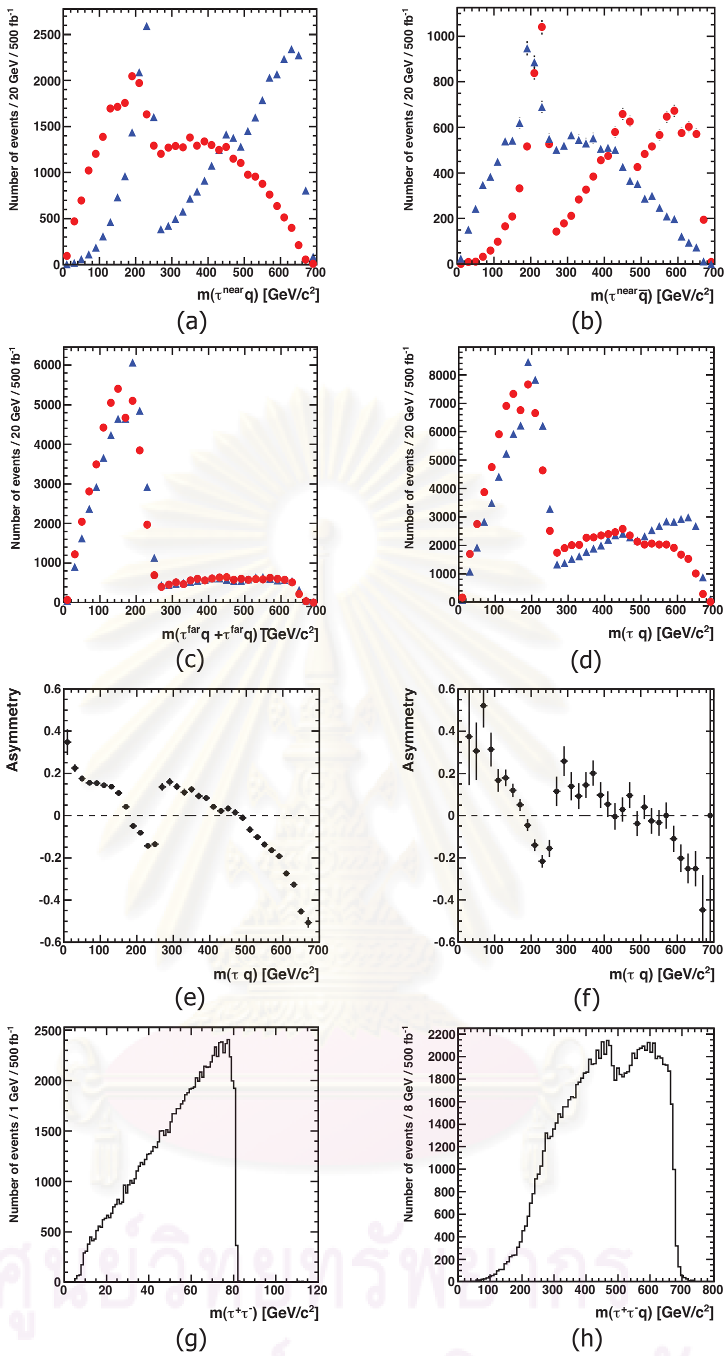

Figure 5.22: The invariant mass distributions of (a) $m(\tau_{near}q)$, (b) $m(\tau_{near}\bar{q})$, (c) $m(\tau_{far}q) + m(\tau_{far}\bar{q})$, and (d) $m(\tau^{\pm}q)$ for LM6 at 500 fb^{-1}. The blue-triangles (red-circles) refer to the negatively (positively) taus. The parton tau charge asymmetry distributions without (e) and with (f) kinematic cuts. The invariant mass distributions of (g) $m(\tau^+\tau^-)$, (h) $m(\tau^+\tau^-q)$.

on masses of squark and slepton. They also depend on masses of neutralinos, but we consider the decay chain via neutralino-2. The peaks in the distributions come from different types of squark and slepton under consideration. Note that, the mixing of left- and right- handed sleptons in the LM6 case causes the different peaks since their masses are not equal.

In addition, one can also see tails in the $m(l^{\pm}q)$ distributions, for examples, in Figures 5.19(c), 5.20(c), 5.21(a,b) and 5.22(c). These tails come from two reasons. First, they come from the mixing of the left- and right-handed sleptons as discussed previously but the number of events of interest is suppressed by one type of slepton. Examples of this case are shown in Figure 5.21(a,b) where the number of right-handed slepton production is suppressed by left-handed slepton. Second, these tails come from the contamination of $\tilde{\chi}_3^0$ and $\tilde{\chi}_4^0$ decays. These contamination effects can be seen in Figures 5.19(c), 5.20(c), and 5.22(c).

In summary, the invariant mass distributions from the parton level analysis agree with the theoretical distibutions presented in Figure 5.16. The applied kinematics cuts mainly affect the low invariant mass region, loss of asymmetry is expected to be observed in this region.

5.4.3 Detector level analysis

In this section, we demonstrate an event selection for the SUSY events to study the decay chain of interest, $\tilde{q} \rightarrow q\tilde{\chi}_2^0 \rightarrow ql^{\pm}_{near}\tilde{l}^{\mp} \rightarrow ql^{\pm}_{near}l^{\mp}_{far}\tilde{\chi}_1^0$. The final products of this decay chain of interest are di-leptons, jets, and missing transverse energy from the light supersymmetric particle (LSP) $\tilde{\chi}_1^0$. The CMS software is used to simulate data from detector and to reconstruct particles from simulation results. In this thesis, `FAMOS_1_6_0` and `CMSSW_3_3_4` are used for this study.

5.4.3.1 Detector level analysis using simulated data from `FAMOS_1_6_0`

Since this study was done in the beginning of the study, event selection was tested based on previous study in [28]. Note that, for this version of the detector simulation, the supersymmetric processes were generated at the benchmark points LM1 and LM6 since there is not tau tagging algorithm including in `FAMOS_1_6_0`. The event selection are

1. **Electrons**

   (a) The transverse momentum (P_T) of electrons is larger than 12 GeV/c.

   (b) The ΔR between two electrons is larger than 0.2.

   (c) The ΣP_T of the tracks within $\Delta R = 0.25$ around the electron is less than 5 GeV/c. The purpose of this step is to select the isolated electrons.

   (d) The likelihood for the electrons is larger than 0.65.

   Electrons which pass all cuts are called "good" electrons. Events which have at least two "good" electrons with opposite charge were selected (SFOS electrons).

2. **Muons**

   (a) The transverse momentum (P_T) of muons is larger than 10 GeV/c.

   (b) The ΔR between two muons is larger than 0.15.

   (c) The ΣP_T of the tracks within $\Delta R = 0.25$ around the muon is less than 5 GeV/c.

   Muons which pass all cuts are called "good" muons. Events which have at least two "good" muons with opposite charge (SFOS muons) were selected.

3. **Jets**

   (a) An iterative cone algorithm with $\Delta R = 0.5$ was used to reconstruct jets.

(b) At least two jets are required. The highest (2nd highest) leading P_T jets has P_T larger than 100 (50) GeV/c.

(c) The leading P_T jet was selected to calculate the invariant mass with the selected lepton.

4. **Missing energy**: Missing transverse energy (MET, $\vec{\not{E}}$) of an event is larger than 200 GeV, it was set based on previous studies.

5. **Edge cuts**: From the kinematics described in Sections 5.2.2 and 5.2.3, the invariant masses of l^+l^- and l^+l^-q must be less than or equal to limits shown in Table 5.7.

Model	Type of lepton	m_{ll}^{max}	m_{llq}^{max}
LM1	electron, muon	80	450
	tau	70	
LM2	tau	93	
LM6	electron, muon	79 (97)	685
	tau	81	

Table 5.7: The maximum invariant mass (GeV/c^2) of l^+l^- and l^+l^-q calculated from Equations (5.11) and (5.26). Only electron and muon limits are used in `FAMOS_1_6_0` analysis. Note that, the m_{ll}^{max} of the LM6 has two values, since there is mixing between left- and right-handed sleptons. The lower value is used as cut in this study, because the fraction of the right-handed slepton is suppressed by the left-handed slepton as one can see in Figure 5.21 (g). In addition, one can avoid the contamination from Z events with the lower value cut since the reconstructed invariant mass of Z boson is around 91 GeV/c^2.

If there are more than two opposite sign leptons passing the cuts, all possible combinations will be used for later analysis. In the invariant mass m_{lq} calculation, the leading P_T jet was used. Note that in this study, if both electrons and muons in an event can pass the event selection, they were combined in the results since the appropriate lepton selection came after this study.

Results of the LM1 study

Figure 5.23 shows the results from detector simulated data using `FAMOS_1_6_0` at the 65 fb^{-1} of supersymmetric events at benchmark point LM1 and the $t\bar{t}$ background. The yellow rectangles of the charge asymmetry distributions show the asymmetry of the parton distribution of the decay chain of interest. It was scaled down by a factor of 0.6. The scaled down factor is applied to the asymmetry of the parton distribution since there are dilutions from many reasons, as discussed in Section 5.4.1.3.

Only the $t\bar{t}$ background is included because the numbers of surviving events from other Standard Model processes were completely suppressed by the number of surviving events of the supersymmetric events. Table 5.8 shows the comparison of the surviving events using the event selection for the LM1 study.

Process	Integrated Luminosity (fb^{-1})	Number of surviving events
SUSY (LM1)	65	25420
$t\bar{t}$	65	968
WW	65	5
WZ	65	2
ZZ	65	0
Z + jet	1	4
W + jet	1	0

Table 5.8: The numbers of surviving events using the event selection with detector simulated data from `FAMOS_1_6_0`.

From the result (Figure 5.23), the charge asymmetry showed up clearly at the collected data at 65 fb^{-1}, specially on the high invariant mass region (> 250 GeV/c^2). The asymmetry is diluted in the low invariant mass region due to the number of surviving events from other supersymmetric decay chain and the Standard Model background. To improve the event selection, one may consider including the b-jet rejection, lepton selection method, pairing method to the algorithm. The improvement of the event selection will be discussed in Section 5.4.3.2.

Results of the LM6 study

The study of the charge asymmetry at the mSUGRA benchmark point LM6 was toward the end of the `COBRA` framework. The important problem found in this study point was the background from other supersymmetric decay processes. The number of the SUSY background event was larger than the interesting signal events. At an integrated luminosity of 400 fb^{-1}, the ratio of the surviving signal event to the surviving supersymmetric background event was 1:1.5. In addition, this ratio does not include the number of the surviving events from Standard Model background processes such as $t\bar{t}$ or Z+jets.

In this situation, the event selection needs to be made tighter. During this study, it was finally decided to migrate to the new framework where b and τ taggings were introduced. With the benefits of b and τ tagging algorithms, we can reject jets coming from B-hadrons, and can study the lepton charge asymmetry from τ candidates. The hemisphere separation was also planned to include in the analysis of the new framework. The hemisphere separation may help us to pair the correct objects and reduce the event contamination from e.g. $t\bar{t}$ where two leptons could come from different hemispheres.

The results of the LM6 benchmark point shown in Figures 5.24 and 5.25 are the results from detector simulated data at 65 fb^{-1} and 400 fb^{-1}, respectively. These results mixed with the $t\bar{t}$ background. The lepton charge asymmetry can be seen for the invariant masses between 100 and 150 GeV/c^2. In the low invariant mass region ($<$ 100 GeV/c^2), the dilution of asymmetry showed up as what we saw from the parton level study. This is due to the sensitivity of the invariant mass with the kinematic cuts applied in the event selection. The kinematic cuts include cuts in the transverse momentum and the missing transverse energy.

In conclusion, we studied the decay of interest, $\tilde{q} \rightarrow q\tilde{\chi}_2^0 \rightarrow ql_{near}^{\pm}\tilde{l}^{\mp} \rightarrow ql_{near}^{\pm}l_{far}^{\mp}\tilde{\chi}_1^0$, using electron and muon signals. Most of Standard Background processes can be ignored, except $t\bar{t}$. In this section, the fast detector simulation `FAMOS_1_6_0` was used to simulate detector results from supersymmetric events and $t\bar{t}$. For the LM1 benchmark point, lepton charge asymmetry shows up at an integrated luminosity of 65 fb^{-1}. The dilution of the asymmetry appears in the low invariant mass region ($<$ 250 GeV/c^2), while the lepton charge asymmetry shows up clearly in the region above 250 GeV/c^2. For the LM6, the number of surviving SUSY signal of interest is lower than the sum of other SUSY events and $t\bar{t}$, this leads to a dilution of the lepton charge asymmetry. The new event selection and new tagging algorithms will be proposed and be applied to the new simulated data using new CMS framework, called `CMSSW`. This will be introduced in the next section.

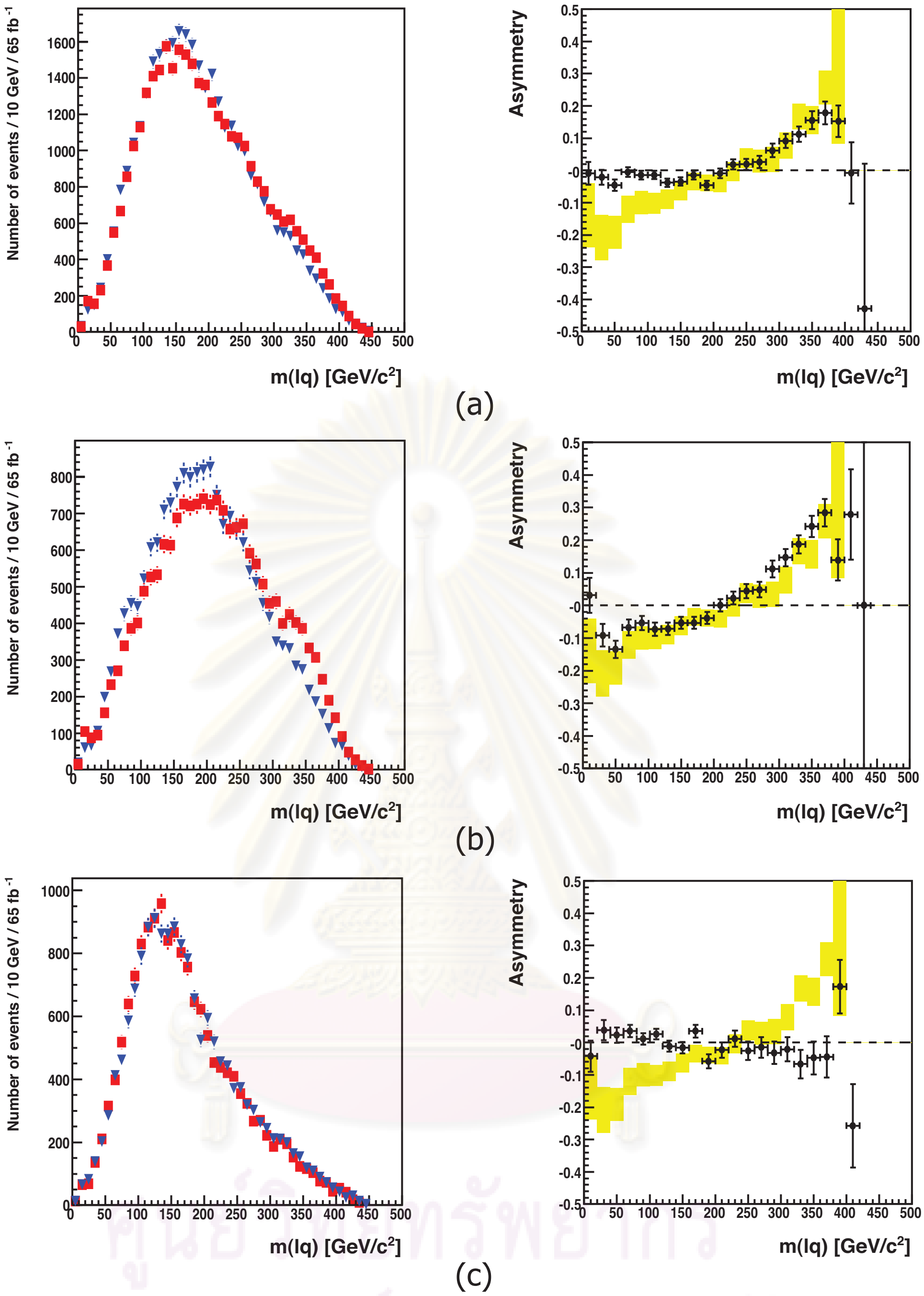

Figure 5.23: The invariant mass distributions of l^+q (red squares), and l^-q (blue triangles) and the corresponding lepton charge asymmetry distributions of (a) the mixing events between supersymmetric events (LM1) and the $t\bar{t}$ events, (b) the matched events between interesting signal and data selection of supersymmetric events, and (c) the combinatorial events of non-matched events and the $t\bar{t}$ events. The integrated luminosity of this data is 65 fb $^{-1}$.

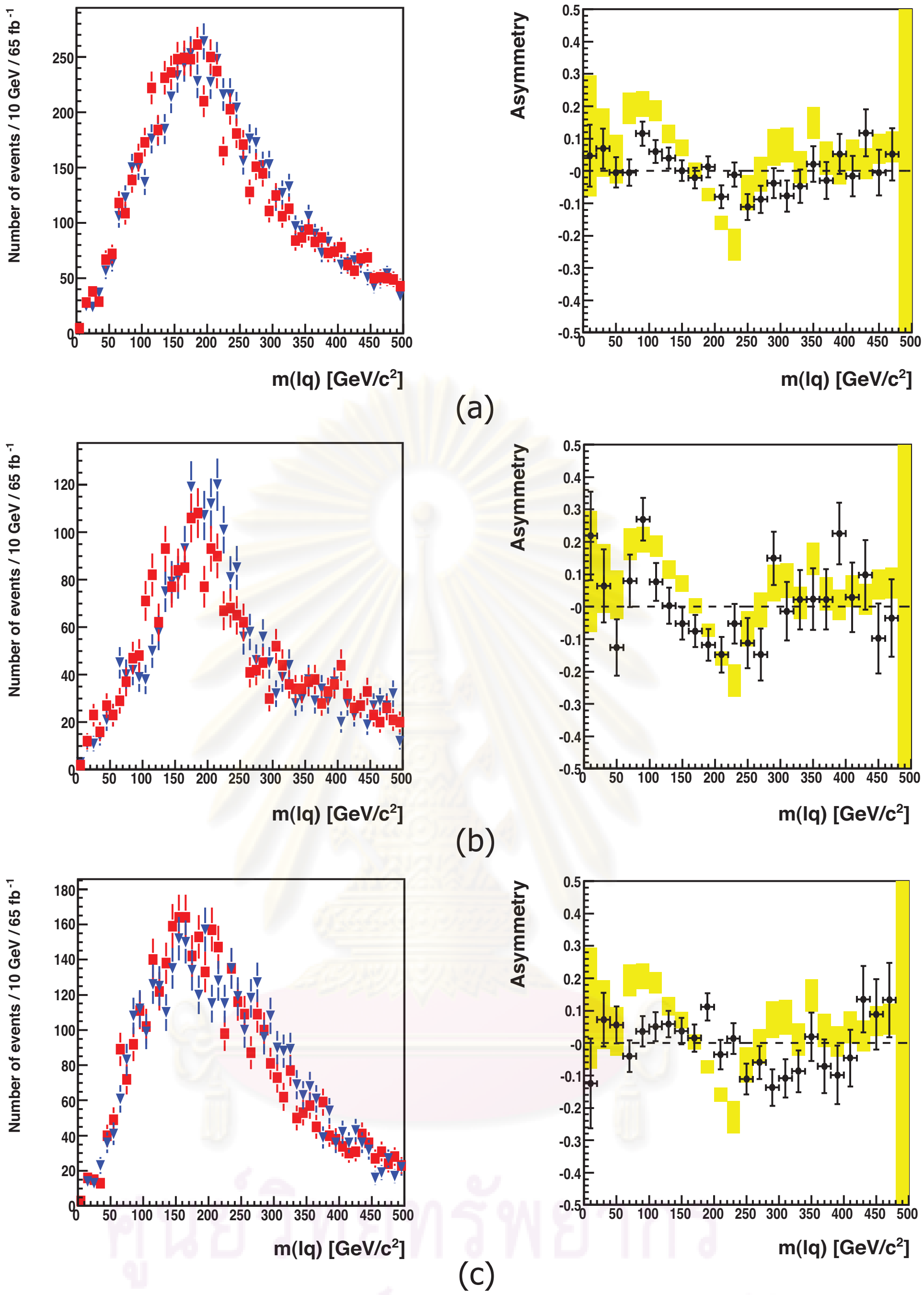

Figure 5.24: The invariant mass distributions of l^+q (red squares), and l^-q (blue triangles) and the corresponding lepton charge asymmetry distributions of (a) the mixing events between supersymmetric events (LM6) and the $t\bar{t}$ events, (b) the matched events between interesting signal and data selection of supersymmetric events, and (c) the combinatorial events of non-matched events and the $t\bar{t}$ events. The integrated luminosity of this data is 65 fb^{-1}.

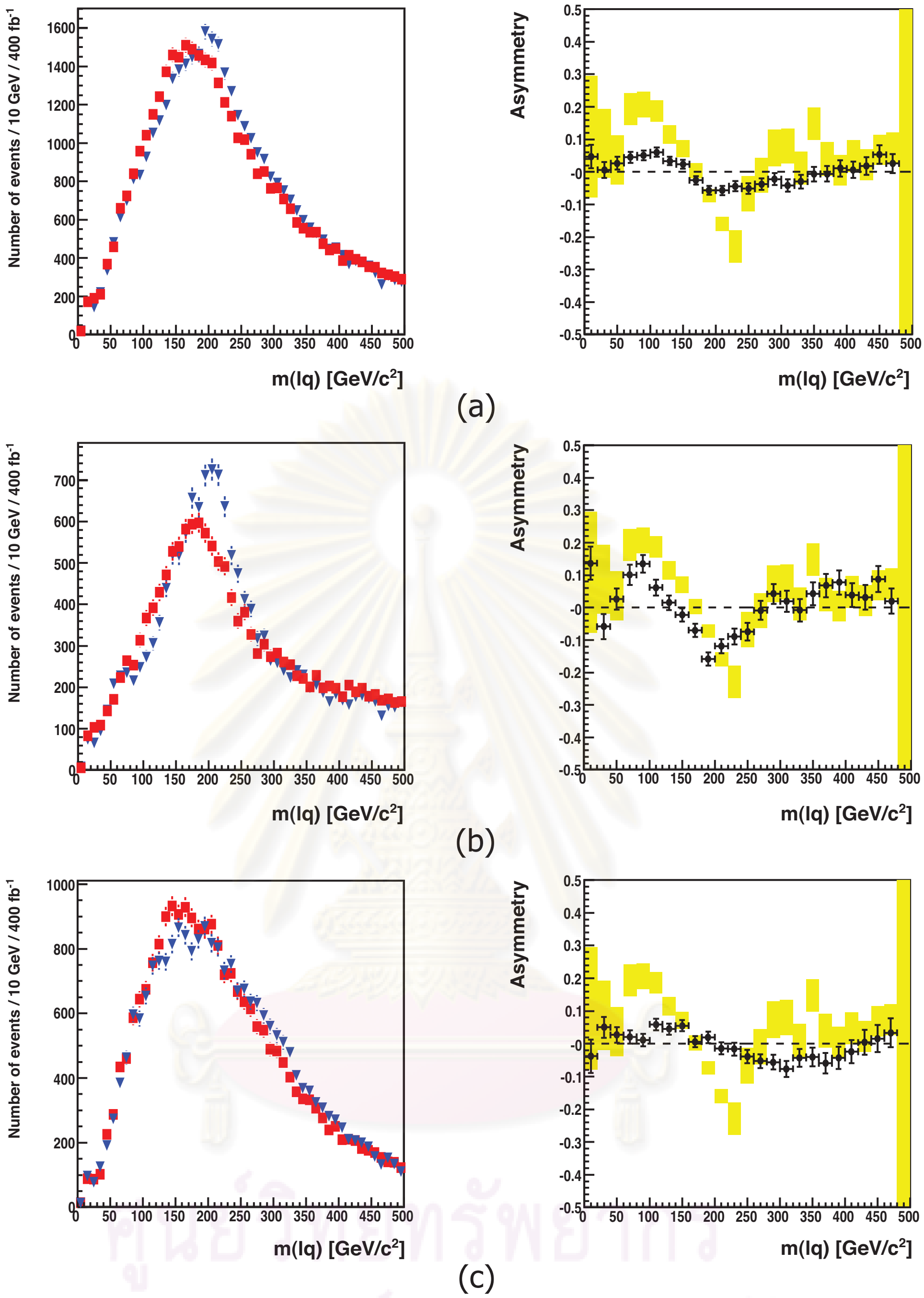

Figure 5.25: The invariant mass distributions of l^+q (red squares), and l^-q (blue triangles) and the corresponding lepton charge asymmetry distributions of (a) the mixing events between supersymmetric events (LM6) and the $t\bar{t}$ events, (b) the matched events between interesting signal and data selection of supersymmetric events, and (c) the combinatorial events of non-matched events and the $t\bar{t}$ events. The integrated luminosity of this data is 400 fb^{-1}.

5.4.3.2 Detector level analysis using simulated data from `CMSSW_3_3_4`

In this section, the analysis method for simulated data from `CMSSW_3_3_4` will be discussed. SUSY processes were generated at the LM1, LM2, and LM6 benchmark points. Electrons, muons, and taus were included to calculate lepton charge asymmetries. The b-tagging algorithm were also included to reduce the dilution of the lepton charge asymmetry, as discussed in Section 5.4.1.3. The event selection was improved from the results of `FAMOS_1_6_0`.

Physics object selection

In this section, we will consider an effective way to select the physics objects, such as leptons and jets, for analysis in `CMSSW_3_3_4`. One million events of LM1 was used as a sample of SUSY events. The study is divided into four cases (1) Using the highest P_T jet, (2) Using the 2nd highest P_T jet, (3) Using the hemisphere method to choose jet which matches with lepton, and (4) Using invariant mass of lepton and jet to select the proper jet. In each case, the analysis will be devided into five steps as follows,

- Step 0: Determine whether the event contains the decay chain of interest or not.
- Step 1: Apply the MET cut at 300 GeV, the maximum number of b-quarks is zero, and the minimum number of quarks is three. The MET threshold is set based on the study discussed in Section 5.4.2.1. With the MET threshold at 300 GeV, we may ignore the contamination from the Standard Model processes.
- Step 2: Search for the highest P_T reconstructed lepton. From Table 5.9, one can see that almost 97% of selected lepton will match with generated lepton in signal events.
- Step 3: Search for the appropriate jet from the four selection methods as mentioned previously. In the fourth case, the jet will be selected if the

invariant mass of jet and highest P_T lepton is smallest among the possible combinations.

- Step 4: Search for SFOS lepton(s). In the hemisphere case, the SFOS lepton has to be in the same hemisphere with the highest P_T lepton.

	Case 1: Highest P_T jet			Case 2: 2nd Highest P_T jet		
	Signal		Background	Signal		Background
	(All)	(Match)		(All)	(Match)	
Step 0	170882		829118	170882		829118
Step 1	12300		91714	12300		91714
Step 2	11919	11638	24303	11919	11638	24303
Step 3	11872	5978	24199	10648	5183	21466
Step 4	4994	3124	808	5880	3245	777

	Case 3: Hemisphere			Case 4: Invariant mass		
	Signal		Background	Signal		Background
	(All)	(Match)		(All)	(Match)	
Step 0	170882		829118	170882		829118
Step 1	12300		91714	12300		91714
Step 2	11919	11638	24303	11919	11638	24303
Step 3	11087	6265	22323	10866	6302	21898
Step 4	4754	3106	519	6519	3947	817

Table 5.9: The table shows the comparison between different selection methods, in order to find an appropriate way to select the physics objects. The "Signal (All)" means the events which contain the decay chain of interest, while "Signal (Match)" means the "Signal (All)" which the selected objects are matched with the interesting generated objects.

From Table 5.9, we can compare the efficiency for each case from the ratio of the matched events with total surviving events. The efficiencies of each case are

53.84%, 48.74%, 58.90%, and 53.80%, respectively. From this result, it is shown that the hemisphere method is a good choice to select and to pair the physics objects. We will use the hemisphere method to find the appropriate jet in the event selection. In addition, the hemisphere method also helps us to reject the Standard Model background, such as $t\bar{t}$, where the SFOS lepton comes from a different hemisphere.

Event selection

The event selection is based on the physics object selection discussed previously. In brief, the event selections are

1. Missing transverse energy $\geq$ 300 GeV.
2. $n_{jet}(P_T > 50\,GeV/c) \geq 3$ and the highest P_T jet is larger than 100 GeV/c.
3. $n_{b-jet}(P_T > 50\,GeV/c) = 0$.
4. The pseudorapidity cut of jet and lepton follows the basic object selection discussed in Section 5.3. It includes $|\eta_{electrons}| < 2.5$, $|\eta_{muons}| < 2.1$, $|\eta_{taus}| < 2.4$, and $|\eta_{jets}| < 5.0$.
5. At least a couple of the same flavor and opposite sign leptons exists. Both leptons have the P_T larger then 15 GeV/c in the case of electron-muon and 10 GeV/c in the case of tau. If there are more than two opposite sign leptons passing cuts, all possible combinations will be used for the analysis. The hemisphere matching between two leptons is included in the case of electron and muon.
6. The selected jet is one of the highest P_T jet, and the 2nd highest P_T jet. To determine which one, the hemisphere matching with selected lepton was applied. If both of them are on the same hemisphere with selected lepton, the highest P_T jet will be chosen. In the case of tau, the highest P_T jet will be chosen.

7. $m_{ll} \leq m_{ll}^{max}$. The m_{ll}^{max} is shown in Table 5.7.

8. $m_{llq} \leq m_{llq}^{max}$. The m_{llq}^{max} is shown in Table 5.7.

Tables. 5.10, 5.14, 5.15 show the number of surviving events at each step of event selection of the studied points, LM1, LM2 and LM6, respectively. Note that, the number of $t\bar{t}$ surviving events are also shown in these tables. One can see that the number of surviving events of $t\bar{t}$ is highly suppressed by the number of SUSY surviving events.

The meanings of steps of event selection are

- Step-0: Counting for the interesting decay chain.
- Step-1: MET and number of jets cuts.
- Step-2: Lepton selection.
- Step-3: Jet selection.
- Step-4: Object isolation.
- Step-5: Searching for SFOS lepton(s) which match with the selected lepton from Step-2.

Results at the LM1 benchmark point

Electron-Muon charge asymmetry: Results for electrons and muons at 50 fb^{-1} and 100 fb^{-1} shown on the left side of Figures. 5.26 and 5.27, respectively. The lepton charge asymmetries from electrons and muons can show up clearly. The asymmetries when the spin correlation is considered (called "spin-on") can be distinguished from the asymmetries when spin correlation is not considered (called "spin-off").

To show the tendency of the lepton charge asymmetries, they are fitted with the linear and quadratic polynomials. The fitting parameters and the chi-square statistics (discussed in Appendix. D) are shown in Tables 5.11 and 5.12 for linear and quadratic fittings, respectively. The fitting lines are shown with asymmetries in Figures 5.26 and 5.27 for data at integrated luminosity of 50 fb^{-1} and 100 fb^{-1}, respectively.

When the spin correlation is considered, the fitting line, which is described by a linear polynomials, tends to have a positive slope, while the slope is close to zero when the spin correlation is not considered. From the chi-square statistics, the large value of a reduced chi-square from spin-on fitting comes from the large variance of the first few bins. This behavior comes from the tight event selection which can cause the dilution in the low mass region as we saw from the result of the parton level study in Figure 5.18, or from the study with `FAMOS_1_6_0` in Figure 5.23. Note that, one may consider using quadratic polynomials fit to describe the electron-muon charge asymmetry. As we see from the chi-square statistics, the quadratic polynomials can describe the asymmetry tendency quite well. This can be seen from the reduce chi-square and the probability α.

Tau charge asymmetry: The tau charge asymmetries are shown in the right side of Figures. 5.26 and 5.27 for the integrated luminosity at 50 fb^{-1} and 100 fb^{-1}, respectively.

The fitting lines with the linear polynomials show similarity when the data is collected at 50 fb^{-1}. Both of "spin-on" and "spin-off" asymmetry distributions have a negative slope and their magnitudes are close to each other. To see the asymmetry tendency at high integrated luminosity, the Monte Carlo data had been raised up to 100 fb^{-1}, as shown in Figure 5.27. The tau charge asymmetry seems to show up clearer than before. The fitting line of "spin-on" data can maintain a negative slope while for the "spin-off" data, the slope of the fitting line goes to zero. One may observe a negative asymmetry and a large error bar in the first bin. This behavior can also be seen at the parton level analysis in Figure 5.19. This asymmetry dilution comes from the kinematics cuts which mostly effect the low invariant mass region.

	SUSY (LM1)		$t\bar{t}$	
	Signal	Background	Signal	Background
Step 0 (Spin-On)	304919	1659081	0	10M
Step 0 (Spin-Off)	341536	1658464	0	10M
Step 1(Spin-On)	69310	363457	0	4689
Step 1(Spin-Off)	69107	364240	0	4769
Step 2 (Spin-On)	21371	23226	0	898
Step 2 (Spin-Off)	31139	24103	0	948
Step 3 (Spin-On)	18468	19498	0	618
Step 3 (Spin-Off)	18229	20398	0	642
Step 4 (Spin-On)	17120	18407	0	482
Step 4 (Spin-Off)	16820	19251	0	510
Step 5 (Spin-On)	4727	2442	0	29
Step 5 (Spin-Off)	4653	2361	0	37

Table 5.10: The number of surviving events passing through each step of event selection. The number of sample of supersymmetric events (LM1) is 2M events which correspond to ∼50 fb^{-1}, while the number of $t\bar{t}$ events is 10M events which correspond to ∼25 fb^{-1}.

Note that, with the LHC data in 2010 ($\sqrt{s}$ = 7 TeV, $\int Ldt$ = 35 pb^{-1}) the LM1 benchmark point is excluded at 99.2% from the CMS experiment.

Results at the LM2 benchmark point

For the result at the LM2 benchmark point, we studied at 250 fb^{-1}. The result is shown in Figure 5.28. Table 5.13 shows the linear fitting parameters and the chi-square statistics. Table 5.14 shows the number of surviving events from the sample data. At this study point, the branching ratio of the decay of neutralino-2 to electrons and muons is completely suppressed by taus, hence we will limit the scope our study to the tau lepton only. Some branching ratios of SUSY decay

	Electron-Muon		Tau	
	LM1 (Spin-On)	LM1 (Spin-Off)	LM1 (Spin-On)	LM1 (Spin-Off)
	$50\ \text{fb}^{-1}$			
p_0	-0.181 ± 0.025	-0.004 ± 0.026	0.107 ± 0.040	0.063 ± 0.041
$p_1(10^{-5})$	93.79 ± 12.02	2.17 ± 12.43	-54.79 ± 19.27	-32.70 ± 19.42
ν	7			
χ^2	15.086	6.138	2.378	4.736
χ^2/ν	2.155	0.877	0.340	0.677
$Q(\chi^2, \nu)$	0.035	0.524	0.936	0.692
	$100\ \text{fb}^{-1}$			
p_0	-0.196 ± 0.018	-0.012 ± 0.018	0.094 ± 0.028	0.012 ± 0.028
$p_1(10^{-5})$	101 ± 8	6.62 ± 8.77	48.5 ± 13.8	-6.48 ± 13.65
ν	7			
χ^2	25.705	5.038	5.571	9.408
χ^2/ν	3.672	0.719	0.796	1.568
$Q(\chi^2, \nu)$	0.0005	0.655	0.591	0.225

Table 5.11: The fitting parameters from the linear polynomial (degree = 1) and the chi-square statistics from the LM1 data at 50 fb^{-1} and 100 fb^{-1}.

processes at the LM2 are shown in Section 2.2.1.

The tau asymmetry in Figure 5.28 (b) shows quite clearly that the linear fit has a negative slope. For the first few bins, the asymmetry is lower than what we expect. This can also be seen from the parton distribution shown in Figure 5.20, which is due to the transverse momentum cut on the selected objects. For the linear fit of the asymmetry when the spin correlation function is not considered, it is close to zero. The p_1 parameter of the "spin-off" data is lower than "spin-on" data with one order of magnitude and its p_0 covers the zero value. One can expect it to go to zero when higher statistics of data are used.

	Electron-Muon		Tau	
	LM1 (Spin-On)	LM1 (Spin-Off)	LM1 (Spin-On)	LM1 (Spin-Off)
	50 fb^{-1}			
p_0	-0.070 ± 0.051	-0.021 ± 0.053	0.112 ± 0.093	-0.086 ± 0.094
$p_1(10^{-4})$	-3.15 ± 5.14	2.16 ± 5.36	-6.05 ± 9.14	12.62 ± 9.23
$p_2(10^{-6})$	2.97 ± 1.18	-0.46 ± 1.24	0.13 ± 2.06	-3.66 ± 2.08
ν	6			
χ^2	8.80	6.00	2.37	1.63
χ^2/ν	1.47	0.99	0.39	0.27
$Q(\chi^2, \nu)$	0.185	0.423	0.882	0.950
	100 fb^{-1}			
p_0	-0.047 ± 0.036	-0.028 ± 0.037	0.135 ± 0.066	-0.115 ± 0.065
$p_1(10^{-4})$	-6.60 ± 3.66	2.38 ± 3.77	-9.24 ± 6.50	13.0 ± 6.38
$p_2(10^{-6})$	3.94 ± 0.84	-0.41 ± 0.87	1.01 ± 1.46	-3.17 ± 1.45
ν	6			
χ^2	3.63	4.82	5.09	4.61
χ^2/ν	0.60	0.80	0.85	0.77
$Q(\chi^2, \nu)$	0.727	0.567	0.532	0.598

Table 5.12: The fitting parameters from the quadratic polynomial (degree = 2) and the chi-square statistics from the LM1 data at 50 fb^{-1} and 100 fb^{-1}.

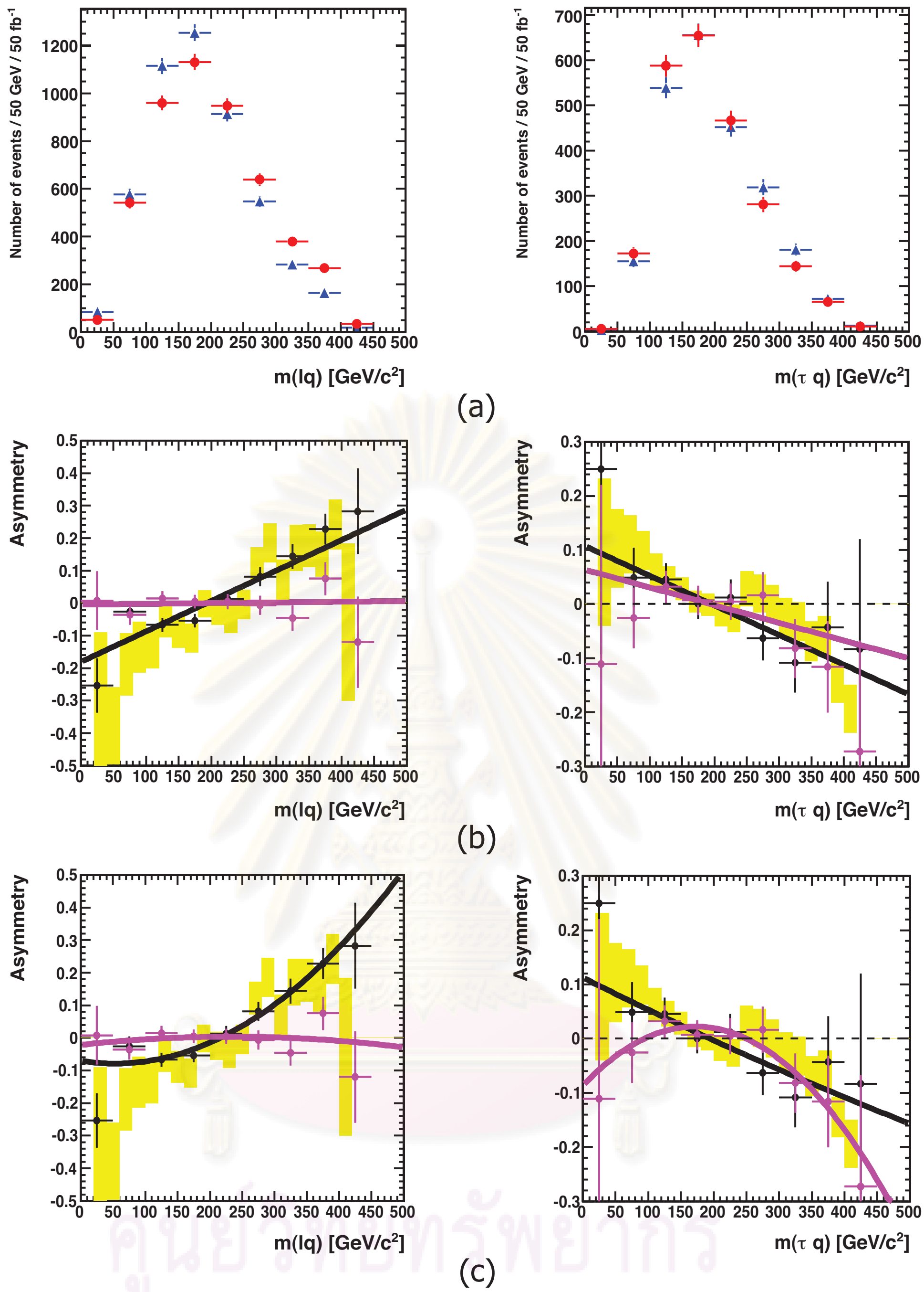

Figure 5.26: (a) The invariant mass distributions of l^+q (red circles) and l^-q (blue triangles) after the event selection using the fast simulation data for the LM1 point at the 50 fb^{-1}. The left side represents for electrons and muons, while the right side represents for taus. (b) The lepton charge asymmetry distributions. The yellow rectangles represent the idealized distribution after P_T selection is applied, they are scaled down by a factor of 0.5. The black and violet circles represent charge asymmetry after event selection of detector simulation data when the spin correlation is and is not considered, respectively. The data is fitted with linear polynomials. (c) The same as (b) but fitted with the quadratic polynomials.

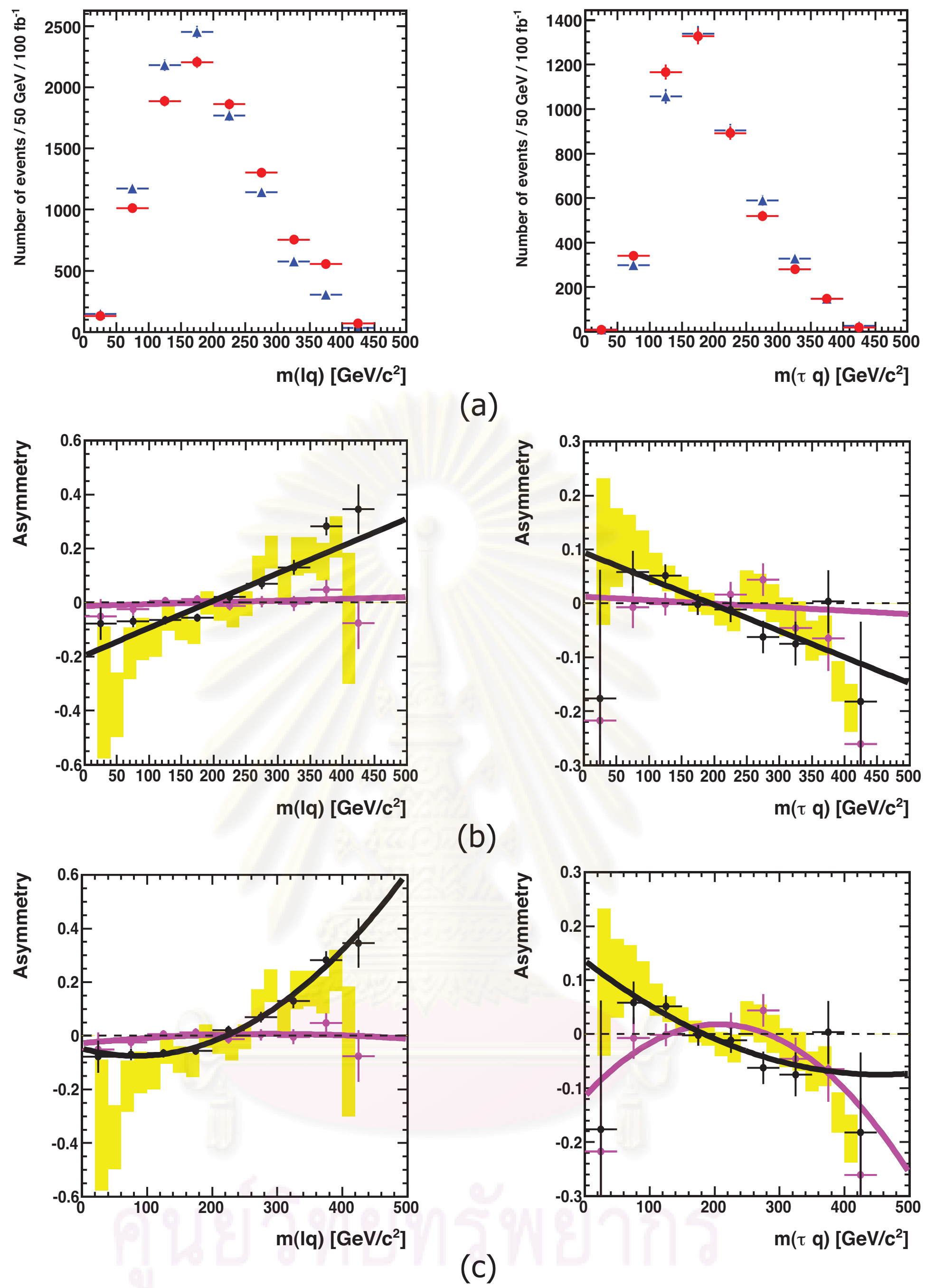

Figure 5.27: (a) The invariant mass distributions of l^+q (red circles) and l^-q (blue triangles) after the event selection using the fast simulation data for the LM1 point at the 100 fb^{-1}. The left side is for electrons and muons, while the right side is for taus. (b) The lepton charge asymmetry distributions. The yellow rectangles represent the idealized distribution after P_T selection is applied, they are scaled down by a factor of 0.5. The black and violet circles represent charge asymmetry after event selection of detector simulation data when the spin correlation is and is not considered, respectively. The data is fitted with linear polynomials. (c) The same as (b) but fitted with the quadratic polynomials.

	Tau	
	LM2 (Spin-On)	LM2 (Spin-Off)
p_0	0.134 ± 0.019	0.019 ± 0.019
p_1	-5.40×10^{-4}	-7.70×10^{-5}
ν	7	
χ^2	6.520	6.086
χ^2/ν	0.931	0.869
$Q(\chi^2, \nu)$	0.481	0.530

Table 5.13: The fitting parameters from the linear polynomial (degree = 1) and the chi-square statistics from the LM2 data at 250 fb^{-1}.

	SUSY (LM2)		$t\bar{t}$	
	Signal	Background	Signal	Background
Step 0 (Spin-On)	509764	1490236	0	10M
Step 0 (Spin-Off)	510947	1489053	0	10M
Step 1 (Spin-On)	152528	410746	0	4689
Step 1 (Spin-Off)	152824	410684	0	4769
Step 2 (Spin-On)	37774	27020	0	898
Step 2 (Spin-Off)	38281	26718	0	948
Step 3 (Spin-On)	33309	22781	0	618
Step 3 (Spin-Off)	33643	22569	0	642
Step 4 (Spin-On)	31539	20906	0	482
Step 4 (Spin-Off)	31797	20742	0	510
Step 5 (Spin-On)	6206	5160	0	37
Step 5 (Spin-Off)	6239	5209	0	46

Table 5.14: The number of surviving events passing through each step of event selection. The number of sample of supersymmetric events (LM2) is 2M events which correspond to ∼250 fb^{-1}, while the number of $t\bar{t}$ events is 10M events which correspond to ∼25 fb^{-1}.

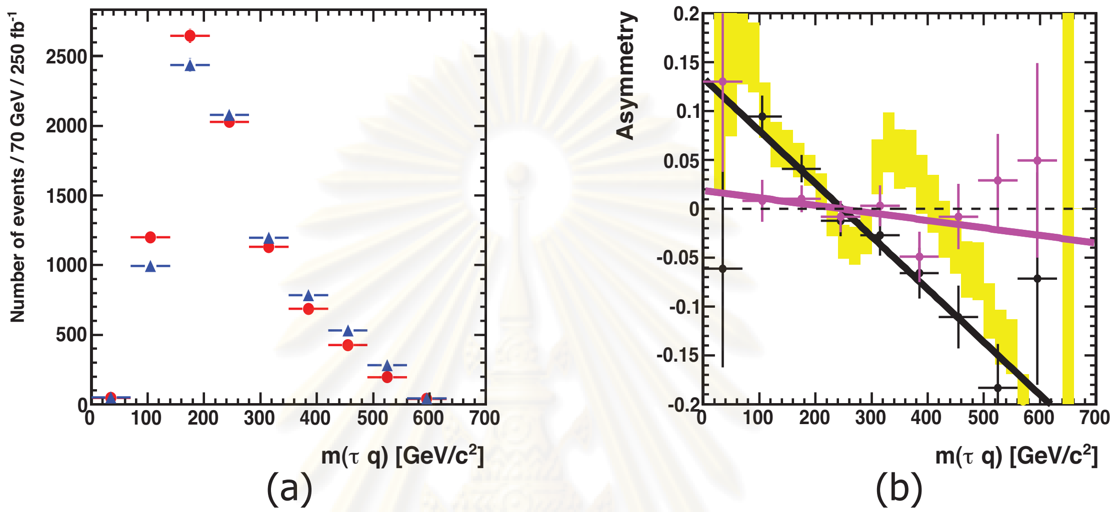

Figure 5.28: (a) The invariant mass distributions of l^+q (red circles) and l^-q (blue triangles) after the event selection using the fast simulation data for the LM6 point at the 250 fb^{-1}. The left side is for electrons and muons, while the right side is for taus. (b) The lepton charge asymmetry distributions. The yellow rectangles represent the idealized distribution after P_T selection is applied, they are scaled down by a factor of 0.5. The black and violet circles represent charge asymmetry after event selection of detector simulation data when the spin correlation is and is not considered, respectively. The data is fitted with linear polynomials.

Results at the LM6 benchmark point

For the study point LM6, 1000 fb^{-1} of simulated data was assumed. The number of the surviving events from the event selection is shown in Table 5.15, and the fitting parameters for the linear and quartic polynomials are shown in Table 5.16. Figure 5.29 shows the lepton charge asymmetries. The charge asymmetry from electrons and muons does not show clearly when an asymmetry distribution is fitted with quartic polynomials.

A clue of the spin correlation can be found from the rising of the asymmetry in a specific region where the contamination of left- and right-handed sleptons goes to the end. The origin of this region can be theoretically calculated from the maximum value of $m(l_{near}q)$, Equation (5.52), using masses of left- and right-handed sleptons. The parton level asymmetry shown in Figure 5.21 shows this clue clearly. At the lower invariant mass region ($<$ 300 GeV/c^2), the asymmetry depends mostly on the left-handed slepton, due to its higher production rate compared with right-handed slepton. For the high invariant mass region ($>$ 300 GeV/c^2), one can see the transition of the asymmetry, it rises up and stays close to zero afterward. With the linear fits to "spin-on" and "spin-off" data shown in Figure 5.29(c), we can separate them apart. The rising of the asymmetry of the invariant mass should be used to identify the charge asymmetry at this point of study.

For the tau analysis, even we can see the significant difference when the linear fit is applied, but the error bars are still large. The higher statistics is needed at this study point.

Since very high statistics is needed to study the asymmetry at the LM6 benchmark point, we then propose another supersymmetric decay chain which can be used to specify the spin of the newly produced particles with lower required statistics at this benchmark point. It will be discussed in the next section.

	SUSY (LM6)		$t\bar{t}$	
	Signal	Background	Signal	Background
Step 0 (Spin-On)	172005	1827995	0	10M
Step 0 (Spin-Off)	172310	1827690	0	10M
Step 1 (Spin-On)	64239	595273	0	4689
Step 1 (Spin-Off)	64367	593483	0	4769
Step 2 (Spin-On)	29640	78405	0	898
Step 2 (Spin-Off)	29812	78736	0	948
Step 3 (Spin-On)	25674	67050	0	618
Step 3 (Spin-Off)	25869	67445	0	642
Step 4 (Spin-On)	22499	59640	0	482
Step 4 (Spin-Off)	22599	59997	0	510
Step 5 (Spin-On)	6883	6312	0	36
Step 5 (Spin-Off)	6930	6329	0	50

Table 5.15: The number of surviving events passing through each step of event selection. The number of sample of supersymmetric events (LM6) is 2M events which correspond to $\sim$500 fb^{-1}, while the number of $t\bar{t}$ events is 10M events which correspond to $\sim$25 fb^{-1}.

	Electron-Muon		Tau	
	LM6 (Spin-On)	LM6 (Spin-Off)	LM6 (Spin-On)	LM6 (Spin-Off)
	Fitted with quartic polynomial (degree = 4)			
p_0	-0.069 ± 0.067	0.093 ± 0.067	0.227 ± 0.215	0.441 ± 0.212
$p_1(10^{-3})$	2.72 ± 1.13	-1.94 ± 1.13	-3.32 ± 3.44	-7.25 ± 3.36
$p_2(10^{-5})$	-2.27 ± 0.63	1.18 ± 0.63	1.29 ± 1.86	3.84 ± 1.81
$p_3(10^{-8})$	6.15 ± 1.39	-2.70 ± 1.38	-1.53 ± 4.09	-8.07 ± 3.95
$p_4(10^{-11})$	-5.11 ± 1.04	2.06 ± 1.04	0.35 ± 3.08	5.89 ± 2.98
ν	6			
χ^2	36.34	7.35	6.84	2.88
χ^2/ν	5.19	1.04	0.98	0.41
$Q(\chi^2, \nu)$	0.00	0.393	0.445	0.896
	Fitted with linear polynomial (degree = 1)			
p_0	-0.220 ± 0.023	0.025 ± 0.023	-0.165 ± 0.056	-0.034 ± 0.057
$p_1(10^{-4})$	6.30 ± 0.69	-0.64 ± 0.69	5.53 ± 1.74	1.16 ± 1.76
ν	5			
χ^2	7.14	1.57	6.81	3.69
χ^2/ν	1.43	0.31	1.36	0.74
$Q(\chi^2, \nu)$	0.727	0.567	0.532	0.598

Table 5.16: The fitting parameters from the quartic polynomial (degree = 4) and linear polynomial (degree = 1), and the chi-square statistics from the LM6 data at 1000 fb^{-1}.

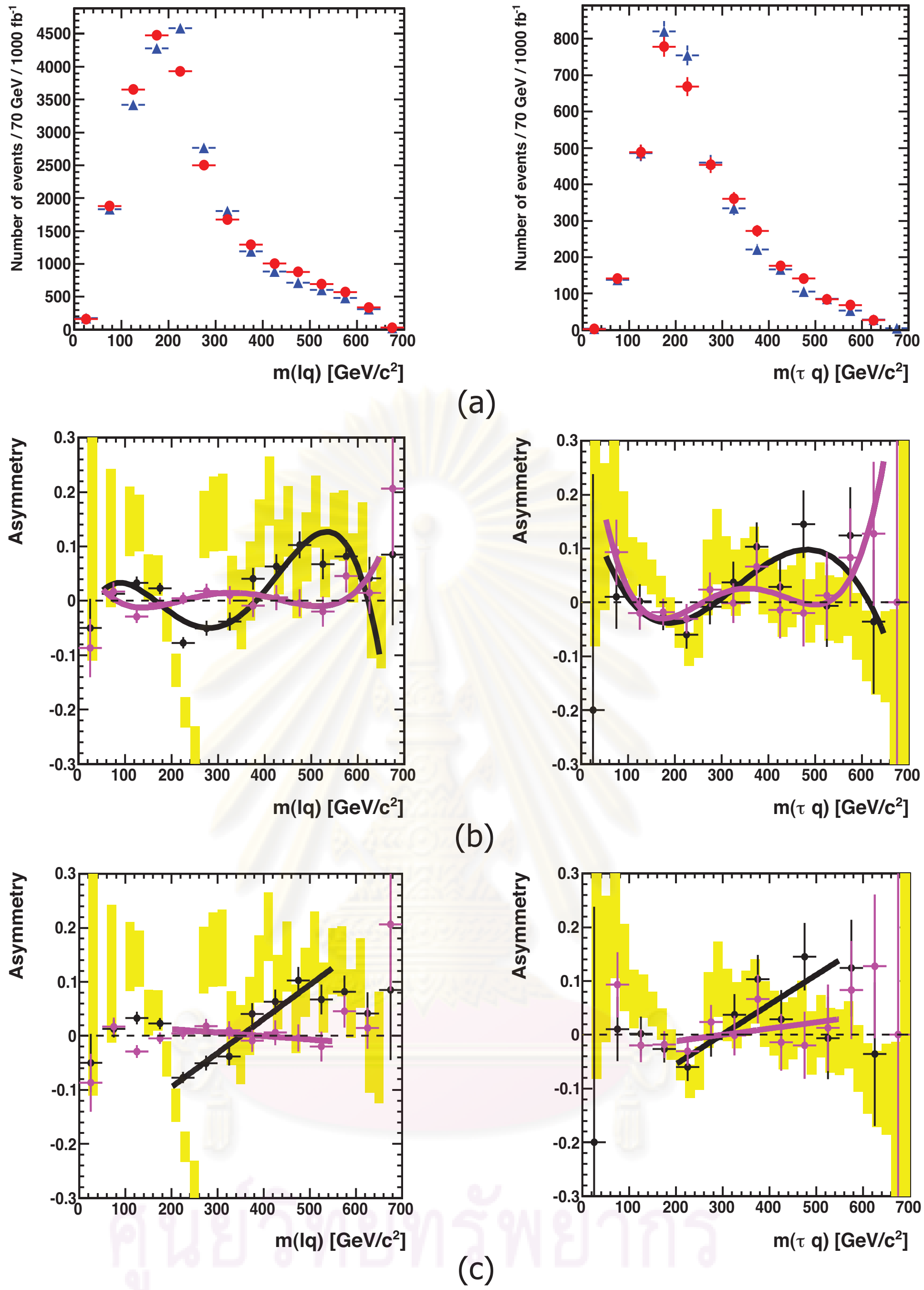

Figure 5.29: (a) The invariant mass distributions of l^+q (red circles) and l^-q (blue triangles) after the event selection using the fast simulation data of the LM6 point at the 1000 fb^{-1}. The left side is for electrons and muons, while the right side is for taus. (b) The lepton charge asymmetry distributions. The yellow rectangles represent the idealized distribution after P_T selection is applied, they are scaled down by a factor of 0.4. The black and violet circles represent charge asymmetry after event selection of detector simulation data when the spin correlation is and is not considered, respectively. The data is fitted with quartic polynomials (degree = 4). (c) The same as (b) but fitted with the linear polynomials in the range [200,500].

5.5 Spin correlations via chargino-1 decay chain

In this section, we consider the decay chain of stop (superpartner of top quark) via chargino-1 ($\tilde{\chi}_1^{\pm}$), shown in Equation (5.61) and Figure 5.30. To determine spins of sparticles using lepton charge asymmetry which was discussed in the previous section, a high statistics of data is required, specially for the LM6. In this study, we will study instead the invariant mass of the lepton and the b-jet from the decay chain of interest. Note that, in this decay chain of interest, the lepton charge asymmetry should not be used to determine the spin of chargino since the number of stop production should be the same as the number of anti-stop production.

$$\tilde{t}^{\pm} \to b^{\mp}\tilde{\chi}_1^{\pm} \to b^{\mp}l^{\pm}\tilde{\nu}_l \to bl^{\pm}\nu_l\tilde{\chi}_1^0 \tag{5.61}$$

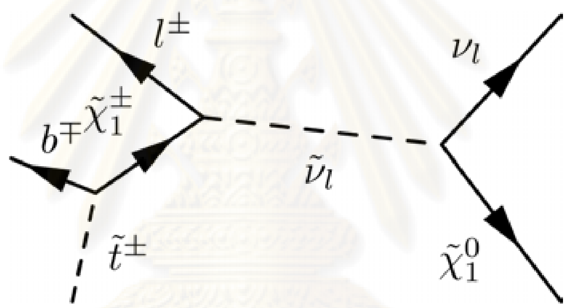

Figure 5.30: The decay chain of interest which decays via chargino-1.

5.5.1 Parton level analysis

As we did for the previous decay chain of interest, the parton distribution is considered first. The event selection is applied to the parton distributions, to see affects of basic cuts on the supersymmetric signal of interest. The missing transverse energy is determined by comparing the Monte Carlo missing transverse energy of SUSY and Standard Model processes.

5.5.1.1 Missing transverse energy at the parton level

To calculate missing transverse energy at the parton level, we apply pre-selection cuts as follows,

1. The minimum number of b-quarks ($P_T > 50$ GeV/c) in an event is one.
2. The minimum number of quarks ($P_T > 50$ GeV/c) in an event is three.
3. The highest P_T of b-quark is larger than 160 GeV/c.
4. The highest P_T of lepton is larger than 15 GeV/c.

The minimum number of b-quarks can be set to 2, if we consider that most of the decay chain of interest starts from gluino. However, due to the efficiency of b-tagging we may lose some b-jets. For this reason, we will set the minimum number of b-quark to 1.

Figure 5.31 shows the missing transverse energy distribution of SUSY and Standard Model events which survive from the pre-selection cuts. From the distribution, it is shown that we should set the missing transverse energy criteria around 300 GeV to reject most of the Standard Model background except $t\bar{t}$. Some of Z+jet events can survive, but the ratio of Z+jet surviving events is suppressed by SUSY and $t\bar{t}$ processes, so we ignore this process in this study.

5.5.1.2 Parton distributions

As we did for the study of the previous decay chain, the event selection is applied to the parton distributions in order to check the sensitivity. For this decay chain of interest, the event selection includes,

1. The MET is greater than 300 GeV.
2. The highest P_T of lepton is larger than 15 GeV/c.

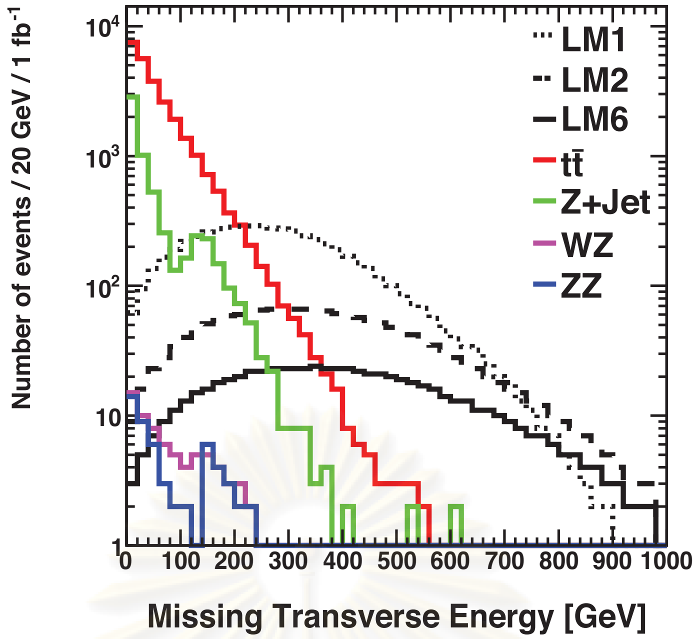

Figure 5.31: The Monte Carlo missing transverse energy distribution, using pre-selection cuts listed in Section 5.5.1.1.

3. The highest P_T of b-quark is larger than 160 GeV/c.

4. The pseudorapidity cut of jet and lepton follows the basic object selection discussed in Section 5.3.

5. The ΔR between b-quark and lepton is larger than 0.3.

The parton invariant mass distributions from lepton and b-quark are shown in Figure 5.32 with the spin correlation function on (considered) and off (not considered). The figure on the right represents the distribution after the event selection. One can see that the figures on both sides show the same shape, the figure on the right side is scaled down from the the figure on the left. In summary, with the event selection, the invariant mass distribution of lepton and b-quark can maintain the shape of original parton distribution. In the supersymmetry case, the distribution can be described by the probability density function used for the opposite-sign lepton and jet which we used to describe the SUSY decay chain via neutralino-2 [38].

$$\frac{1}{\Gamma} = 4x(1 - x^2), \tag{5.62}$$

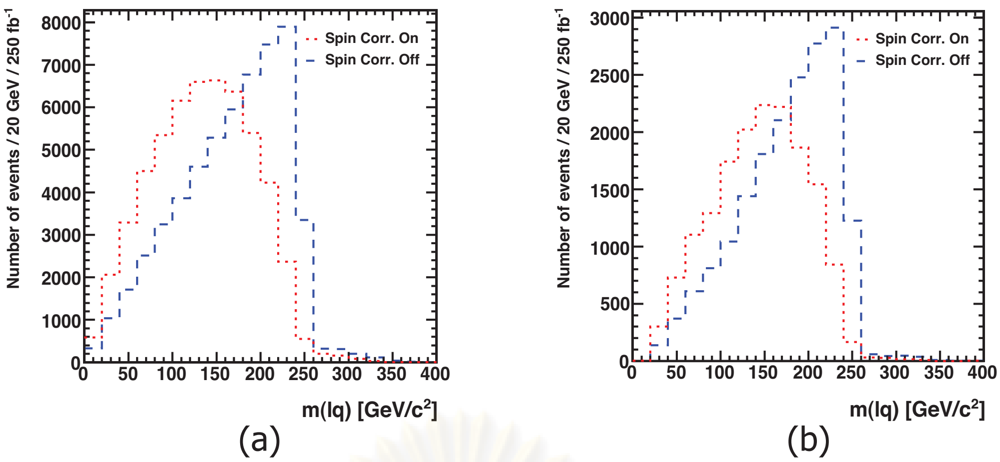

Figure 5.32: The lepton and b-quark invariant mass distributions. The dotted line represents the invariant mass when spin correlations is considered, and the dashed line is when the spin correlations is not considered. The left side shows the parton distribution at the 250 fb^1, and the right side show the distributions after the event selection at the same integrated luminosity.

where x is defined by $m_{lq}/m_{lq,max}$. For the spin-off case, the distribution can be described by the phase-space distribution as described by Equation (5.44).

5.5.1.3 Event selection at the parton level

Due to the limited constraints on the products from the decay chain of interest, one would expect a huge background from the decay products of other supersymmetric particles or t-quarks. The mismatch could happen when b-jets coming from decays of gluinos or t-quarks and leptons coming from neutralino decay. To show how the background from another supersymmetric decay chain, Standard Model background, and mis-selection affect the parton distribution, we apply the event selection to the general SUSY and Standard Model events. In brief, the event selection requires,

1. MET $>$ 300GeV.

2. $n_{quark}(P_T > 50$ GeV/c$) \geq 3$.

3. $n_{b-quark}(P_T > 50 \text{ GeV/c}) \geq 1$.

4. The highest P_T b-quark (≥ 160 GeV/c) is selected.

5. The highest P_T^{lepton} (≥ 15 GeV/c) is selected.

6. The pseudorapidity cut of jet and lepton follows the basic object selection discussed in Section 5.3. It includes $|\eta_{electrons}| < 2.5$, $|\eta_{muons}| < 2.1$, $|\eta_{taus}| < 2.4$, and $|\eta_{jets}| < 2.4$. Note that, since b-tagging uses the track information, the pseudorapidity of jet is limited by tracker.

7. The ΔR between b-quark and lepton is larger than 0.3.

8. To avoid the b-quarks from top quark decays, the number of quarks or leptons within the cone size of 0.7 from the selected b-quark is equal to 0. To compare the efficiency of this cut, the distribution without this step is also shown.

Note that, the efficiency of b-discriminator is not considered in the parton level.

The parton level invariant mass of lepton and b-quark distributions are shown in Figure 5.33. One can see that the top rejection (the eighth cut) can reduce the number of $t\bar{t}$ significantly. This distributions are presented as the stacked histograms, the meanings of each layer are described in the caption of the figure. One can see from the figure that the distributions are mainly coming from the red layer, which represents the surviving SUSY events that do not contain the decay chain of interest.

From the results, one can see that if the newly produced particles are not particles which have the spin difference by $\frac{\hbar}{2}$ (supersymmetric particles in our case), an extra peak which corresponds with the maximum invariant mass of lepton and b-quark should appear. This peak can be considered as the peak of invariant mass of lepton and b-quark of the phase-space decay chain of interest.

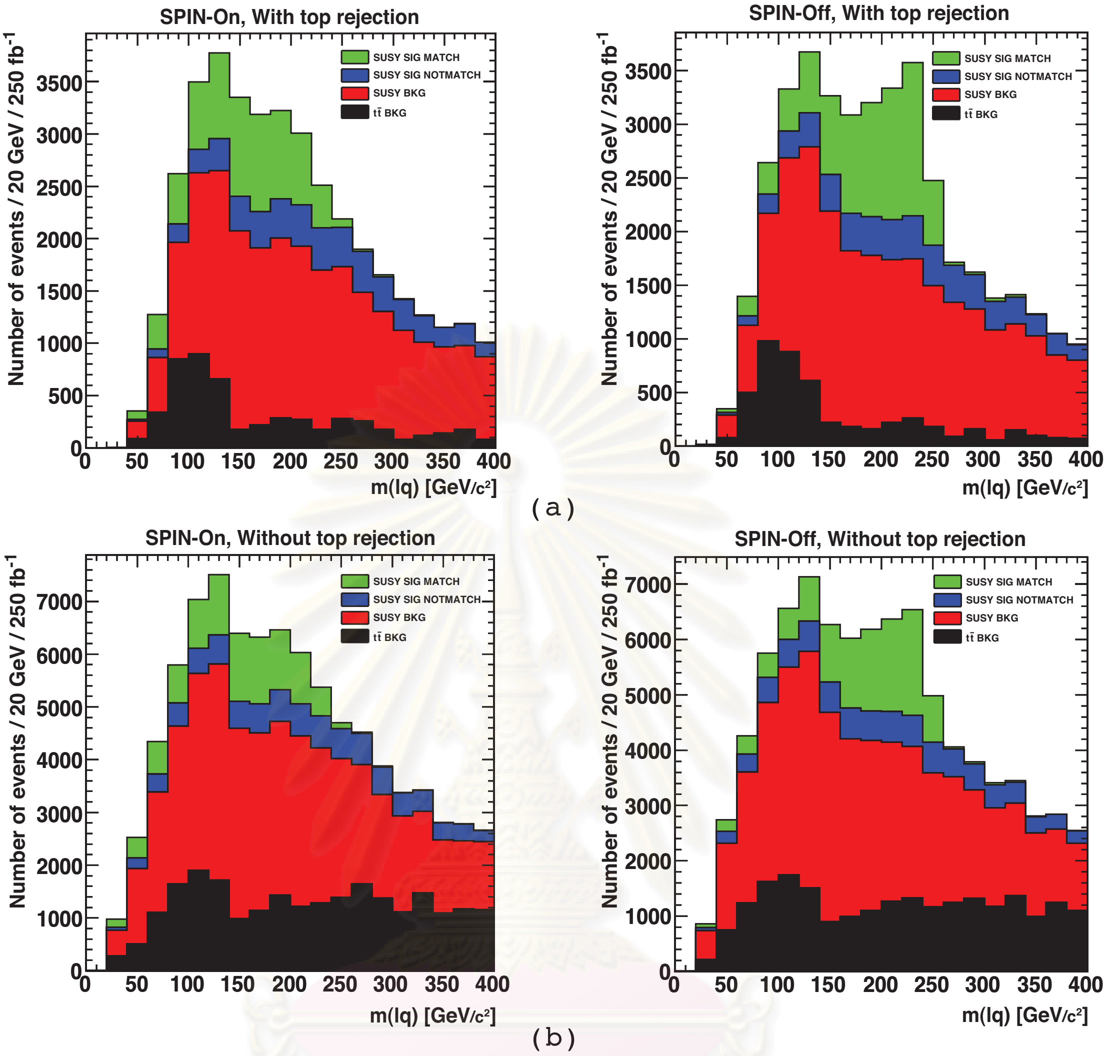

Figure 5.33: The stacked distributions of lepton and b-quark invariant mass for the LM6 data at 250 fb^{-1} when the top rejection is included (a), is not included (b). The meanings of each layer from bottom to top are as follows. The black layer presents the surviving events of the $t\bar{t}$ process. The red layer represents the surviving SUSY events which do not contain the decay chain of interest. The blue layer shows the surviving SUSY events which have the decay chain of interest but the mis-selection from lepton and/or jet happened. The green layer shows the correct selection from both lepton and jet.

5.5.2 Detector level analysis

5.5.2.1 Detector level analysis using simulated data from CMSSW_3_3_4

The study of this decay chain started after the fast simulation of the CMSSW_2_2_6 came out, so FAMOS_1_6_0 results are not available. The results which are shown here are summarized from the fast simulation and physics analysis tools packages for CMSSW_3_3_4. The LM6 data sample at 250 fb^{-1} is used in this analysis. The event selection is as follows,

1. MET > 300 GeV.
2. $n_{jet}(P_T > 50$ GeV/c$) \geq 3$.
3. $n_{b-jet}(P_T > 50$ GeV/c$) \geq 1$..
4. The highest P_T b-jet ($\geq$ 160 GeV/c) is selected.
5. The highest P_T^{lepton} ($\geq$ 15 GeV/c) is selected.
6. The number of SFOS leptons (opposite charge with the selected lepton) is required to be zero.
7. The pseudorapidity cut of jet and lepton follows the basic object selection discussed in Section 5.3. It includes $|\eta_{electrons}| < 2.5$, $|\eta_{muons}| < 2.1$, $|\eta_{taus}| < 2.4$, and $|\eta_{jets}| < 2.4$.
8. The number of jets or leptons within the cone size of 0.7 from the selected jet is equal to zero. The cut was done to avoid the b-jet from top quark decay.

The results, shown in Figure 5.34,with the detector simulated data show the difference of the peak's positions between the distributions. When the spin correlation function is not considered (newly produced particles are not supersymmetry), the peak of the distribution locates between 200 and 250 GeV/c^2. This

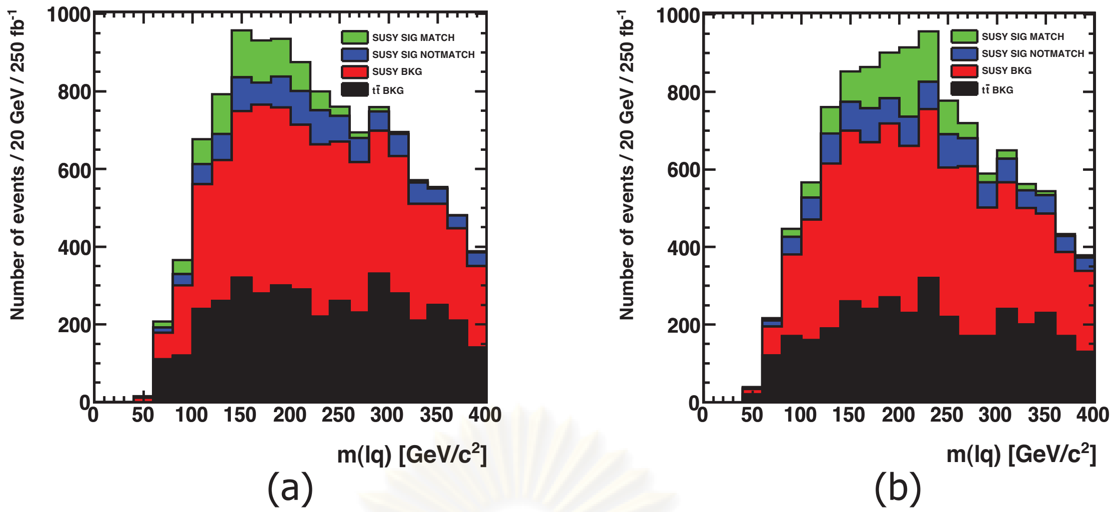

Figure 5.34: The distributions of lepton and b-jet invariant mass using the detector level data from `CMSSW_3_3_4`. (a) when the spin correlation was turned on, (b) turned off. The meanings of each layer are the same as Figure 5.33

peak corresponds to the peak shown at the parton level. It can be interpreted as the newly produced particles have the same spins of their partners, which is not the supersymmetry case. In the supersymmetry case (at the LM6 benchmark point), the peak of the invariant mass between selected lepton and b-jet should locate between 150 and 200 GeV/c^2. This peak corresponds with the peak calculated by probability density function described by Equation (5.62).

With this decay chain of interest, one can see that the required statistics of data is lower than the required statistics to study the decay chain via neutralino-2. As discussed previously, the main background is not Standard Model processes, but it is the other supersymmetric decay chains which can contaminate and dilute our decay chain of interest.

CHAPTER VI

Conclusion and Outlook

In this thesis, the spin measurement through effects on angular correlations in supersymmetric decay products has been studied. The Lorentz invariant quantity - invariant mass - of the decay products was used to investigate the angular correlations. Two supersymmetric decay chains which are (1) the decay of squark via neutral boson's partner, neutralino-2 ($\tilde{\chi}_2^0$), and (2) the decay of stop (supersymmetric top) via charge boson's partner, chargino-1 ($\tilde{\chi}_1^{\pm}$), were considered to extract the spin information of boson's partners from their decay products. Their decay products include lepton, jet, and missing transverse energy from the lightest supersymmetric particles. The existence of the light supersymmetric particles at the end of the decay chain can help us to reduce the contamination of the Standard Model background by applying a cut on large missing transverse energy.

For the first decay chain of interest, $\tilde{q} \rightarrow q\tilde{\chi}_2^0 \rightarrow ql_{near}^{\pm}\tilde{l}^{\mp} \rightarrow ql_{near}^{\pm}l_{far}^{\mp}\tilde{\chi}_1^0$, the imbalance of the production rate between the positive and negative sign leptons-near can lead us to observe the spin correlation effect. The complicated part of this decay chain comes from the existence of the lepton-far which cannot be distinguished in an experiment. We used the Barr's defined asymmetry parameter to investigate the sensitivity of the invariant mass of lepton and jet with the spin of $\tilde{\chi}_2^0$. For the LM1 benchmark point, the lepton charge asymmetry can be seen clearly from the electron-muon and tau distributions. The statistics of the data is about 65 fb^{-1}, which is about the expected nominal LHC luminosity. Note that, for the LHC Data in 2010 ($\sqrt{s} = 7$ TeV, $\int Ldt = 35$ pb^{-1}), the LM1 benchmark point LM1 is excluded at 99.2% from the CMS experiment [39]. For the LM2 benchmark point where the electron and muon production rate from the neutralino is compressed by tau, the asymmetry can be seen with 250 fb^{-1}. For the LM6 benchmark point, higher statistics is needed in order to extract the spin information by using a lepton charge asymmetry. The background which dilutes a lepton charge study comes from other supersymmetric decay chains. For both the LM2 and LM6, they are challenges since both of them have lower cross-sections than LM1's. The third generation fermions play an important role in supersymmetry. With the good efficiency of $b-$ and $\tau-$tagging algorithms, it is possible to make a precise measurement of the new physics.

For the second decay chain of interest, $\tilde{t}^{\pm} \rightarrow b^{\mp}\tilde{\chi}_1^{\pm} \rightarrow b^{\mp}l^{\pm}\tilde{\nu}_l \rightarrow bl^{\pm}\nu_l\tilde{\chi}_1^0$, it is another possible SUSY decay chain to extract the spin information for the LM6 benchmark point. The invariant mass of lepton and b-jet is used to extract the spin information. The significant difference can be seen from the lepton and b-jet invariant mass when the spin correlation is and is not considered. The expected integrated luminosity is at 250 fb^{-1}. Note that, in this thesis, the distribution when the spin correlation is not considered represents other groups of theories which expect the same spin partner of the Standard Model particles, e.g. universal extra-dimension models.

REFERENCES

[1] Gonzalez-Garcia, M. C. and Nir, Y. Developments in neutrino physics. *Rev. Mod. Phys.* **75** (2003): 345-402.

[2] Peltoniemi, J. The Ultimate Neutrino Page. [Online]. 2005. Available from: `http://cupp.oulu.fi/neutrino/`.

[3] CMS Collaboration. CMS Physics Technical Design Report, Volume II: Physics Performance. *J. Phys. G* **34** (2007): 995.

[4] CMS Collaboration. A candidate for production of a top quark pair in CMS. [Online]. 2010. Available from: `http://cdsweb.cern.ch/record/1280695`.

[5] Pi, H. and Wuerthwein, F. Study of QCD background for W+jets with isolated lepton+jet +missing E_T signature. *CMS IN* **2006/108** (2006).

[6] CMS Collaboration. CMS Physics Technical Design Report, Volume I: Detector Performance and Software. *CERN/LHCC* **2006-001** (2006).

[7] Eidelman, S. *et al.* Review of Particle Physics. *Phys. Lett.* **B592** (2004): 1-5.

[8] Barate, R. *et al.* Search for the standard model Higgs boson at LEP. *Phys. Lett.* **B565** (2003): 61-75.

[9] Bilal, A. Introduction to supersymmetry. 2001. [arXiv:hep-th/0101055].

[10] Djouadi, A. The MSSM. [Online]. 1998. Available from: `http://www.lpta.univ-montp2.fr/users/djouadi/GDR/latex/mssm/mssm.html`.

[11] Battaglia, M. *et al.* Updated post-WMAP benchmarks for supersymmetry. *Eur. Phys. J.* **C33** (2004): 273.

[12] Brüning, O. S. *et al.* *LHC Design Report.* CERN, Geneva (2004).

[13] CERN. The accelerator complex. [Online]. 2008. Available from: `http://public.web.cern.ch/public/en/research/AccelComplex-en.html`.

[14] Klein, K. The CMS Silicon Strip Tracker - Overview and Status. 2006. [arXiv:physics/0610259].

[15] Dominguez, A. The CMS pixel detector. *Nucl. Instrum. Methods. Phys. Res.* **A581** (2007): 343.

[16] Cavallari, F. Progress in the CMS ECAL. *Nucl. Instr. and Meth.* **A461** (2001): 368.

[17] CMS Collaboration. The CMS Experiment at the CERN Large Hadron Collider. *J. Instrum.* **4** (2008): S08004.

[18] CMS Collaboration. The Muon Project, Technical Design report. *CERN/LHCC* **97-32** (1997).

[19] Binetti, C., Liuzzi, R., Loddo, F., Marangelli, B., and Ranieri, A. A new Front-End board for RPC detector of CMS. *CMS NOTE* **1999/047** (1999).

[20] Sjostrand, T., Mrenna, S., and Skands, P. Z. PYTHIA 6.4 Physics and Manual. *J. High Energy Phys.* **JHEP05** (2006): 026.

[21] Corcella, G. *et al.* HERWIG 6.5: an event generator for Hadron Emission Reactions With Interfering Gluons (including supersymmetric processes). *J. High Energy Phys.* **JHEP01** (2001): 010.

[22] Paige, F. E., Protopopescu, S. D., Baer, H., and Tata, X. ISAJET 7.69: A Monte Carlo event generator for p p, anti-p p, and e+ e- reactions. 2003. [arXiv:hep-ph/0312045].

[23] Richardson, P. ISAWIG. [Online]. 2002. Available from: `http://www.hep.phy.cam.ac.uk/~richardn/HERWIG/ISAWIG`.

[24] Wynhoff, S. FAMOS: A Dynamically Configurable System for Fast Simulation and Reconstruction for CMS. 2003. [arXiv:physics/0306052].

[25] Janot, P. FAMOS. [Online]. 2005. Available from: `http://cmsdoc.cern.ch/cms/FAMOS/`.

[26] CMS Collaboration. CMSSW Application Framework. [Online]. 2010. Available from: `https://twiki.cern.ch/twiki/bin/view/CMS/WorkBookCMSSWFramework`.

[27] Richardson, P. Spin Correlations in Monte Carlo Simulations. *J. High Energy Phys.* **JHEP11** (2001): 029.

[28] Barr, A. J. Determining the spin of supersymmetric particles at the LHC using lepton charge asymmetry. *Phys. Lett.* **B596** (2004): 205-212.

[29] Goto, T., Kawagoe, K., and Nojiri, M. M. Study of the slepton non-universality at the CERN Large Hadron Collider. *Phys. Rev.* **D70** (2004): 075016.

[30] CMS Collaboration. Plans for Jet Energy Corrections at CMS. *CMS PAS* **JME-07-002** (2008).

[31] Salam, G. P. Towards Jetography. *Eur. Phys. J.* **C67** (2010): 637.

[32] Blazey, G. C. *et al.* Run II jet physics. 2000. [arXiv:hep-ex/0005012].

[33] Bagliesi, G. Reconstruction and identification of tau decays at CMS. *J. Phys.: Conf. Ser.* **119** (2008): 032005.

[34] Rizzi, A., Palla, F., and Segneri, G. Track impact parameter based b-tagging with CMS. *CMS NOTE* **2006/019** (2006).

[35] Miller, D. J. *et al.* Invariant mass distributions in cascade decays. *J. High Energy Phys.* **JHEP03** (2006): 034.

[36] Athanasiou, C. *et al.* Distinguishing spins in decay chains at the large hadron collider. *J. High Energy Phys.* **JHEP08** (2006): 055.

[37] Gedalia, O. *et al.* Spin determination via third generation cascade decays. *Phys. Rev.* **D80** (2009): 035012.

[38] Graesser, M. and Shelton, J. Probing supersymmetry with third-generation cascade decays. *J. High Energy Phys.* **JHEP06** (2009): 039.

[39] CMS Collaboration. Search for Supersymmetry in pp Collisions at 7 TeV in Events with Jets and Missing Transverse Energy. 2011. [arXiv:1101.1628v1 [hep-ex]].

[40] Cox, P. T. Review of neutron background studies in the Endcap Muon CSCs. [Online]. 2001. Available from: `http://ptc.web.cern.ch/ptc/down/resources/presentations/mprs_010426/mprs_010426.html`.

[41] Geant4 Collaboration. Reference Physics Lists. [Online]. 2008. Available from: `http://geant4.cern.ch/support/proc_mod_catalog/physics_lists/useCases.shtml`.

[42] ATLAS Collaboration. The ATLAS Experiment at the CERN Large Hadron Collider. *J. Instrum.* **3** (2008): S08003.

[43] Abbrescia, M. *et al.* The RPC system for the CMS experiment at the LHC. *Nucl. Instr. and Meth.* **A508** (2003): 137.

[44] Choi, S. Y. *et al.* Analysis of the neutralino system in supersymmetric theories. *Eur. Phys. J.* **C22** (2001): 563.

[45] Beylin, V. A. *et al.* Diagonalization of the neutralino mass matrix and boson-neutralino interaction. *Eur. Phys. J.* **C56** (2008): 395.

APPENDICES

APPENDIX A

Acronym

- ALICE: A Large Ion Collider Experiment
- AOD: Analysis Object Data
- ATLAS: A Toroidal LHC ApparatuS
- AVD: Avalanche Photo Diodes
- CAF: CERN Analysis Facility
- CERN: European Organization for Nuclear Research
- CMS: Compact Muon Solenoid
- COBRA: Coherent Object-oriented Base for Reconstruction, Analysis and simulation
- CSCs: Cathode Strip Chambers
- CSEWG: Cross Section Evaluation Working Group
- DAQ: Data Acquisition
- DTs: Drift Tube chambers
- EDM: CMS Event Data Model
- ENDF: Evaluated Nuclear Data File
- EOP: Electromagnetic energy over track momentum

- FAMOS: FAst MOnte Carlo Simulation for CMS
- FWLite: Framework-light
- G4NDL: GEANT4 Neutron Data Library
- GEANT4: GEometry ANd Tracking (A toolkit for the simulation of the passage of particles through matter)
- HB: Barrel Hadronic Calorimeter
- HE: Endcap Hadronic Calorimeter
- HF: Forward Calorimeter
- HERWIG: (The Monte Carlo package for) Hadron Emission Reactions With Interfering Gluons
- HLT High-Level Trigger
- HO: Outer Hadronic Calorimeter
- HOE: Hadronic energy Over Electromagnetic energy
- L1: Level-1 Trigger System
- LEP: Large ElectronPositron Collider
- LHC: Large Hadron Collider
- LHCb: Large Hadron Collider beauty experiment
- LHCf: Large Hadron Collider forward
- LSP: Lightest Supersymmetric Particle
- MB: Muon Barrel
- ME: Muon Endcap
- MET: Missing transverse energy

- MONARC: Models of Networked Analysis at Regional Centres
- MSSM: Minimal Supersymmetric Standard Model
- mSUGRA: Minimal Supergravity
- ORCA: Object oriented Reconstruction for CMS Analysis
- OSCAR: Object oriented Simulation for CMS Analysis and Reconstruction
- PAT: Physics Analysis Toolkit
- pMSSM: Phenomenological Minimal Supersymmetric Standard Model
- QGSP_BERT_HP: Quark-Gluon String Precompound model with Bertini Cascade Model and High Precision Neutron Model
- RPCs: Resistive Plate Chambers
- SUSY: Supersymmetry
- TIB: Tracker Inner Barrel
- TID: Tracker Inner Disk
- TEC: Tracker Endcap
- TriDAS: Trigger and Data Acquisition System
- TOB: Tracker Outer Barrel
- UED: Universal Extra Dimension
- VPT: Vacuum PhotoTriodes
- uMSSM: Unconstrained Minimal Supersymmetric Standard Model

APPENDIX B

The neutron background study at the CMS detector

In this section, the early work of the author which was done during the first few years when joining the CMS collaboration is introduced[1]. The neutron background study was chosen as the topic of work. In addition, the author also used this work to study the whole simulation processes, including detector simulation, basic data structure, and data analysis with the CMS software.

At high luminosity of the LHC ($10^{34}\,\mathrm{cm}^{-2}\mathrm{s}^{-1}$), the inelastic interactions of neutrons can be as high as 10^9 interactions per second [40]. One of the neutron inelastic interactions which needs to be considered is neutron capture. The neutron can be captured by nuclei and leads to photon emission. These photons can produce electrons via the compton scattering or the photoelectric processes in detector materials. The appearance of the electrons can lead to hits in the muon chambers. These hits can cause noise in the muon signals. In addition, neutrons also take a long time, compare with the beam crossing time, to thermalize, or in other words, to be captured by nuclei. Consequently, neutrons which are produced in an events can cause the hits in other events later.

The neutron background had been studied using the `CMSIM_1_2_1` which is based on `GEANT3` simulation package. In this work, the `GEANT4` simulation on the `OSCAR` package was used. This study has the benefit of the new simulation module, including ion simulation and a new physics package for the thermal neutron. In

[1] This work had been done under supervised of P. Arce and P. T. Cox.

this study, the physics model QGSP_BERT_HP was used [41]. This physics model is suitable for background radiation studies, including neutron production and transport. In this work, the minimum bias events are generated as the neutron background source.

In the results, the number of hits in the muon chambers by the interaction products of neutrons are shown. These interaction products included electrons, protons and charged ions. Figure B.1 shows the number of hits from the interaction products of neutron in the muon endcap chambers. The x-axis and y-axis of the plot represents the energy scale and the time of flight of particles in the log scale, respectively. This plot was done using the minimum bias sample from the PYTHIA6 generator and CMSIM_1_2_1. The average number of hits per event in this results is 1.1 in the endcaps when the time of flight is greater than 250 ns.

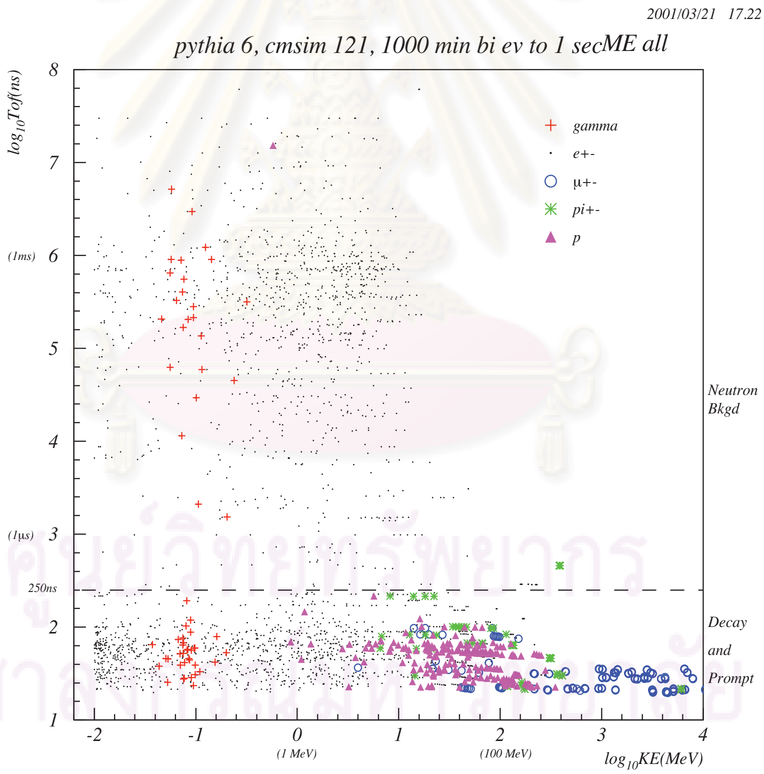

Figure B.1: The number of hits from the daughters of neutrons in the muon endcap chambers simulated by CMSIM_1_2_1. Note that, the gamma in this plot came from the bug of GEANT3.

To compare with the previous results, the simulation of the hits from interaction products of neutrons was simulated using OSCAR_3_3_2. Figures B.2, B.3 and B.4, show the number of hits from the interaction products of neutron in all muon chambers, CSC volumes, and RPC volumes, respectively. Note that, the components of the CSC material was discussed in Section 3.3.4.4. The numbers of hits in the CSC volumes are shown similarity between OSCAR_3_3_2 study (Figure B.3) and CMSIM_1_2_1 study (Figure B.1). For the RPC volumes, the numbers of protons, fluorine ions and sulphur ions showed up. This is a problem we investigated.

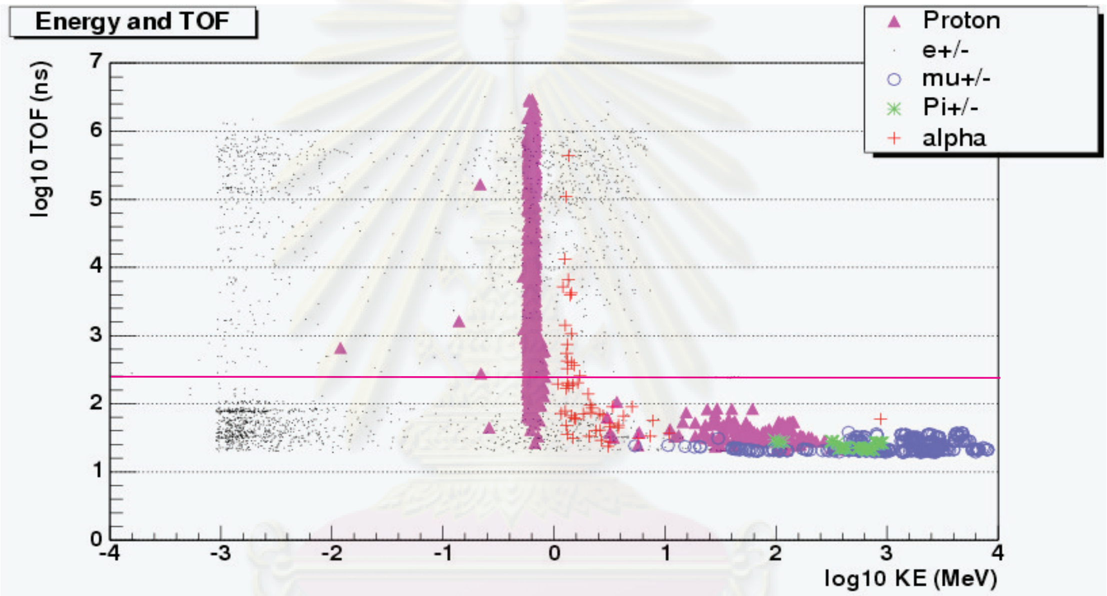

Figure B.2: The number of hits from the daughters of neutrons in all muon chambers (DTs, RPCs, CSCs) simulated by OSCAR_3_3_2.

To understand the problem of increasing number of protons and few types of ions clearly, we had to investigate if this strange behavior of the proton and ion production from neutron came directly from the material effect. Two methods to study this problem were proposed. The first method was to run the Monte Carlo simulation by using GEANT4 with simple box geometries, while the second method was to run Monte-Carlo simulation using OSCAR_3_3_2 with modified CMS material.

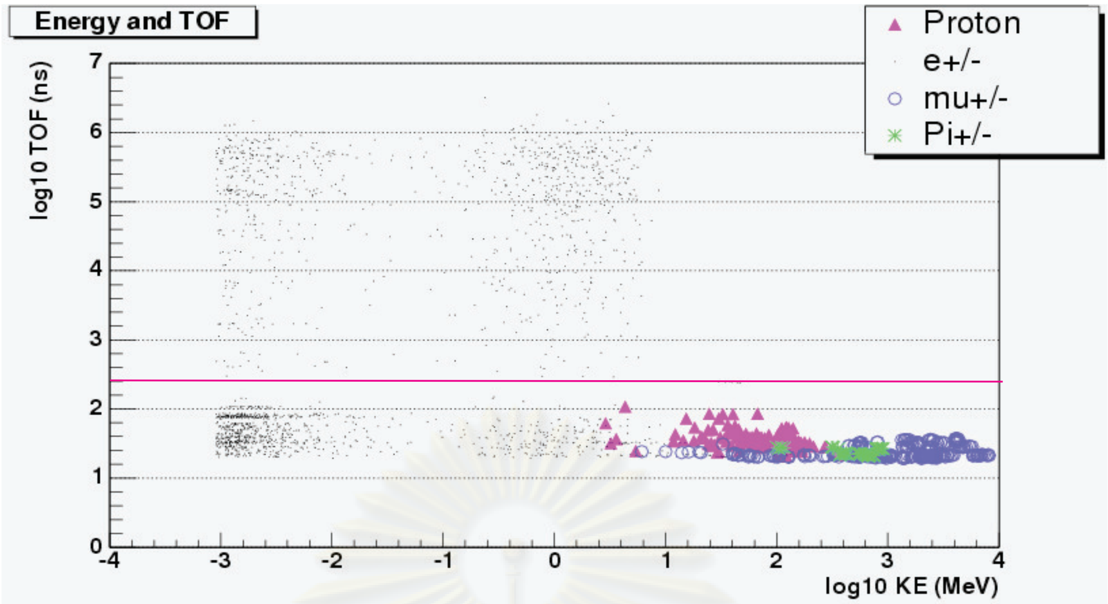

Figure B.3: The number of hits from the daughters of neutrons in the muon CSC chambers simulated by OSCAR_3_3_2.

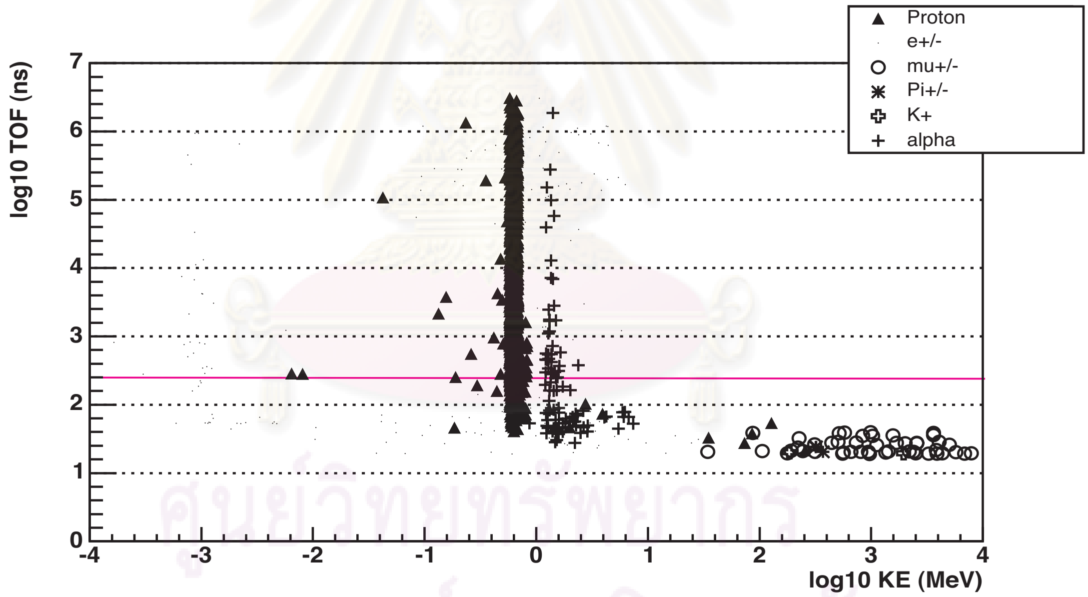

Figure B.4: The number of hits from the daughters of neutrons in the muon RPC chambers simulated by OSCAR_3_3_2.

For the first method, three simple geometries, including a simple box of CSC gas, RPC gas and a simple box of CSC gas with six small layers of RPC gas, were created to use with GEANT4 and QGSP_BERT_HP 1.0 physics model. The

CSC and RPC gas components were shown in Table B.1. The energy of the incoming neutrons varied between 10^{-4} - 10^{-3} MeV. The result of the Monte-Carlo simulation with 100,000 events is shown in Table B.2. In this table, the number of protons and ions coming from neutron interactions are shown.

	CSC Gas	RPC Gas
C-12	16.31%	25.89%
O-16	30.87%	67.56%
F-19	29.86%	1.67%
Cl-35	-	3.12%
Ar-40	22.96%	1.76%

Table B.1: The gas components in the muon chambers.

	Mix		Pure	Pure
	CSC	RPC	CSC	RPC
F19	519392	718	512	28895900
S35	24111	2	0	36500
Proton	24427	68	98	36800

Table B.2: The number of proton and ions occurred from neutron interaction.

For the second method, the modified CMS material was separated into two versions, the first version used CSC gas in all muon systems, while the second one was used RPC gas instead. Figure B.5 shows the number of fluorine ion hits when the RPC gas was used, while Figure B.6 shows the number of fluorine ion hits when the CSC gas was used.

From the results of both methods, we can conclude that the strange behavior of hits from protons and ions in the muon chambers came directly from the material effects. The results showed that, with the pure CSC gas, the number of hits is very small compared to the number of hits when the RPC gas was used. Thus the number of neutron interactions in CSC gas is much smaller than the interactions

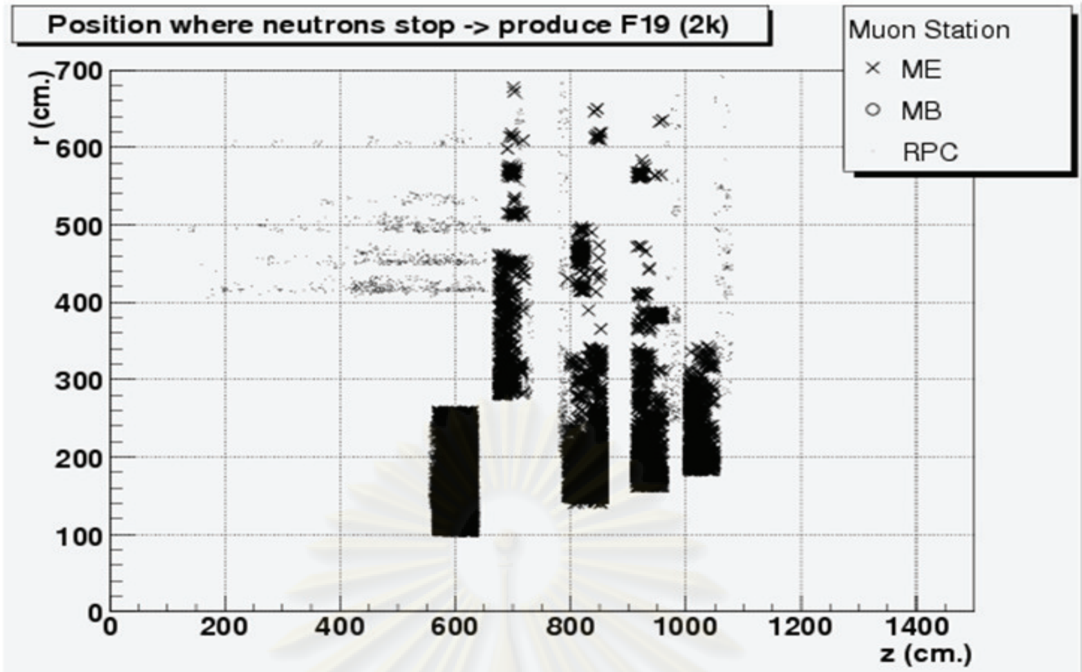

Figure B.5: The hit positions in the muon endcap stations when the RPC gas were used in all volumes.

in the RPC gas. One can also see that the number of hits from the fluorine gas in the RPC material is higher than the CSC material, this result contradicted with the fraction of the fluorine in the CSC gas which is higher than in the RPC gas. The interaction which can produce fluorine ions from neutron is $n_0^1 + F_9^{19} \rightarrow n_0^1 + F_9^{19} + \gamma(s)$. Since the cross section data of the fluorine for the CSC and RPC gases are the same, therefore the cross section data of the fluorine should not lead to the problem of a huge number of neutron interactions. We then considered the reaction $n_0^1 + Cl_{17}^{35} \rightarrow p_1^1 + S_{16}^{35}$. After discussing with the neutron experts in the `GEANT4` group, we found that the neutron cross section for the inelastic process of the chlorine contained a bug which gave a very high values at certain energy levels. This caused an increasing of the total cross section of the gas. It can help us solve the problem of fluorine ions which have a fraction in the CSC above the RPC, while the number of neutron interactions is much smaller. The fix of this bug was released in the G4NDL 3.8. The result of `GEANT4` simulation with simple geometries is shown in Table B.3. Note that the `GEANT4` neutron

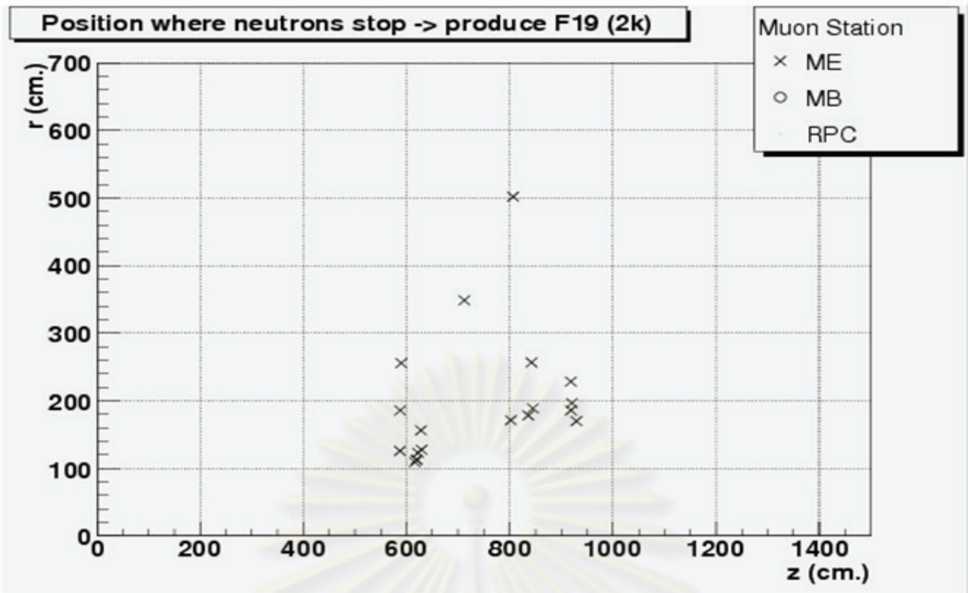

Figure B.6: The hit positions in the muon endcap stations when the CSC gas were used in all volumes.

data library (G4NDL) which is used for the thermal neutron interaction is mainly based on the Evaluated Nuclear Data File (ENDF). The ENDF is developed and maintained by the Cross Section Evaluation Working Group (CSEWG), National Nuclear Data Center, Brookhaven National Laboratory. With the new neutron data library, the new result of the hit in the muon chambers was determined and shown in Figure B.7. Agreement was found with the previous study by `CMSIM` in which the average number of hits in an event in the endcaps is equal to 0.82 which is lower than previous study.

From this study, it follows that the average number of hits of particles, which are the interaction products of neutrons, is lower than previous study. The average number of hits is 0.82 in the CSC volumes compared with 1.1 hits from `CMSIM_1_2_1` study. Therefore it should not cause a serious problem from a noise of neutron background in the reconstruction processes at the high luminosity at the LHC. Figure B.7 shows the hits in the CSC volumes using the corrected chlorine data with `CMSSW_1_0_0`.

	Mix		Pure	Pure
	CSC	RPC	CSC	RPC
F19	20	5364	5338	295
S35	0	2	4	2
Proton	18	738	861	696

Table B.3: The number of protons and ions occurred from neutron interactions with G4NDL 3.8. Note that, this result came from 1,000,000 events simulation.

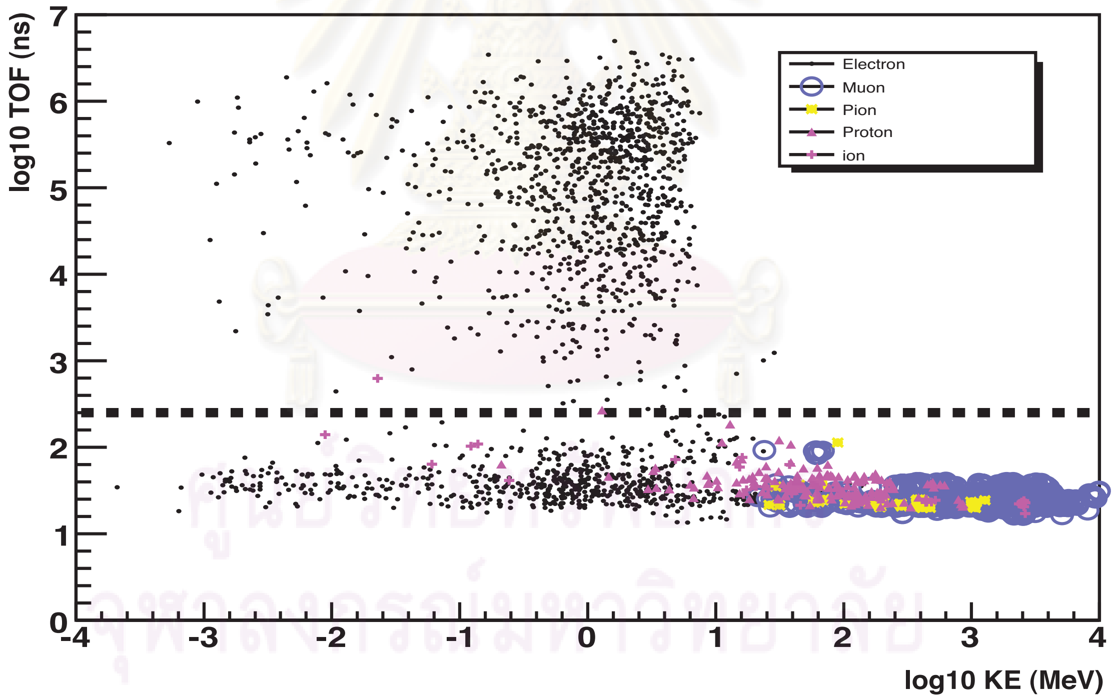

Figure B.7: The hits in the muon endcap stations using the corrected chlorine data with `CMSSW_1_0_0`.

APPENDIX C

Diagonalization of the neutralino mass matrix

In this chapter, we review an analytical solution to calculate the mixing matrix U which diagonalize the neutralino mass matrix, $U^* M_{\tilde{\chi}^0} U^\dagger = \text{diag}\ (m_{\tilde{\chi}^0})$. This analytical solution was discussed in [44, 45]. In the Minimal Supersymmetric Standard Model (MSSM), the neutralino mass eigenstates come from the mix of the neutral gauge bosons, $\tilde{B}, \tilde{W}^0, \tilde{h}_1^0$, and $\tilde{h}_2^0$. The neutralino mass matrix can be written as

$$M_{\tilde{\chi}^0} = \begin{pmatrix} M_1 & 0 & -m_z c_\beta s_W & m_z s_\beta s_W \\ 0 & M_2 & m_z c_\beta c_W & -m_z s_\beta c_W \\ -m_z c_\beta s_W & m_z c_\beta c_W & 0 & -\mu \\ m_z s_\beta s_W & -m_z s_\beta c_W & -\mu & 0 \end{pmatrix}, \tag{C.1}$$

where $s_W = \sin\theta_W, c_W = \cos\theta_W, s_\beta = \sin\beta,$ and $c_\beta = \cos\beta$. In this paper, we consider when $M_1^2, M_2^2,$ and μ^2 are much larger than m_Z^2 and all of them are real. For the general case, it was discussed in [44]. The mixing matrix U can be written into a composite form as

$$U = MDP \tag{C.2}$$

where

$$P = \begin{pmatrix} \mathbf{1} & \mathbf{0} \\ \mathbf{0} & \mathbf{O_2} \end{pmatrix}; \mathbf{O_2} = \frac{1}{\sqrt{2}} \begin{pmatrix} 1 & -1 \\ 1 & 1 \end{pmatrix}, \tag{C.3}$$

$$M = \mathrm{diag}(1,1,1,i), \tag{C.4}$$

$$D = \begin{pmatrix} a_1 & s_{12} & s_{13} & s_{14} \\ -s_{12}^{'} & a_2 & s_{23} & s_{24} \\ -s_{13} & -s_{23} & a_3 & s_{24} \\ -s_{14} & -s_{24} & -s_{13}^{'} & a_4 \end{pmatrix} \tag{C.5}$$

The components of the D matrix are

$$\begin{aligned}
s_{12} &= +\frac{m_Z^2 c_W s_W}{(M_2^2 - M_1^2)(M_1^2 - \mu^2)}(M_1 + M_2)(M1 + \mu s_{2\beta}), \\
s_{13} &= -\frac{m_Z s_W c_\eta}{M_1 - \mu}, \quad s_{14} = -\frac{m_Z s_W s_\eta}{M_1 + \mu}, \\
s_{23} &= +\frac{m_Z c_W c_\eta}{M_2 - \mu}, \quad s_{24} = +\frac{m_Z c_W s_\eta}{M_2 + \mu}, \\
s_{24} &= +\frac{m_3 - \mu}{2\mu}\frac{s_\eta}{c_\eta}, \\
s_{12}^{'} &= s_{12} + s_{13}s_{23} + s_{14}s_{24}, \quad s_{34}^{'} = s_{34} + s_{13}s_{14} + s_{23}s_{24}, \\
a_1 &= \sqrt{(1 - s_{13}^2)(1 - s_{14}^2)}, \quad a_2 = \sqrt{(1 - s_{23}^2)(1 - s_{24}^2)}, \\
a_3 &= \sqrt{(1 - s_{13}^2)(1 - s_{23}^2)}, \quad a_4 = \sqrt{(1 - s_{14}^2)(1 - s_{24}^2)}
\end{aligned} \tag{C.6}$$

where s_η and c_η are $(c_\beta - s_\beta)/\sqrt{2}$ and $(c_\beta + s_\beta)/\sqrt{2}$, respectively. The m_3 is defined in Equation (C.7). With the unitary matrix formation presented above, one can see that $|UU^\dagger|_{ii} \approx 1$ and $|UU^\dagger|_{ik} \ll 1, i \neq k$. The neutralino masses can be calculated from $U^* M_{\tilde{\chi}^0} U^\dagger = \mathrm{diag}\ (m_{\tilde{\chi}^0})$. The masses of neutralinos are as follows,

$$\begin{aligned}
m_1 &= M_1 + \frac{m_z^2 s_W^2}{M_1^2 - \mu^2}(M_1 + \mu s_{2\beta}), \\
m_2 &= M_2 + \frac{m_z^2 c_W^2}{M_2^2 - \mu^2}(M_2 + \mu s_{2\beta}), \\
m_3 &= \mu + \frac{m_z^2(1 - s_{2\beta})}{2(M_1 + \mu)(M_2 + \mu)}(M_1 c_W^2 + M_2 s_W^2 + \mu), \\
m_4 &= \mu - \frac{m_z^2(1 - s_{2\beta})}{2(M_1 - \mu)(M_2 - \mu)}(M_1 c_W^2 + M_2 s_W^2 - \mu).
\end{aligned} \tag{C.7}$$

APPENDIX D

Chi-square test

The chi-square distribution is particularly useful for testing the goodness-of-fit of theoretical formulae or predicted distributions to experimental data. Mathematically, the chi-square is defined as

$$\chi^2 = \sum_N \left\{ \frac{1}{\sigma_i^2} [y_i - f(x_i)]^2 \right\}, \tag{D.1}$$

where N is the number of data point, σ_i^2 is the variance which relates to the measurement error of y_i, y_i is the observed mean and $f(x_i)$ is predicted mean.

In this study, the fitting function, f, describes the assumed functional relationship between the invariant mass (as the independent variable on x-axis) and the lepton charge asymmetry (as the dependent variable on y-axis). The fitting function should accurately predict the means of the distribution at each data point, then the estimated variance of the fit, s^2, should agree well with the variance of the data at that point, σ^2. Their ratio should be close to one. The ratio of s^2/σ^2 can be estimated by χ^2/ν where ν is called degree of freedom. The degree of freedom can be calculated by

$$\nu = N - P - 1, \tag{D.2}$$

where N is the number of observations, and P is the number of fitting parameters. The value of χ^2/ν is sometimes called "reduced chi-square", "normalized chi-square", or "chi-square per degree of freedom".

The chi-square has the probability distribution given by

$$f(\chi^2) = \frac{1}{2^{\nu/2}\Gamma(\nu/2)} e^{-\chi^2/2} (\chi^2)^{(\nu/2)-1}. \qquad \text{(D.3)}$$

This is know as the "χ^2-distribution with ν degree of freedom". $\Gamma(x)$ is the "Gamma function", defined by

$$\Gamma(x+1) \equiv \int_0^\infty t^x e^{-t} dt. \qquad \text{(D.4)}$$

Examples of graphs of $f(\chi^2)$ versus χ^2 are shown in Figure D.1. Note that χ^2 range only over positive values ($0 < \chi^2 < \infty$).

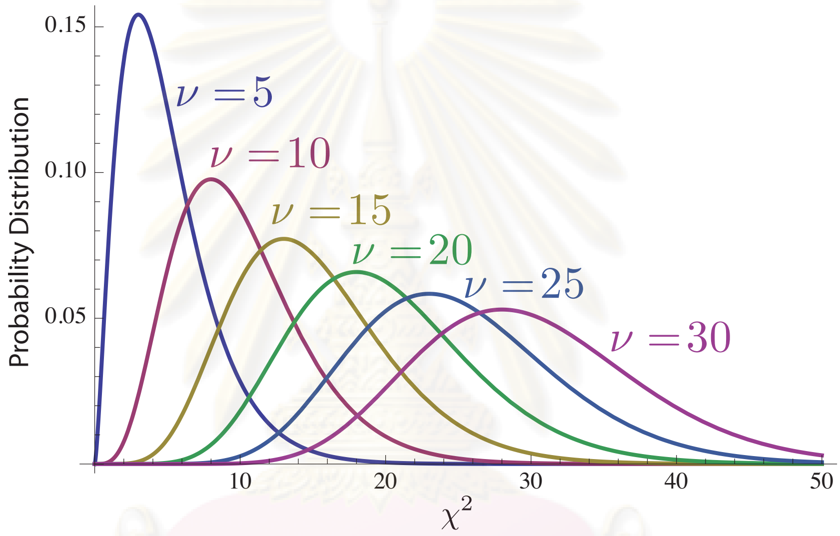

Figure D.1: The cumulative distribution function (c.d.f.) of chi-square when the degrees of freedom are equal to 5, 10, 15, 20, 25, and 30.

To use χ^2 to test for goodness of the fit, we calculate the probability α from

$$\alpha = \int_{\chi^2_{\nu,\alpha}}^\infty f(\chi^2) d\chi^2. \qquad \text{(D.5)}$$

We then compare a calculated probability α with the significance level, α_{cri}. A common value for α_{cri} is 0.05. Or on the other hand, we can calculate numerically χ^2_{cri} which corresponds with α_{cri}, then compare χ^2_{cri}/ν with χ^2/ν from our data. We can interpret the comparison between χ^2_{cri}/ν and χ^2/ν as follows,

- If χ^2 is too small ($\chi^2/\nu < \chi^2_{1-\alpha}/\nu$):

  1. The fitting function is valid but a statistically improbable value of χ^2 occurs.
  2. The values of σ_i are over-estimated.
  3. The experimental data is too good (to be true).

  Note that, in this case, we cannot interpret that the fitting function is a poor model. A poor model can only increase the value of χ^2.

- If $\chi^2/\nu > \chi^2_{cri}/\nu$: The fitting function is a poor model, then a large value of χ^2 occurs. In this case, we have $100 \cdot (1-\alpha)\%$ to reject our fitting function.

Generally speaking, for a good fit, a sample value χ^2/ν should be close to 1 or α should be close to 0.5, or in other words, the chi-square falls in the "fat region" of the probability curve.

VITAE

Mr. Norraphat Srimanobhas was born on August 27, 1982 in Bangkok. He received his bachelor degree (first class honor) of Science in Physics from Mahidol University in 2002. He had been supported financially to study and to research with the CMS collaboration by (1) the Development and Promotion of Science and Technology Talents Project (DPST), (2) Chulalongkorn University, and (3) University of Antwerp.

Conference Presentations:

2007 **N. Srimanobhas, B. Asavapibhop, and A. De Roeck**
"Spin-sensitive variables for the products of supersymmetric particles", *2nd Siam Physics Congress (SPC2007)*, Nakorn Pathom, Thailand (March 22-24, 2007).

Schools and Meetings:

2005 12nd Vietnam School of Physics
Hanoi, Vietnam (December 26, 2005 - January 07, 2006).

2009 4th CERN-Fermilab Hadron Collider Physics Summer School
CERN, Geneva, Switzerland (June 8-17, 2009).

2011 1st Particle Physics School in South-East Asia
Kuala Lumpur, Malaysia (March 14-18, 2011).